②

AD-A203 514

UNITED STATES ARMY EUROPEAN RESEARCH OFFICE

F I N A L   R E P O R T

(May - July, 1988)

Professor J. Jortner
Tel Aviv University
Israel

Contract No.:   DAJA45-85-C-0008

DTIC
ELECTE
DEC 2 7 1988
S
D
α
H

88 12 27 027

REPORT DOCUMENTATION PAGE

Form Approved
OMB No. 0704-0188
Exp. Date: Jun 30, 1986

1a. REPORT SECURITY CLASSIFICATION Unclassified	1b. RESTRICTIVE MARKINGS

2a. SECURITY CLASSIFICATION AUTHORITY	3. DISTRIBUTION/AVAILABILITY OF REPORT
2b. DECLASSIFICATION/DOWNGRADING SCHEDULE	Approved for public release; distribution unlimited

4. PERFORMING ORGANIZATION REPORT NUMBER(S)	5. MONITORING ORGANIZATION REPORT NUMBER(S) R&D 4759-CH-01

6a. NAME OF PERFORMING ORGANIZATION Tel Aviv University	6b. OFFICE SYMBOL (If applicable)	7a. NAME OF MONITORING ORGANIZATION USARDSG(UK)

6c. ADDRESS (City, State, and ZIP Code) Ramat Aviv 69978 Tel Aviv Israel	7b. ADDRESS (City, State, and ZIP Code) Box 65 FPO New York 09510-1500

8a. NAME OF FUNDING/SPONSORING ORGANIZATION USARDSG(UK)	8b. OFFICE SYMBOL (If applicable) AMXSN-UK-RC	9. PROCUREMENT INSTRUMENT IDENTIFICATION NUMBER DAJA45-85-C-0008

8c. ADDRESS (City, State, and ZIP Code) Box 65 FPO New York 09510-1500	10. SOURCE OF FUNDING NUMBERS			

	PROGRAM ELEMENT NO.	PROJECT NO.	TASK NO.	WORK UNIT ACCESSION NO.
	61103A	1L161103BH57	08	DA312139

11. TITLE (Include Security Classification)

(U) Excited State Energetics and Dynamics of Large Molecules, Complexes and Clusters

12. PERSONAL AUTHOR(S)
J. Jortner

13a. TYPE OF REPORT Final	13b. TIME COVERED FROM May 85 TO Jul 88	14. DATE OF REPORT (Year, Month, Day) 1988, July	15. PAGE COUNT 13

16. SUPPLEMENTARY NOTATION

17. COSATI CODES			18. SUBJECT TERMS (Continue on reverse if necessary and identify by block number)
FIELD	GROUP	SUB-GROUP	
07	04		

19. ABSTRACT (Continue on reverse if necessary and identify by block number)

New techniques for spectroscopy in supersonic expansions and in the development of specific supersonic sources were developed, including vacuum ultraviolet absorption spectroscopy in supersonic expansions, development of conical nozzles for supersonic jets and pulse extraction mass spectrometer. Research has included studies of energetics of rydberg states of jet-cooled molecules, rydberg states of anthracene, intramolecular relaxation of rydberg states and interference effects between extravalence and intravalence molecular excitations. The rotational state dependence of intramolecular dynamics was investigated, as well as the coupling between intrastate vibrational energy redistribution and interstate electronic relaxation and the coriolis rotation-vibration coupling and intramolecular dynamics. Mediated intersystem crossing phenomenology, inverse isotope effects and microscopic level shifts were explored. Studies of fluorescence quantum yields for highly-excited states of large molecules and

20. DISTRIBUTION/AVAILABILITY OF ABSTRACT ☒ UNCLASSIFIED/UNLIMITED ☒ SAME AS RPT. ☒ DTIC USERS	21. ABSTRACT SECURITY CLASSIFICATION Unclassifed
22a. NAME OF RESPONSIBLE INDIVIDUAL Dr. Robert J. Campbell	22b. TELEPHONE (Include Area Code) 01-409 4423	22c. OFFICE SYMBOL AMXSN-UK-RC

DD FORM 1473, 84 MAR
83 APR edition may be used until exhausted.
All other editions are obsolete.

photoisomerization dynamics of selected molecules were conducted, including an examination of energy-resolved photoisomerization rates and excited state energetics of van der Waals complexes and porphyrins. Large van der Waals complexes consisting of rare-gas (R) and atom(s) bound to a large aromatic molecule (M) were studied by fluorescence excitation and by two-photon, two-color spectroscopy in conjunction with mass-resolved detection. Information on the coupling between intramolecular and intermolecular nuclear motion in complexes was obtained. The analogies between the characteristics of large van der Waals M·Rn complexes and R atoms on graphite surfaces were explored, focusing on structure, packing, orientational registry effects and the nuclear motion of R adsorbates on finite microsurfaces. A theoretical study of the structure, energetics and dynamics of an excess electron interacting with an alkali-halide cluster has been provided. Further studies involved an exploration of vibrational predissociation induced by exciton trapping in rare-gas clusters and an investigation of nonreactive and reactive excited-state dynamics in mixed rare-gas clusters.

(Israel, edc)

C O N T E N T S

-----oOo-----

F I N A L   R E P O R T

1. Title: EXCITED-STATES ENERGETICS AND
                                             DYNAMICS OF LARGE MOLECULES,
                                             COMPLEXES AND CLUSTERS

2. Principal Investigator: Professor Joshua Jortner

3. Associate Investigator: Professor Uzi Even

4. Contractor: School of Chemistry
                                             Tel Aviv University
                                             69 978 Tel Aviv
                                             Israel

5. Contract No.:   DAJA45-85-C-0008

6. PROGRESS IN TECHNICAL APPROACH

New techniques for spectroscopy in supersonic expansions and in the development of specific supersonic sources were developed.

6.A **Vacuum Ultraviolet Absorption Spectroscopy in Supersonic Expansions.** We have combined the techniques of vacuum ultraviolet (VUV) spectroscopy together with planar supersonic jets, which allows for the interrogation of absorption spectra of large molecules cooled in supersonic expansions in the near VUV region. The experimental setup consists of a high pressure Xe lamp, CaF_2 optics, a vacuum ultraviolet spectrograph and a nozzle slit (0.27x90 mm, repetition rate 9 Hz and gas pulse duration 300 μsec). The characteristics of this spectroscopic setup are: (i) Energy range 6-10 eV. (ii) Spectral resolution 0.1 Å. (iii) Routine measurements of high-energy absorption spectra. (iv) Interrogation of fluorescence excitation spectra of the parent molecule or its photoproducts with limiting quantum yields of $Y \geq 10^{-4}$.

6.B **Development of Conical Nozzles for Supersonic Jets.** Conical nozzles (nozzle opening angle $\theta = 30°$, and nozzle diameter $D = 0.3$ mm) were constructed and used in conjunction with a magnetic pulsed valve. The use of conical nozzles considerably enhances clustering in supersonic expansions, facilitating studies of large van der Waals complexes and clusters.

6.C **Pulse Extraction Mass Spectrometer.** This setup is characterized by a mass resolution of $\Delta m/m = 10^{-2}$ and allows for the measurements of high ion masses up to $m = 2000$ in supersonic jets. The ions of large molecules and of large clusters, e.g., $tetracene \cdot Ar_{30}^+$, are produced by two-photon two-color ionization.

7. ACCOMPLISHMENTS OF OBJECTIVES

7.A **Energetics of Rydberg States of Jet-Cooled Molecules.** VUV absorption spectra of benzene, benzene-D_6 and naphthalene cooled in planar supersonic expansions were measured over the range 2000-1600 Å, providing evidence on energetics, line broadening and interference effects.

7.B   **Rydberg States of Anthracene.** Several Rydberg transitions
of jet-cooled anthracene were observed in the spectral region
1900-2000 Å. These Rydbergs are superimposed on a broad
"background" of $\pi\pi^*$ transitions. Up to now no fluorescence
from Rydberg states of polyatomic molecules has been reported.
The 1997 Å n=3 Rydberg of anthracene reveals fluorescence
with a quantum yield of $\sim$ 5%. This fluorescence originates
from internal conversion R $\leadsto$ S_1 followed by $S_1 \longrightarrow S_0$ emission,
as documented by the spectral distribution of the dispersed
fluorescence.

7.C   **Intramolecular Relaxation of Rydberg States.** Information on
intramolecular dynamics of extravalence excitations of benzene
was obtained from lineshape analysis. The lineshape of the
$^3P_{xy}(0)$ Rydberg is Lorentzian, whose homogeneous width result
in the lifetime $\tau =$ 0.19±0.02 psec for C_6H_6 and $\tau \simeq$ 0.22±0.02
psec for C_6D_6. Semiquantitative information on the lifetimes
of some Rydbergs of anthracene was obtained, which fall in the
range of $\sim$ 0.1 psec. These lifetime data imply that (i) the
relaxation of the Rydberg is characterized by moderate energy
gap(s), and (ii) the electronic relaxation rate of the Rydberg
is considerably less efficient than that of the intravalence
excitation in the same energy domain.

7.D   **Interference Effects between Extravalence and Intravalence
Molecular Excitations.** We have searched for Rydberg-valence
interference effects in large molecules, which are expected to
be exhibited in asymmetric Fano-type lineshapes in absorption.
For "isolated" Rydbergs, which are superimposed on a $\pi\pi^*$ tran-
sition in benzene, naphthalene and anthracene, the absorption
lineshapes are symmetric Lorentzians. No line asymmetry and
no antiresonances characteristic of Fano profiles were found
in that case. The absence of interference effects in this case
reveals the manifestation of random interstate coupling of R
with the π^* manifold. The random coupling erodes all inter-
ference effects. The situation is different for nearly lying
Rydbergs, where pronounced R-R-valence interference effects
were observed in the absorption spectra of jet-cooled naphtha-
lene in the spectral region 1600-1650 Å, providing information
on the homogeneous contribution to high-energy molecular coupl-
ing phenomena.

7.E **Rotational State Dependence of Intramolecular Dynamics.** Rotational effects on interstate coupling are of considerable current interest. Absolute fluorescence quantum yields from photoselected rotational states were measured for the electronic origins of the S_1 state of pyrazine. Strong rotational state dependence was observed providing novel information on interstate coupling for the intermediate level structure. This unique information cannot be extracted from time-resolved decay lifetimes.

7.F **The Coupling between Intrastate Vibrational Energy Redistribution and Interstate Electronic Relaxation.** We have documented some universal characteristics of the decay lifetimes and fluorescence quantum yields from the S_1 manifold of large molecules, which originate from the coupling between intrastate vibrational energy redistribution and interstate electronic relaxation. The time-resolved total fluorescence decay excited by a psec laser from the S_1 state of jet-cooled 9CN-anthracene exhibits nonexponential decay in the energy range $E_V = 1200$-1740 cm^{-1} above the S_1 origin, which does not originate from dephasing but rather manifests the effects of intrastate intermediate level structure for vibrational energy redistribution on intersystem crossing.

7.G **Coriolis Rotation-Vibration Coupling and Intramolecular Dynamics.** We have demonstrated that rotational effects play a central role on intramolecular vibrational energy redistribution in electronic-vibrational excitations of large molecules. Strong rotational effects on the fluorescence quantum yields from vibrational states (above 1000 cm^{-1}) in the S_1 manifold of 9-cyanoanthracene were observed, which demonstrate that Coriolis interactions serve as the dominant coupling leading to intramolecular vibrational energy redistribution (IVR). In contrast to common wisdom, which attributed IVR in large molecules to anharmonic interactions, we have shown that rotational effects play a central role strongly enhancing interstate electronic relaxation.

7.H **Resonances in Mediated Intersystem Crossing.** The mechanisms of direct and of mediated intersystem crossing from the first excited singlet manifold of anthracene and some of its derivatives were explored by the study of the internal and the external heavy atom effect on the fluorescence quantum yields. Pronounced mode selectivity was observed in the vibrational energy dependence of the emission quantum yield in 9-bromoanthracene and 9,10-dibromoanthracene

7.1 <u>Mediated Intersystem Crossing Phenomenology, Inverse Isotope Effects and Microscopic Level Shifts</u>. We explored the energy dependence of the interstate electronic relaxation rates, k_{nr}, from the S_1 manifold of anthracene and seven of its isotopic and chemical derivatives, which were inferred from quantum yield data. Absolute fluorescence quantum yields, Y, from groups of rotational states within the electronic origin $S_1(0)$ and from vibrational states were obtained over the excess energy E_v = 0-3000 cm^{-1} above $S_1(0)$ by the simultaneous interrogation of the fluorescence excitation spectra and of the absorption spectra in seeded, pulsed, planar supersonic jets of Ar. Additional information was obtained from quantum yield data of van der Waals (vdW) complexes of these molecules with Ar. The fluorescence quantum yields from the $S_1(0)$ of anthracene, 9-cyanoanthracene and 9,10-dibromoanthracene were found to be independent of the rotational state, providing further evidence for the rotational independence of k_{nr} from a single doorway state. From the Y data of the electronic origins and from the E_v dependence of Y, we conclude that intersystem crossing (ISC) dynamics of the S_1 manifold is dominated by the interplay between two classes of nonreactive coupling and/or relaxation. (i) Interstate coupling, involving the superposition of direct $S_1 \rightarrow (T_x)$ ISC together with $S_1 - (T_x) \rightarrow (T_1)$ mediated ISC through a sparse or dense (T_x) manifold of a higher triplet state. (ii) Intrastate coupling within the S_1 manifold, which sets in with increasing E_v and which results in intramolecular vibrational energy redistribution (IVR) at high E_v. The dominant role of mediated interstate coupling in ISC dynamics from $S_1(0)$ and from low E_v states was inferred from the inverse deuterium isotope effect on the ISC rates, the extreme sensitivity of k_{nr} of deuterated anthracene to a single H atom substitution, and to level shifts induced by complexing with Ar, as well as from the three orders of magnitude difference between the k_{nr} values from the $S_1(0)$ of 9-bromoanthracene and of 9,10-dibromoanthracene. The onset of the mediated ISC is documented by an abrupt drop of Y in the narrow (E_v = 617-805 cm^{-1}) energy range for 9,10-dichloroanthracene and by the oscillatory energy dependence of Y versus E_v and the extreme energy sensitivity of Y in the range E_v = 157-800 cm^{-1} of 9,10-dibromoanthracene which is attributed to near-degeneracies between S_1 states and the mediating (T_x) states. These resonance effects can be drastically modified by dispersive level shifts induced by complexing with Ar. At high excess vibrational energies some universal features of the E_v dependence of k_{nr} are exhibited. These involve a gradual increase of k_{nr} with increasing E_v at medium energies (E_v = 1000-1800 cm^{-1}), which correspond to the intermediate level structure for intrastate coupling, and a very weak E_v dependence of k_{nr} at high energies (E_v = 1800-3000 cm^{-1}), which manifest the effect of statistical intrastate IVR on interstate ISC.

7.J <u>Fluorescence Quantum Yields for Highly-Excited States of Large Molecules.</u> Fluorescence quantum yields Y from high electronic excitations of naphthalene, anthracene and tetracene in the energy range 5.0-6.5 eV have been recorded. Y exhibits an exponential dependence on the excess vibrational energy with the slope decreasing with increasing size of the molecule, i.e., the vibrational density of states. These data are characteristic of internal conversion from S_1 to S_0. These results are of interest regarding recent astrophysical implications of high-energy photophysics of large aromatic hydrocarbons in outer space.

7.K <u>Photoisomerization Dynamics of Trans-Stilbene and of Cis-Stilbene.</u> Time-resolved fluorescence lifetimes from photoselected states of trans-stilbene were recorded by the techniques of picosecond spectroscopy in jets using a mode-locked dye laser and a fast photon counting system. Decay lifetimes as short as 100±30 psec were recorded Extensive information on the energy dependence of the isomerization rates of alkyl stilbenes was obtained, providing information on the role of intramolecular vibrational distribution on the photochemistry in an isolated molecule. The absorption spectrum of jet-cooled cis-stilbene is broad and no vibrational structure could be resolved due to the congestion of broadened low-frequency vibrational excitation. From the low quantum yield $Y \leqslant 2\times10^{-4}$ we infer a S_1 lifetime of $\tau \leqslant 0.4$ psec, which indicates ultrafast relaxation of this molecule.

7.L <u>Photoisomerization Dynamics of Alkyl Substituted Trans-Stilbene.</u> A central issue pertaining to isolated-molecule photochemistry involves the role of intramolecular vibrational relaxation in determining intramolecular dynamics. We have attempted to increase the density of vibrational states by alkyl substitution of trans-stilbene and have explored the isomerization dynamics by picosecond time-resolved spectroscopy. We have obtained the counter-intuitive result that alkyl substitution of trans-stilbene enhances the photoisomerization rates, while general arguments based on the role of IVR and the implications of statistical theories indicate that the rate should be retarded. The results can be accounted for by the modification of the molecular parameters, i.e., threshold energy, by alkyl substitution.

7.M   <u>Energy-Resolved Photoisomerization Rates</u>. The dynamics of the S_1 and S_2 electronically excited singlet states of *diphenylbutadiene* was interrogated by fluorescence quantum yield measurements over the very broad energy domain of 0-7500 cm^{-1} above the (false) S_1 origin. The issues of the lack of mode selectivity and the applicability of statistical theories for the description of isolated-molecule photochemistry were explored.

7.N   <u>van der Waals Complexes and Porphyrins</u>. Excited-state energetics and dynamics of large complexes consisting of porphyrins bound to rare-gas atoms were explored. Detailed spectroscopic information on the $S_0 \rightarrow S_1$ and $S_0 \rightarrow S_2$ transitions of the free-base porphine·Ar complex was obtained, providing insight into the structure of this complex, as well as resulting in a novel mechanism for microscopic solvent shifts induced by configurational distortions, which are due to complexing.

7.O   <u>Molecular and Metallic van der Waals Complexes</u>. Large van der Waals complexes consisting of rare-gas (R) and atom(s) bound to a large aromatic molecule (M) were studied by fluorescence excitation and by two-photon, two-color spectroscopy in conjunction with mass-resolved detection. These studies provided information on spectral shifts of the S_1 level and of the ionization potential for tetracene·Ar (n=1-5) complexes, providing central information on microscopic solvent shifts. These studies were extended to M-metal atom complexes, such as pyrene·Hg_n (n=1,2), which constitute a new method for the creation of metallic microclusters supported on a "microspace". The electronic-vibrational spectroscopy of M·R complexes provide information on large amplitude intermolecular nuclear motion of rare-gas atoms on microsurfaces, which pertain to the interesting analogy between large van der Waals molecules and microsurfaces.

7.P   <u>Coupling between Intramolecular and Intermolecular Nuclear Motion in Complexes</u>. Intermolecular vibrations of large van der Waals complexes, which involve the motion of the ligand relative to the large molecule, provide an analogue for surface vibrational motion in a finite system and constitute the precursors of phonon modes in condensed phases. Information on the coupling between intermolecular and intramolecular vibrational motion was obtained for the trans-stilbene·Ar complex.

INTERSTATE COUPLING AND DYNAMICS OF EXCITED SINGLET STATES OF ISOLATED DIPHENYLBUTADIENE

Aviv AMIRAV, Mark SONNENSCHEIN and Joshua JORTNER

Department of Chemistry, Tel Aviv University, 69978 Tel Aviv, Israel

In this paper, we report on absolute fluorescence quantum yields from photoselected vibrational states of jet-cooled 1,4-diphenylbutadiene for excess vibrational energies, $E_V \approx 0-7500$ cm^{-1}, above the apparent electronic origin of the $S_1(2A_g)$ state. The pure radiative lifetimes, τ_r, of the strongly scrambled $S_2(1B_u)-S_1(2A_g)$ molecular eigenstates ($E_V = 1050-1800$ cm^{-1}) show a marked dilution effect, ($\tau_r/\tau_r(S_2) \approx 40$), being practically identical with the τ_r values from the $S_1(2A_g)$ manifold ($E_V = 0-900$ cm^{-1}), which is affected by near-resonant vibronic coupling to $S_2(1B_u)$ and exhibiting the dynamic manifestations of the intermediate level structure. Isomerization rates in the isolated molecule, which do not exhibit vibrational mode selectivity, were recorded over the energy range 0-6600 cm^{-1} above the threshold.

INTERSTATE COUPLING AND DYNAMICS OF EXCITED SINGLET STATES OF ISOLATED DIPHENYLBUTADIENE

Aviv AMIRAV, Mark SONNENSCHEIN and Joshua JORTNER

Department of Chemistry, Tel Aviv University, 69978 Tel Aviv, Israel

In this paper, we report on absolute fluorescence quantum yields from photoselected vibrational states of jet-cooled 1,4-diphenylbutadiene for excess vibrational energies, E_V = 0–7500 cm^{-1}, above the apparent electronic origin of the $S_1(2A_g)$ state. The pure radiative lifetimes, τ_r, of the strongly scrambled $S_2(1B_u)$–$S_1(2A_g)$ molecular eigenstates (E_V = 1050–1800 cm^{-1}) show a marked dilution effect, ($\tau_r/\tau_r(S_2) \approx 40$), being practically identical with the τ_r values from the $S_1(2A_g)$ manifold (E_V = 0–900 cm^{-1}), which is affected by near-resonant vibronic coupling to $S_2(1B_u)$ and exhibiting the dynamic manifestations of the intermediate level structure. Isomerization rates in the isolated molecule, which do not exhibit vibrational mode selectivity, were recorded over the energy range 0–6600 cm^{-1} above the threshold.

1. Introduction

Excited-state energetics and dynamics of linear polyenes [1], which have been investigated for more than three decades [2], are of considerable interest with regard to their intramolecular isomerization photochemistry, their relevance to the process of vision, and in serving as model systems for the elucidation of electronic structure and vibronic coupling in conjugated organic molecules. With the advent of modern techniques of spectroscopy in supersonic jets [3], the electronic level structure and intramolecular relaxation of isolated polyenes because amenable to experimental interrogation [4–20]. Recent studies reported on the electronic level structure of some isolated polyenes, i.e., butadiene [4,10–15], hexatriene [11–13] and 1,3,5,7-octateraene [5,12], and on the level structure and dynamics of isolated diphenyl polyenes, i.e., trans-stilbene [14–20], 1,4-diphenylbutadiene [6,7] and 1,6-diphenyl-1,3,5-hexatriene [9] in supersonic jets. A series of interesting issues can be addressed that pertain to:

(1) The ordering of the electronically excited states [1,4–14,16].

(2) Electronic energy gap effects on pure radiative lifetimes.

(3) Interstate S_2–S_1 mixing and non-reactive dynamics.

(4) Reactive isomerization dynamics [7,8,14–20].

(5) Electronic structure and isomerization dynamics.

(6) Mode specificity or statistical characteristics of photoisomerization.

Concerning point (1), a detailed picture emerged on the basis of the vibrational level structure [4–14,16], relative intensities of distinct electronic transitions [6–13] and two-photon spectroscopy [7] in jets. While for trans-stilbene [14–20] and cis-stilbene [21], the lowest spin-allowed electronic transition involves $A_g \rightarrow B_u$, the two lowest electronic transitions in longer diphenyl polyenes [1,6–9] are $S_0(1A_g) \rightarrow S_1(2A_g)$ and $S_0(1A_g) \rightarrow S_2(1B_u)$. This ordering of the energy levels [1] provides the basis for the elucidation of non-reactive and reactive dynamics. Regarding reactive dynamics [point (4)], recent time-resolved [7,14,18–20] and energy-resolved [15,16] data provided insight into photo-isomerization in isolated diphenyl polyenes. Relatively little is known on interstate coupling [point (3)] in these systems. The complex level structure of the $S_0(1A_g) \rightarrow S_2(1B_u)$ transition in diphenylbutadiene [6,7] exhibits the spectroscopic manifestations of the intermediate

level structure [22,23] for the $S_2(1B_u)-S_1(2A_g)$ coupling, while the extreme line broadening of the $S_0(1A_g) \rightarrow S_2(1B_u)$ transition in diphenyl hexatriene [9] seems to be on the verge of the statistical limit. Absolute fluorescence quantum yield data of polyenes in supersonic expansions which provide information on the pure radiative lifetimes, are expected to elucidate some dynamic aspects of $S_2(1B_u)-S_1(2A_g)$ coupling in these molecules. Furthermore, such energy-resolved quantum yields are pertinent for the interrogation of the dynamics and for the search for mode specificity in the reactive photo-isomerization process over a broad energy range [15]. With these goals in mind, we have measured absolute fluorescence quantum yields from photoselected states of jet-cooled 1,4-diphenylbutadiene (DPB) over the excess energy range $E_V = 0-7500$ cm^{-1} above the first apparent electronic origin of the $S_0(1A_g) \rightarrow S_1(2A_g)$ transition.

2. Experimental

Our experimental techniques [15,27–29] for the measurement of absolute fluorescence quantum yields from jet-cooled large molecules have been described previously. Briefly, the absorption spectra and the fluorescence excitation spectra of DPB seeded in pulsed planar supersonic expansions were simultaneously determined using a pulsed xenon lamp and a monochromator. DPB was heated in the nozzle chamber to 130°C, mixed into Ar (stagnation pressures $p = 30-50$ Torr) or Ne ($p = 100-150$ Torr), and expanded through a nozzle slit (dimensions 0.27×90 mm, repetition rate 6 Hz and gas pulse width 300 μs). Light from a pulsed simmered Xe flashbulb (pulse duration 24 μs) was passed through an 0.75 M Spex monochromator (with a 2400 lines/mm grating and 3 cm^{-1} resolution at 6 μm slit width) and focused onto the jet parallel to the slit at a distance of $x = 10$ mm from it. The light beam was split by a sapphire window and monitored by two vacuum photodiodes. The attenuation ΔI of the light beam due to absorption was determined from the difference in the light intensity before and after crossing the planar jet. The lamp-induced fluorescence (LMIF) inten-

sity I_F was monitored by a photomultiplier. The absorption signal ΔI and the LMIF signal I_F were normalized to the incident light intensity I_0. The relative quantum yield, q, is given by $q = I_F/\Delta I$. Absolute quantum yields, Y, were obtained by measuring the quantum yields simultaneously from DPB excited at 3256 Å and from the S_1 electronic origin of anthracene (at 3610 Å) in an expansion containing both molecules. The quantum yield from the S_1 origin of the reference molecule was taken to be 0.67 [29]. In this manner, the q scale of DPB was calibrated to give Y data from photoselected vibrational states for excess vibrational energies E_V above the lowest-energy spectral feature of $E_V = 0-7500$ cm^{-1}.

The fluorescence excitation and absorption spectra of DPB were studied in expansions of seeded Ne ($p = 150$ Torr) and of Ar ($p = 30-50$ Torr). The spectra and the fluorescence quantum yields obtained under these expansion conditions were independent of the nature of the diluent corresponding to the bare molecule. At higher stagnation pressures of Ar ($p = 80-150$ Torr) the contributions of van der Waals DPB $\cdot$ Ar$_n$ complexes became significant. The spectroscopic manifestations of complexing involve the blurring of the intense, irregular, closely spaced structure in the range 3200–3240 Å. The fluorescence quantum yield in the range $\lambda < 3300$ Å from DPB expanded in Ar ($p = 80-150$ Torr), containing DPB $\cdot$ Ar$_n$ complexes, is considerably higher than that of the bare molecule which was cooled in Ne. This increase of Y is tentatively attributed to vibrational predissociation of DPB $\cdot$ Ar$_n$, or/and intramolecular vibrational energy flow from the intramolecular vibration of DPB to intermolecular DPB---Ar modes within the complex. All the spectroscopic and dynamic data for the bare DPB molecule reported in this work were obtained in expansions of seeded Ne ($p = 150$ Torr).

3. Spectra

The lamp-induced fluorescence (LMIF) and absorption spectra of DPB over a broad energy region are portrayed in fig. 1. These bare molecule spectra reveal three regions:
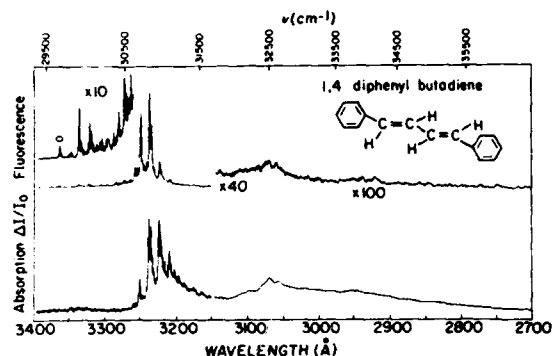
Fig. 1. Absorption spectrum (lower curve) and fluorescence excitation spectrum (upper curve) of DPB over the spectral range 2700–3400 Å. DPB was heated in the nozzle chamber to 140°C, seeded into Ne ($p = 150$ Torr) and expanded through the nozzle slit. The light beam crossed the planar jet at $x = 10$ mm from the nozzle. The apparent origin of the $S_0(1A_g) \to S_1(2A_g)$ transition is marked 0.

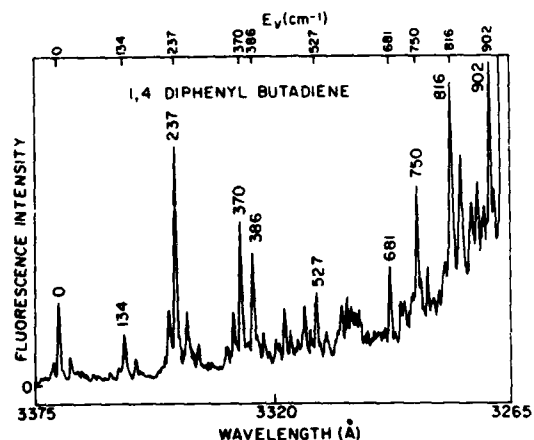Fig. 2. The fluorescence excitation spectrum of DPB in the range 3265–3375 Å, exhibiting the $S_0(1A_g) \to S_1(2A_g)$ electronic transition. Experimental conditions as in fig. 1. The apparent electronic origin is marked 0, while the numbers mark the excess vibrational energies (in cm^{-1}).

(1) The lowest-energy weak $S_0(1A_g) \to S_1(1A_g)$ transition (fig. 2) has its apparent electronic origin [7] at 3370 Å (29673 cm^{-1}), which is in accord with the results of Heimbrook et al. [6] and of Shepanski et al. [7]. The vibrational level structure of this transition (fig. 3), exhibiting excitations at 134, 237, 370, (134 + 237) and 370 cm^{-1} above the apparent origin, is in perfect agreement with previous work [7].

(2) The second $S_0(1A_g) \to S_2(1B_u)$ intense electronic transition sets in at the vicinity of 3240 Å (fig. 3) and is also in agreement with previous work [6,7]. This transition in the range 3180–3240 Å exhibits an irregular closely spaced structure which clearly corresponds to the intermediate level structure [22–26] originating from strong interstate $S_2(1B_u)–S_1(2A_g)$ mixing. As the electronic energy gap ΔE between the electronic origin of the two electronic configurations is low, $\Delta E(S_2–S_1) \approx 1000$ cm^{-1}, the spectroscopic manifestations of $S_2–S_1$ interstate coupling in DPB are analogous to those exhibited in the S_2 state of jet-cooled naphthalene [25], pyrene [30] and ovalene [31], all of which are characterized by a low electronic energy gap. A comparison between the relative intensities of the irregular, closely spaced, distinct spectral features in the fluorescence excitation and absorption spectra in the range 3180–3240 Å reveals a gradual
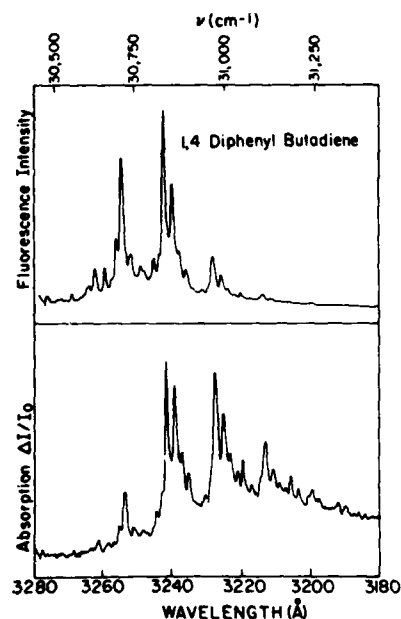

Fig. 3. The absorption (lower curve) and the fluorescence excitation (upper curve). Spectra of DPB in the spectral range 3180–3280 Å. Experimental conditions as in fig. 1. This spectrum for the $S_0(1A_g) \to S_2(1B_u)$ transition exhibits the features of the intermediate level structure for $S_2–S_1$ mixing, as well as a monotonical decrease of Y with increasing E_V.

and monotonical decrease of the fluorescence quantum yield with increasing energy. No vibrational mode selectivity of the yield is exhibited in this energy domain.

(3) The "quasicontinuum". In the energy range 2700–3150 Å, i.e., $E_V = 2000$–8000 cm^{-1} (fig. 1), the absorption and LMIF spectra of the jet-cooled molecule are devoid of any vibrational structure. A cursory examination of fig. 1 reveals that in this energy range the quantum yield for fluorescence exhibits a marked decrease with increasing E_V. Such a quasicontinuum was observed also in the electronically excited manifold of trans-stilbene [14,15,18], while there is no evidence for the observation of such a quasicontinuum in the ground S_0 electronic state of trans-stilbene [14,18]. It is plausible that this excited-state quasicontinuum exhibited at high E_V provides a spectroscopic manifestation of intramolecular isomerization in the isolated molecule. A cursory examination of the fluorescence excitation and absorption spectra within the "quasicontinuum" (fig. 1) reveals again a gradual and monotonical decrease of the fluorescence quantum yield with increasing excess vibrational energy. As the spectra of the isolated internally cold molecule are devoid of any structure within the "quasicontinuum", it is not surprising that the fluorescence quantum yield does not exhibit any vibrational mode selectivity within this energy range.

4. Quantum yields

The absolute quantum yield data over the range $E_V = 0$–7500 cm^{-1} above the $S_1(1A_g)$ apparent origin (fig. 4) reveal the following features in the order of increasing energy: (a) a modest decrease with increasing E_V in the range $E_V = 0$–1050 cm^{-1}, (b) a break at $E_V = 1050$ cm^{-1}, (c) a sharp decrease of Y by about two orders of magnitude over the narrow energy range, $E_V = 1050$–2000 cm^{-1}, and (d) a further and more moderate decrease of Y with increasing E_V in the range $E_V = 2000$–7500 cm^{-1}. Features (a)–(c) in the Y data show a similar trend to that exhibited by the lifetime data of Zewail et al. [8]. Feature (a) presumably reveals modest intersystem crossing, ex-
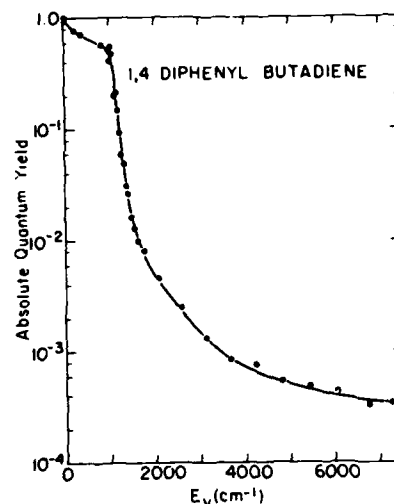
Fig. 4. Absolute fluorescence quantum yields from photo-selected states of DPB for excess vibrational energies $E_V = 0$–7500 cm^{-1}.

hibiting interstate, non-reactive, electronic relaxation. Reactive dynamics is exhibited at higher energies. Feature (b) presumably marks the onset of isomerization, which prevails in regions (c) and (d).

Two features of the intramolecular isomerization within the isolated DPB molecule should be noted. (I) The onset of isomerization at $E_V \approx 1050$ cm^{-1} [feature (b)] practically coincides with the onset of the second, spin-allowed electronic transition, which sets in at $E_V \approx 1000$ cm^{-1}. We believe that this apparent correspondence between dynamics and the spectroscopic level structure is coincidental as, in views of the heavy S_2–S_1 mixing (see the discussion in section 7), the S_2 states lose their identity. (II) As is evident from the foregoing discussion of the spectra (section 3) and from the quantitative Y data (fig. 4), the quantum yields for isomerization, which prevails in regions (a) and (d), reveal a smooth Y versus E_V dependence and no vibrational mode selectivity of the "reactive" intramolecular process is exhibited.

5. Pure radiative lifetimes

The combination of our quantum yield data with the time-resolved data of Shepanski et al. [7],

Fig. 5. The energy dependence of the pure radiative lifetimes of DPB over the energy range $E_v = 0$-1800 cm^{-1}. The absolute fluorescence 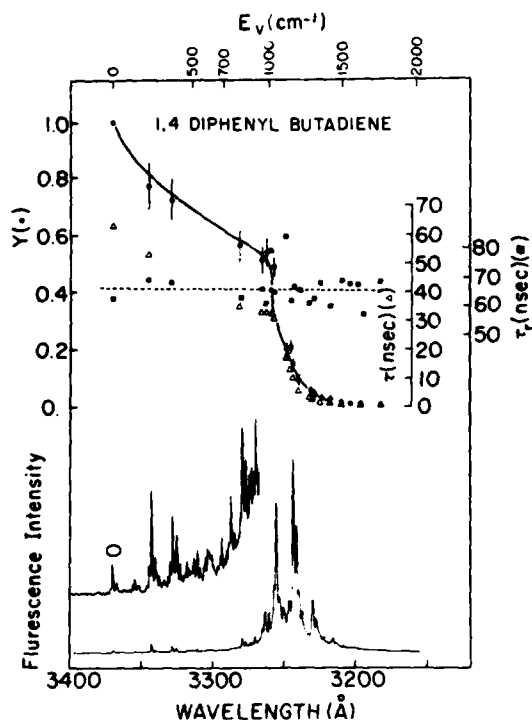quantum yields (●) from the present work were combined with the experimental decay lifetimes (△) of Shepanski et al. [7] to give the τ_r values (■). In the lower part of the figure the LMIF spectrum is displayed revealing two electronic transitions in this energy range.

and of Heimbrook et al. [6] provides new information on the pure radiative lifetimes of the $2A_g$ and $1B_u$ states. Fig. 5 portrays the Y data together with Shepanski's experimental decay lifetimes, τ, [7] over the energy range $E_v = 1$-1800 cm^{-1}, which spans the two $S_0 \to S_1$ and $S_0 \to S_2$ electronic transitions. From these data, we have evaluated the pure radiative lifetimes $\tau_r = Y\tau$. The pure radiative lifetimes from the $S_1(2A_g)$ manifold ($E_v = 0$-900 cm^{-1}) are $\tau_r = 65 \pm 5$ ns (fig. 5). The τ_r values obtained for the radiative decay of molecular eigenstates (MEs), which involve the scrambling of the $S_2(1B_u)$ origin and/or its low vibronic excitations with the $S_1(2A_g)$ background states in the energy range $E_v = 1000$-1800 cm^{-1} are practi-

cally constant assuming the value $\tau_r = 65 \pm 5$ ns (fig. 5).

6. Radiative lifetime of S_1

The pure radiative lifetime $\tau_r(S_1) = 65 \pm 5$ ns of the states in the $S_1(2A_g)$ manifold ($E_v = 0$-900 cm^{-1}) are surprisingly short for a weakly allowed, vibronically induced transition. The pure radiative lifetime of $S_1(2A_g)$ inferred from the integrated oscillator strength is considerably longer than the experimental value of $\tau_r(S_1)$.

To provide a spectroscopic estimate of the pure radiative lifetime of the $S_1(1A_g)$ state, we have evaluated the relative integrated intensities in the absorption spectra of the $S_0(1A_g) \to S_1(2A_g)$ transition (spectral range 3260–3362 Å) and of the $S_0(1A_g) \to S_1(2A_g)$ transition (spectral range 3180–3250 Å) of the jet-cooled molecule. The absorption intensity of the $S_0(1A_g) \to S_1(2A_g)$ transition was obtained from the LMIF spectra in conjunction with the quantum yield data, while the absorption intensity of the $S_0(1A_g) \to S_1(1B_u)$ transition was taken from figs. 1 and 3. This estimate results in the oscillator strength ratio $f(S_0 \to S_2)/f(S_0 \to S_1) = 150$. In view of the effects of interstate coupling, which are manifested by the appearance of the irregular quasi-lorentzian onset of the $S_2 + S_1$ MEs (figs. 1 and 5) in the range 3320–3362 Å ($E_v = 700$-900 cm^{-1}), it appears that our estimate of $f(S_0 \to S_1)$ constitutes an upper limit for this observable and a lower limit for the oscillator strength ratio, i.e., $f(S_0 \to S_2)/f(S_0 \to S_1) \geqslant 150$. The ratio of the pure radiative lifetimes of the two electronic states of the isolated molecule $\tau_r(S_1)/\tau_r(S_2) = f(S_0 \to S_2)/f(S_0 \to S_1)$ is $\tau_r(S_1)/\tau_r(S_2) \geqslant 150$. The pure radiative lifetime of the $S_2(1B_u)$ state of DPB estimated from the integrated oscillator strength in solution is $\tau_r(S_2) = 1.5$ ns [31], being close to the pure radiative lifetime $\tau_r = 2.5$ ns of the $1B_u$ state of isolated trans-stilbene [14–20]. Accordingly, the spectroscopic estimate of the pure radiative lifetime of the $S_1(2A_g)$ state of DPB is $\tau_r(S_1) \geqslant 225$ ns, which is considerably longer than the experimental value (fig. 5) $\tau_r = 65 \pm 5$ ns. The origins of the apparent shortening of $\tau_r(S_1)$, which may originate from

near-resonant vibronic coupling, i.e., pseudo-Jahn–Teller effects as well as from configurational changes in S_1, remain to be explored.

7. Interstate S_2–S_1 coupling

Novel information concerning $S_2(1B_u)$–$S_1(2A_g)$ interstate coupling emerges from the τ_r data. The τ_r values for the $S_2 + S_1$ MEs in the energy range $E_V = 1000$–1800 cm^{-1} (fig. 5) exhibit the following features:

(1) The τ_r values are practically constant in this energy range, where both τ [7] and Y sharply decrease with increasing E_V.

(2) The values of $\tau_r = 65 \pm 5$ ns are very close to the pure radiative lifetimes of the vibronic levels in the $S_1(1A_g)$ manifold.

(3) The τ_r values of the MEs are appreciably longer than the pure radiative lifetimes $\tau_r(S_2)$ estimated from the integrated strength for the $S_0(1A_g) \rightarrow S_2(1B_u)$ transition.

To provide a quantitative estimate of the lengthening of τ_r, we follow the conventional procedure, evaluating the dilution factor $\tau_r/\tau_r(S_2)$. Utilizing the pure radiative lifetime of the $S_2(1B_u)$ state $\tau_r(S_2) = 1.5$ ns estimated [31] from the integrated oscillator strength in solution, we infer that the dilution factor is $\tau_r/\tau_r(S_2) = 40$. The appreciable lengthening of τ_r for the second excited singlet state, wich is characterized by $\tau_r \approx \tau_r(S_1)$ for the MEs of S_2 parentage, can be attributed to one of the following causes: (a) The dilution effect for strong S_2–S_1 mixing within the intermediate level structure (ILS) [22–26]. (b) $S_2 \rightarrow S_1$ intramolecular relaxation in the statistical limit [23], followed by the radiative decay of the isoenergetic S_1 manifold. Mechanism (b) is realized for large electronic S_2–S_1 energy gaps, whereupon the background density of states is very high, so that the level widths of the resulting MEs exceed their spacings. This state of affairs probably prevails for the decay of the S_2 state of diphenylhexatriene, where $\Delta E(S_2$–$S_1) \approx 3400$ cm^{-1} [9], and where the fluorescence decay lifetime from the S_2 origin is more than an order of magnitude longer than the pure radiative lifetime of the $S_2(1B_u)$ state. For the problem at hand, the electronic energy gap in DPB

$\Delta E(S_2$–$S_1) = 1000$ cm^{-1} is small, whereupon the ILS prevails, i.e., the MEs are well separated relative to the widths. The marked lengthening of τ_r is attributed to the dilution effect, which was previously documented in the S_2 state of jet-cooled naphthalene [25] and ovalene [26]. Using the vibrational frequencies of DPB [32], we estimate that the density of S_1 vibrational states at $\Delta E(S_2$–$S_1) = 1000$ cm^{-1} is $\rho \approx 10^3$ cm, which constitutes a rough estimate of the effectively coupled levels. Within the framework of the ILS model [22], the (average) pure radiative width, γ_m^{rad}, of an ME is $\gamma_m^{rad} = \gamma_s^{rad}/N + \gamma_\ell^{rad}$, where γ_s^{rad} and γ_ℓ^{rad} correspond to the pure radiative lifetimes of $S_2(1B_u)$ and $S_1(2A_g)$, respectively. N is the dilution factor, which is given by $N = 2\pi^2 V^2 \rho^2$. Expressing N in terms of $\Gamma = 2\pi V^2 \rho$, i.e., the mean energetic spread of MEs emerging from a single S_2 vibronic doorway state, and taking $\Gamma \approx 10$ cm^{-1} (fig. 2), we obtain the crude estimate $N \approx 10^4$. As $\gamma_s^{rad}/\gamma_\ell^{rad} = \tau_r(S_1)/\tau_r(S_2) \approx 40$, we expect on the basis of the relation $\gamma_m^{rad} = \gamma_\ell^{rad}(1 + \gamma_s^{rad}/\gamma_\ell^{rad}N)$, together with $\gamma_s^{rad}/\gamma_\ell^{rad}N \approx 4 \times 10^{-3}$, that $\gamma_m^{rad} \approx \gamma_\ell^{rad} \approx [\tau_r(S_1)]^{-1}$. Accordingly, the dilution of the S_2 levels among the MEs is so effective that the decay lifetimes of these MEs are essentially determined by their S_1 character.

8. Isomerization dynamics

Following conventional wisdom, we attribute the marked decrease of Y with increasing E_V over the broad region $E_V = 1050$–7500 cm^{-1} (fig. 3) to intramolecular isomerization [7]. The nature of the photoisomerization process in DPB has not yet been established. This radiationless process does not necessarily involve rotation above a double bond. An interesting alternative mechanism may involve electrocyclic ring closing. This cardinal issue deserves further study. From the quantum yield data, we have evaluated the ratio of the non-radiative decay rate, k_{nr}, and the radiative decay rate $k_r = \tau_r^{-1}$ from the relation $k_{nr}/k_r = (Y^{-1} - 1)$. These results are displayed in fig. 6. On the basis of the foregoing analysis of the pure radiative lifetimes (fig. 5) in the range $E_V = 0$–1800 cm^{-1}, which rests on our quantum yield data in
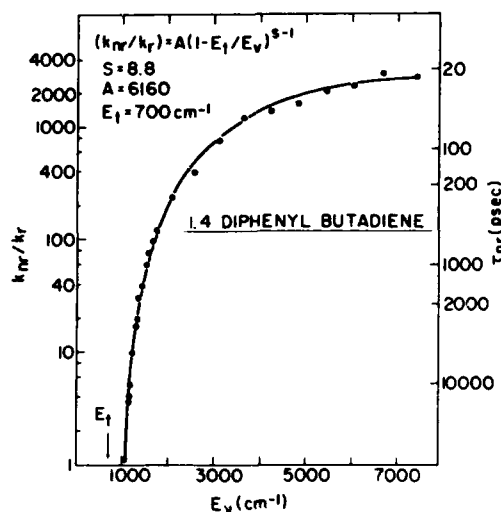
Fig. 6. The energy dependence of the relative non-reactive decay rate (k_{nr}/k_r) and of the non-reactive lifetime (τ_{nr}) for intramolecular isomerization within the isolated DPB in the range $E_V = 0–7500$ cm^{-1}. The solid line represents the best fit of the experimental data to the classial RRK theory with the parameters marked on the figure.

conjunction with the lifetime data [6,7], we can safely assert that $k_r = 1.5 \times 10^7$ s^{-1} over the entire energy region. The non-radiative lifetimes, τ_{nr}, for intramolecular isomerization extracted from our quantum yield data, which span the range $\tau_{nr} \approx 20–5 \times 10^5$ ps, are also presented in fig. 6. The lack of mode selectivity in the isomerization reaction (fig. 6) within the isolated molecule, already alluded to in section 4, points towards efficient vibrational energy redistribution preceding the reactive intramolecular process. This state of affairs is similar to that encountered previously for the decay of the intramolecular dynamics of trans-stilbene [14–20]. Obviously, the qualitative observations of a complete erosion of mode selectivity constitutes a necessary but by no means sufficient condition for the applicability of "statistical" theories of unimolecular reactions. In this context, we have attempted to provide a fit of our Y data in terms of the simple classical RRK equation. As is apparent from fig. 6, the dynamic data can be presented in terms of the classical RRK equation $k_{nr}/k_r = A(1 - E_t/E_V)^{s-1}$, with the threshold energy $E_t = 700$ cm^{-1}, the effective number of vibra-

tional degrees of freedom $s = 8.8$ and the pre-exponential factor $A = 6160$. As is well known, this classical RRK fit provides a low value of s and a lower limit for E_t. A cursory examination of the apparently low pre-exponential factor $\tilde{A} \approx Ak_r = 9 \times 10^{10}$ s^{-1} may indicate that the isomerization reaction in the isolated molecule is non-adiabetic. However, it has recently been pointed out by Troe [33] that the apparently low pre-exponential frequency factors originating from the analysis of isomerization dynamics in isolated diphenyl polyenes in terms of statistical unimolecular theories may be due to frequency changes between the reactant and the activated complex. For a "more rigid" set of activated complex frequencies, as compared to the molecular frequencies, the change in the vibrational entropy will reduce the frequency factor. The extremely good RRK fit (fig. 6) over a large energy range should be considered just as a convenient way of data representation and does not provide unambiguous mechanistic information regarding partial or complete vibrational energy redistribution and adiabaticity of the isomerization process in the isolated molecule.

Acknowledgement

References

[1] B.S. Hudson, B.E. Kohler and K. Schulter, Excited states, Vol. 3 (Academic Press, New York, 1982) p. 1.

[2] J. Dale, Acta Chem. Scand. 11 (1957) 971.

[3] D.H. Levy, Ann. Rev. Phys. Chem. 31 (1980) 197.

[4] V. Vaida and G.M. McClelland, Chem. Phys. Letters 71 (1980) 436.

[5] L.A. Heimbrook, J.E. Kenny, B.E. Kohler and G.W. Scott, J. Chem. Phys. 75 (1981) 4338.

[6] L.A. Heimbrook, B.E. Kohler and T.A. Spiglanin, Proc. Natl. Acad. Sci. US 80 (1983) 4580.

[7] J.F. Shepanski, B.W. Keelan and A.H. Zewail, Chem. Phys. Letters 103 (1983) 9.

[8] S.H. Courtney, G.R. Fleming, L.R. Khundkar and A.H. Zewail, J. Chem. Phys. 80 (1984) 4559.

[9] B.E. Kohler and T.A. Spiglanin, J. Chem. Phys. 80 (1984) 5465.

[10] D.G. Leopold, R.J. Hemley and V. Vaida, J. Chem. Phys. 75 (1981) 4758.

[11] R.J. Hemley, J.J. Dawson and V. Vaida J. Chem. Phys. 78 (1983) 2915.

[12] D.G. Leopold, V. Vaida and M.F. Granville, J. Chem. Phys. 81 (1984) 4210.

[13] D.G. Leopold, R.D. Pendley, J.L. Roebber, R. Hemley and V. Vaida, J. Chem. Phys. 81 (1984) 4218.

[14] J.A. Syage, W.R. Lambert, F.M. Felker, A.H. Zewail and R.H. Hochstrasser, Chem. Phys. Letters 88 (1982) 266.

[15] A. Amirav and J. Jortner, Chem. Phys. Letters 95 (1983) 295.

[16] T.S. Zweir, E. Carrasquillo and D.H. Levy, J. Chem. Phys. 78 (1983) 5493.

[17] J.W. Perry, N.F. Scherer and A.H. Zewail, Chem. Phys. Letters 103 (1983) 1.

[18] T.J. Majors, U. Even and J. Jortner, J. Chem. Phys. 81 (1984) 2330.

[19] J.A. Syage, P.M. Felker and A.H. Zewail, J. Chem. Phys. 81 (1984) 4685.

[20] J.A. Syage, P.M. Felker and A.H. Zewail, J. Chem. Phys. 81 (1984) 4706.

[21] A. Amirav and J. Jortner, unpublished.

[22] A. Nitzan, J. Jortner and P.M. Rentzepis, Proc. Roy. Soc. A327 (1972) 367.

[23] S. Mukamel and J. Jortner, in: Molecular energy transfer, eds. R.D. Levine and J. Jortner (Wiley, New York, 1975) p. 178.

[24] G.W. Robinson and C.A. Langhof, Chem. Phys. 5 (1974) 1.

[25] F.M. Behlen and S.A. Rice, J. Chem. Phys. 75 (1981) 5672, 5685.

[26] A. Amirav, U. Even and J. Jortner, J. Chem. Phys. 74 (1981) 3745.

[27] A. Amirav and J. Jortner, Chem. Phys. Letters 94 (1983) 545.

[28] A. Amirav, M. Sonnenschein and J. Jortner, Chem. Phys. Letters 100 (1983) 488.

[29] M. Sonnenschein, A. Amirav and J. Jortner, J. Phys. Chem. 88 (1984) 4214.

[30] A. Amirav, M. Sonnenschein and J. Jortner, unpublished.

[31] J.B. Birks and D.J. Dyson, Proc. Roy. Soc. A275 (1963) 135.

[32] B.M. Pierce and R.R. Birge, J. Phys. Chem. 86 (1982) 2651.

[33] J. Troe, Quantitative Analysis of Photoisomerization Rates in Trans-Stilbene and 4-Methyl-Trans-Stilbene, Chem. Phys. Letters, to be published.

7.Q   <u>Analogies between Large van der Waals Molecules and Microsurfaces</u>.
The binding of rare-gas (R) atoms to large aromatic molecules (M)
on the one hand, and to the basal plane of graphite on the other
hand, represent two extremes of the interaction of R atoms with
ordered arrays of sp^2 hybridized carbon atoms. We have explored
the analogies between the characteristics of large van der Waals
$M \cdot R_n$ complexes and R atoms on graphite surfaces, focusing on
structure, packing, orientational registry effects and the nuclear
motion of R adsorbates on finite microsurfaces. The elucidation
of the structure, energetics and nuclear dynamics of large $M \cdot R_n$
complexes rests on semi-empirical calculations of potential
surfaces. These provide a quantitative account of the geometry,
the existence of isomers, the dissociation energies and the fre-
quencies of out-of-plane and in-plane vibrational modes for large
amplitude intermolecular nuclear motion.

7.R   <u>Electron Localization in Clusters</u>. Small clusters exhibit unique
physical and chemical phenomena, which are both of fundamental and
technological significance, and provide ways and means to explore
the "transition" from molecular to condensed-matter systems. We
have provided a theoretical study of the structure, energetics and
dynamics of an excess electron interacting with an alkali-halide
cluster, which was explored by the quantum path integral molecular
dynamics method. These studies establish various compositional,
structural and size dependence of bulk and surface localization
mechanisms of the dynamic process induced by electron attachment.

7.S   <u>Vibrational Predissociation Induced by Exciton Trapping in Rare-Gas</u>
<u>Clusters</u>. The dynamics of exciton trapping, vibrational energy
transfer and vibrational predissociation in an electronically excited
state of Ar_{13} clusters was explored by classical molecular dynamics.
This study constitutes an application of this technique for the
dynamics of electronically excited states of large systems. New
mechanisms of ultrafast ($\sim$ 300 fsec) vibrational energy flow induced
by short-range repulsion were documented. In these systems vibra-
tional energy redistribution does not occur and mode selection
excitation prevails. In small (n=13) clusters the consequences of
vibrational energy flow results in reactive vibrational predissocia-
tion, leading to the "evaporation" of Ar atoms for the cluster. In
layer (n=55) clusters a transition from molecular-type reactive
behavior to nonreactive vibrational relaxation, which is character-
istic of condensed phases, was exhibited.

7.T **Nonreactive and Reactive Excited-State Dynamics in Mixed Rare-Gas Clusters.** We explored the dynamic implications of energy exchange in electronically-vibrationally excited states of mixed rare-gas clusters. The classical molecular dynamics method was applied for the study of vibrational energy flow from electronically excited atomic $(^3P_1)$ states in $Xe^* Ar_{12}$ and $Xe^* Ar_{54}$, due to short-range repulsive interactions, and the consequences of $Xe_2^* (^3\Sigma_u)$ excimer formation in $Xe_2^* Ar_{11}$ and $Xe_2^* Ar_{53}$ clusters. We have established the occurrence of an ultrafast vibrational energy flow (~ 300 fsec) from local Rydberg atomic and excimer excitations into the cluster, which is accompanied by large configurational dilation around the excited state, due to short-range repulsive interactions. Size effects on cluster dynamics were elucidated, being manifested by vibrational predissociation in small clusters, and by vibrational relaxation and vibrational predissociation in small clusters and by vibrational relaxation and vibrational energy redistribution in large clusters. A gradual transition from reactive molecular-type relaxation in small clusters to non-reactive condensed-matter-type relaxation in large clusters was documented. Qualitative and quantitative differences between relaxation of excited species initially located in the interior or on the surface of the cluster were established, being exhibited in the details of the vibrational energy flow. In the case of the bulk $Xe_2^* Ar_{53}$, excessive local heating is manifested in cluster melting, which results in mass transport of the excimer to the cluster surface. The many facets of the dynamics of electronically excited mixed rare-gas clusters are amenable to experimental interrogation.

7.U **Energetics, Dynamics and Ionization of Large Clusters.** Large insulating clusters formed by the nucleation of R atoms on M molecules were synthesized using small-aperture conical nozzles. We have applied the two-color, two-photon ionization method in cluster beams to investigate various spectroscopic and chemical attributes, i.e., the excited-state energetics, the ionization existence of isomer potentials and the vibrational frequencies of large $M \cdot R_n$ (n=1-50) with M $\equiv$ tetracene, anthracene and di-chloroanthracene and R $\equiv$ Ar and Kr clusters. These studies pertain to the evolution of energetic size effects from an isolated large molecule to the condensed phase. Furthermore, the size dependent line broadening and vibrational energetics pertain to the interesting issues of the documentation of isomerization and "melting" in large finite systems. These studies will contribute towards bridging the gap between molecular, surface and condensed-matter energetics and dynamics.

8. PUBLICATIONS

The following manuscripts, which were supported by this research grant, were prepared and submitted for publication.

(1) A. Amirav and J. Jortner
     Vacuum Ultraviolet Absorption Spectroscopy in Supersonic
      Expansions
     J. Chem. Phys. (Communication) 82, 4378 (1985)

(2) J. Troe, A. Amirav and J. Jortner
     Energy-Resolved and Thermalized Photoisomerization Rates
      of Diphenylbutadiene
     Chem. Phys. Letters 115, 245 (1985)

(3) A. Amirav and J. Jortner
     Rotational and Vibrational State Dependence on Intra-
      molecular Coupling and Dynamics in the S_1 State of
      Pyrazine
     J. Chem. Phys. 84, 1500 (1986)

(4) A. Amirav, M. Sonnenschein and J. Jortner
     Interstate coupling and Dynamics of Excited Singlet States
      of Isolated Diphenylbutadiene
     Chem. Phys. 102, 305 (1986)

(5) U. Even, Z. Berkovitch-Yellin and J. Jortner
     Electronic Excitations of the Free-Base Porphine-Ar van
      der Waals Complex
     Canad. J. Chem. (C. Sandorfy-Special Issue) 63, 2073 (1985)

(6) D. Bahatt, U. Even and J. Jortner
     Coupling between Intramolecular and Intermolecular Nuclear
      Motion in a Large van der Waals Complex
     Chem. Phys. Letters 117, 527 (1985)

8. <u>PUBLICATIONS</u> (cont'd)

(7) Klaus Rademann, Uzi Even, Shlomo Rozen and J. Jortner
Photoisomerization Dynamics of Alkyl Substituted Stilbenes
in Supersonic Jets.
Chem. Phys. Lett. <u>125</u>, 5-11 (1986)

(8) A. Amirav, J. Jortner, S. Okajima and E. C. Lim
Manifestations of Intramolecular Vibrational Energy
Redistribution on Electronic Relaxation in Large Molecules
Chem. Phys. Letters <u>126</u>, 2187 (1986)

(9) U. Landman, D. Scharf and J. Jortner
Electron Localization in Alkali-Halide Clusters
Phys. Rev. Letters <u>54</u>, 1860 (1985)

(10) Dafna Scharf, Uzi Landman and Joshua Jortner
Energetics and Dynamics of Clusters
Proc. of the Int'l School of Physics "Enrico Fermi", Italy,
1986, in: <u>Advances in Chemical Reaction Dynamics</u> (D. Reidel
Publishing Company)

(11) D. Scharf, U. Landman and J. Jortner
Vibrational Predissociation Induced by Exciton Trapping in
Inert-Gas Clusters
Chem. Phys. Letters <u>126</u>, 495-500 (1986)

(12) Dafna Scharf, Uzi Landman and J. Jortner
Surface States of Electrons and Alkali-Halide Clusters
Proc. of the 19th Jerusalem Symposium, Israel, 1986. Eds
J. Jortner and B. Pullman (D. Reidel Publishing Company,
Holland, 1986)

(13) Samuel Leutwyler and Joshua Jortner
The Adsorption of Rare-Gas on Microsurfaces of Large
 Aromatic Molecules
J. Phys. Chem. 91, 5558 (1987)

(14) Dafna Scharf, Uzi Landman and Joshua Jortner
Atomic and Molecular Quantum Mechanics by the Path
 Integral Molecular Dynamics Method
Chem. Phys. Letters 130, 504 (1987)

(15) A. Amirav and Joshua Jortner
Rotation, Vibration and Electronic Relaxation
Proc. of the CECAM Conference, Orsay, France, 1986
 (D. Reidel Publishing Co., Holland, 1986)

(16) A. Amirav and J. Jortner
Resonances in Mediated Intersystem crossing of Jet-
 Cooled Anthracene Derivatives
Chem. Phys. Letters 132, 335 (1986)

(17) A. Amirav, J. Jortner, M. Terazima and E.C. Lim
Rotational Effects on Intramolecular Radiationless
 Transitions in a Large Molecule
Chem. Phys. Letters 133, 179 (1987)

(18) U. Landman, R.N. Barnett, C.L. Cleveland, D. Scharf
 and J. Jortner
Electron Excitation Dynamics, Localization and Solvation
 in Small Clusters
J. Phys. Chem. 91, 4980 (1987)

(19) A. Amirav, C. Horowitz and J. Jortner
Optical Selection Studies of Electronic Relaxation from
 the S_1 State of Jet-Cooled Anthracene Derivatives
J. Chem. Phys. 88, 3092 (1988)

(20) R.D. Levine, S.A. Rice and J. Jortner
      Level Structure and Dynamics from Diatomics to Clusters
      Advances in Chemical Physics
      (John Wiley & Sons. New York, 1988)

(21) U. Even, N. Ben-Horin and J. Jortner
      Hierarchal Isomerization of Molecular Clusters
      Chem. Phys. Letters (Submitted)

6.

COUPLING BETWEEN INTRAMOLECULAR AND INTERMOLECULAR NUCLEAR MOTION IN A LARGE VAN DER WAALS COMPLEX

Dar BAHATT, Uzi EVEN and Joshua JORTNER

Department of Chemistry, Tel-Aviv University, 69978 Tel Aviv, Israel

The vibrational level structure of the $S_0 \rightarrow S_1$ transition of trans-stilbene·Ar_1 was interrogated by mass-resolved resonance two-photon ionization spectroscopy in supersonic beams. Combination bands provide evidence for intermode coupling between the vibrational excitation of the relative motion of Ar and trans-stilbene (TS) in TS·Ar and an intramolecular vibration of TS, which is manifested by the linear dependence of the intermolecular vibrational energy on the vibrational quantum number of the intramolecular motion.

Electronic–vibrational spectra of large van der Waals (vdW) complexes [1,2], consisting of aromatic molecules bound to atomic or molecular ligands, reveal two major types of vibrational modes: (A) Intramolecular vibrational modes of the aromatic molecule in the complex [1–7], and (B) intermolecular vibrational modes, which involve the motion of the ligand relative to the large molecule [1,2,7,8]. The intermolecular modes can be segregated further into: (B1) perpendicular intermolecular modes involving out-of-plane motion of the ligand relative to the organic molecule [2,7–11]. Typical vibrational frequencies for rare-gas aromatic-molecule complexes were documented experimentally to lie in the range $\bar{\omega} \approx 30$–$50\ cm^{-1}$ [1,2,7–10]. (B2) Parallel intermolecular modes involving in-plane motion of the ligand with respect to the organic molecule [8]. Vibrational frequencies of these modes were calculated to lie in the range $\bar{\omega} \approx 1$–$10\ cm^{-1}$ [9]. These intermolecular modes are of considerable interest in providing an analog for surface vibrational motion in a finite system and in constituting the precursors of phonon modes in condensed phases. A reasonable starting point for the understanding of the nuclear motion within large vdW complexes is based on the segregation between intramolecular and intermolecular vibrational modes [7,8]. A heuristic justification for such an approach rests on the separation of time scales

for the two distinct types of motion, which are characterized by a small frequency ratio $\omega(intermolecular)/\omega(intramolecular) \approx 0.001$–$0.05$. Nevertheless, the coupling between intermolecular and intramolecular motion in large vdW complexes is pertinent for the elucidation of the energetics, i.e. the vibrational level structure, and the dynamics, e.g., vibrational energy redistribution, in these systems. In this note, we report on the observation of the manifestations of the coupling between intramolecular and intermolecular nuclear motion in a large vdW complex. We have explored the electronic–vibrational spectroscopy of the $S_0 \rightarrow S_1$ transition of the trans-stilbene (TS)–Ar complex interrogated by mass-resolved resonance two-photon ionization (R2PI) [7,11–13]. The vibrational level structure of TS·Ar_1 in its S_1 state exhibits intramolecular vibrations of TS and perpendicular intermolecular Ar–TS modes. The combination bands, which involve both types of vibration, reveal systematic deviations from additivity, exhibiting the manifestations of the coupling between intermolecular and intramolecular motion in the large vdW complex.

The TS·Ar^+ vdW ions were produced by R2PI of the corresponding vdW molecules in supersonic beams and interrogated by time-of-flight mass spectrometry. TS was heated in the nozzle chamber to 150°C (partial vapour pressure 7 Torr) [14], seeded into Ar (stagna-

tion pressure $p = 1-2$ atm) and expanded by a mag-
netic pulsed valve (gas pulse length of 200 μs, pulse
frequency 10 Hz) through a conical nozzle (nozzle
diameter $D = 0.3$ mm, nozzle opening angle $\theta = 30°$).
The use of conical nozzles considerably enhances clus-
tering in the supersonic expansion [15]. The central
core of the jet was skimmed by a nickel electroplated
copper skimmer (diameter 1 mm). Light from a fre-
quency-doubled N_2 laser pumped dye laser (spectral
range 2800–3200 Å, pulse duration 4 ns, peak power
output 2 μJ/pulse, spectral width 0.3 cm^{-1}) was
focused by an $f = 7$ cm lens onto the molecular beam
at the ion source of the time-of-flight mass spectrom-
eter (TOFMS). The total ion accelerating voltages em-
ployed in these experiments were 800 V. The acceler-
ated ions were passed through the drift tube (length
249 mm) and interrogated by a fast ion detection
scheme. This consists of a large-aperture high-voltage
(30 kV) detector generating free electrons, which are
detected by a plastic scintillator (light pulse width
2–5 ns in the range 4100–4300 Å) in conjunction
with a photomultiplier (Phillips XP2020). The photo-
multiplier signal was fed to a boxcar integrator
(Brookdeal), which recorded the appropriate mass
(TS$^+$; $m/e = 180$ or TS·Ar$^+$; $m/e = 220$). The R2PI
ion signal was averaged by a signal averager (PAR) and

diplayed after normalization to the square of the in-
cident laser intensity.

The mass-resolved R2PI spectrum for the low-energy
regime (excess vibrational energy $E_V = 0$–500 cm^{-1})
of the $S_0 \to S_1$ transition of TS is portrayed in fig. 1.
The electronic origin of $S_0 \to S_1$ is located at 3102.8
Å (32229 cm^{-1}), which is in accord with the original
fluorescence excitation spectra [16]. The bare-mole-
cule spectrum exhibits weak hot bands at 25 and 38
cm^{-1} and low-frequency vibrations at 80 and 89
cm^{-1}, which is in good agreement with the previous
laser-induced fluorescence (LIF) spectra [16]. The
80 and 89 cm^{-1} modes correspond, according to
Warshel [17], to out-of-plane C–ϕ bending and
C–C–ϕ bending, respectively. The prominent vibra-
tional mode in the S_1 state of TS involves the well
known [16] $\omega_0 = 200$ cm^{-1} progression, which cor-
responds to the C–C–ϕ in-plane bending [17].

The mass-resolved R2PI spectrum of TS·Ar (fig. 2)
reveals the electronic origin of the $S_0 \to S_1$ transition
at 3108.4 Å (32171 cm^{-1}). The red dispersive spec-
tral shift $\Delta\nu = -58 \pm 5$ cm^{-1} of the $S_0 \to S_1$ electron-
ic origin of TS induced by the binding of an Ar atom
is similar to those observed for the origin of intense
spin-allowed transitions in other aromatic molecules,
e.g., analine [2], fluorene [3], anthracene [18] and
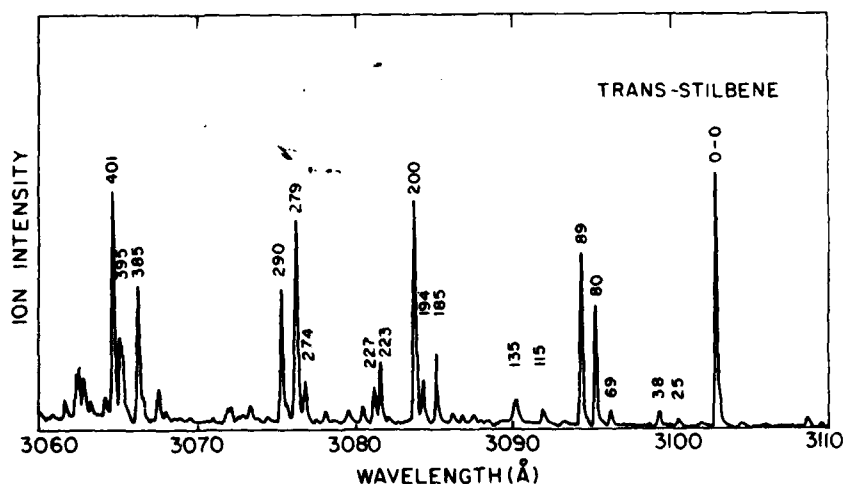

Fig. 1. Ion current versus wavelength in the range 3060–3110 A for trans-stilbene$^+$. Trans-stilbene at 150°C was seeded into Ar at
$p = 2$ atm and expanded through a pulsed conical nozzle ($D = 0.3$ mm, $\theta = 30°$). The electronic origin is marked 0–0 and the num-
bers labeling the spectral features mark the excess vibrational energies above the origin (in cm^{-1}).
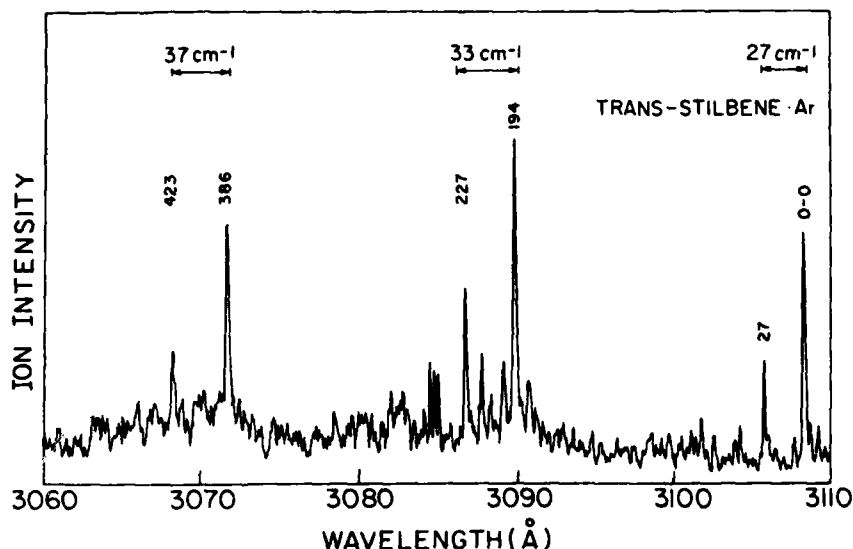
Fig. 2. Ion current versus wavelength in the range 3060–3110 A for trans-stilbene·Ar*. Experimental conditions and labeling of spectral features as in fig. 1.

tetracene [1]. The vibrational level structure of TS·Ar reveals two types of vibrations:

(A) Intramolecular vibrations. An intense progression with the frequency $\bar{\omega}_0 = 194$ cm^{-1} is exhibited (fig. 2), which is attributed to the intramolecular symmetric C–C–ϕ in-plane bending of TS in the TS·Ar complex.

(B) Intermolecular vibrations. The spectral feature at $E_V = 27$ cm^{-1} in TS·Ar (fig. 2) is absent in the bare TS molecule. The intensity of this spectral feature relative to the electronic origin of TS·Ar is independent of the Ar stagnation pressure, whereupon it does not correspond to a hot band of TS in the complex. The spectral feature is attributed to an intermolecular vibrational frequency of $\bar{\omega}_1 = 27$ cm^{-1}. Model calculations [2,10] for the benzene·Ar vdW complex reveal that the frequency of the perpendicular vibrational motion of Ar relative to the benzene ring is ≈ 30 cm^{-1}. Accordingly, we attribute the $\bar{\omega}_1 = 27$ cm^{-1} mode in TS·Ar to the out-of-plane perpendicular motion of the Ar atom with respect to the benzene ring of TS.

(C) Combination bands. The vibrational excitations at 227 and 423 cm^{-1} (fig. 2) are assigned to combination $(v\bar{\omega}_0 + \bar{\omega}_1)$ bands of $\bar{\omega}_0$ and $\bar{\omega}_1$ modes, which correspond to $\bar{\omega}_0 + 33$ cm^{-1} (± 1 cm^{-1}) and to $2\bar{\omega}_0 + 37$ cm^{-1} (± 1 cm^{-1}), respectively.

The most interesting feature of the vibrational level structure of TS·Ar in the S_1 state is the appearance of the (perpendicular) intermolecular vibration, which exhibits a systematic dependence on the intramolecular vibrational excitation $(v\bar{\omega}_0)$, being $\bar{\omega}_1 = 27$ cm^{-1} for $v = 0$, $\bar{\omega}_1 = 33$ cm^{-1} for $v = 1$, and $\bar{\omega}_1 = 37$ cm^{-1} for $v = 2$. We attribute this nearly linear dependence of $\bar{\omega}_1$ for v to the effects of intermode coupling in a vdW complex. This experimental result is in accord with the recent theoretical calculations of Sage and Jortner [19], who considered the coupling between intermolecular and intramolecular vibrations in a large vdW complex. This treatment rests on the consideration of the coupled equations resulting from the expansion of the total vibrational wavefunction in terms of the "free"-molecule wavefunctions. Application of van Vleck's perturbation theory results in explicit first-order and second-order kinetic energy and potential energy corrections, which incorporate the energetic shift of the intramolecular vibration, as well as the intermolecular vibrational energies, which depend on the vibrational quantum numbers of the intramolecular modes. Consideration of intermode coupling in a simple model system consisting of a single harmonic intramolecular mode coupled to an intermolecular mode results in the energy levels [19].

529

$$E_{v,l} = v\hbar\bar{\omega}_0 + l\hbar\bar{\omega}_1 (1 + v\delta), \qquad (1)$$

where v and l are the vibrational quantum numbers for the intramolecular and intermolecular modes, respectively. $\bar{\omega}_0$ is the intramolecular vibrational frequency in the complex, which is related to the "free" molecule vibrational energy ω_0 via $\bar{\omega}_0 = \omega_0 (1 + a)$, where the "solvent shift" a originates from kinetic energy and potential energy contributions, which are due to the modification of the intramolecular force field by vdW binding. $\bar{\omega}_1$ is the vibrational frequency of the intermolecular motion for $v = 0$, while $\delta = (\gamma\hbar\omega_0/8k_0\bar{\omega}_1)$, with γ being the potential energy contribution for the intermode coupling and k_0 the force constant for the intramolecular vibration. From eq. (1) it is apparent that the spectral shift of the intramolecular vibrational frequency relative to that of the "free" molecule is constant, while the energy shift of the combination band vl, involving the intermolecular mode relative to $v0$, is linear in v. From the application of eq. (1) for the analysis of our experimental data (fig. 2), we conclude that:

(1) The intramolecular symmetric C–C–ϕ in-plane bending vibration is reduced from $\omega_0 = 200$ cm^{-1} in the "free" molecule to $\bar{\omega}_0 = 194$ cm^{-1} in the complex. Accordingly, the contribution of the kinetic and potential energy terms is $a = -3.1 \times 10^{-2}$. The spectral shift $(\bar{\omega}_0 - \omega_0)$ is independent of v, as is expected.

(2) The linear dependence of the experimental intermolecular frequency on v is in accord with the relation $\bar{\bar{\omega}}_1 = \bar{\omega}_1(1 + v\delta)$, eq. (1). The intermode coupling term is $\delta \approx 0.2$. This large value of δ originates from the low value of ω_0 (or rather k_0) and presumably also from the effective intermode coupling for that particular intramolecular mode.

A cursory examination of the R2PI spectra of TS and TS·Ar reveals that the 80 and 89 cm^{-1} vibrational frequencies of TS (fig. 1) are missing in the TS·Ar spectrum (fig. 2). This behaviour is in sharp contrast with the prominence of the $\bar{\omega}_0$ mode (fig. 2). The "disappearance" of the S_1 80 and 89 cm^{-1} vibrational excitations in the R2PI spectrum can be blamed on one of the following reactive processes: (i) Vibrational predissociation (VP) of TS·Ar in the S_1 intermediate state. (ii) VP of the vibrational excited positive vdW TS·Ar$^+$ ion. Mechanism (i) is inapplicable for the problem at hand as the vibrational excitations (80–90 cm^{-1}) in the S_1 state are considerably lower than

the dissociation energy of the TS·Ar vdW complex, which is estimated [2,10] to be $D \approx 400$ cm^{-1}, whereupon the VP channel is closed in the intermediate S_1 state. On the other hand, the VP channel is open in the final ionic state. The adiabatic ionization potential of TS is 7.75 eV [20], whereupon the excess vibrational energy of TS·Ar$^+$ produced via R2PI by two 3095 Å photons is 2250 cm^{-1}, being sufficient for dissociation. The "disappearance" of the 80 and 89 cm^{-1} modes (which will hereinafter be referred to as the α modes) together with persistence of the higher energy $\bar{\omega}_0 = 194$ cm^{-1} mode in the R2PI spectrum, raises the distinct possibility of mode selective VP of the TS·Ar$^+$ ion, which was excited photoselectively to an α vibrational state from an $S_1(\alpha)$ intermediate level. Further work is being conducted for a critical scrutiny of this conjecture.

References

[1] A. Amirav, U. Even and J. Jortner, J. Chem. Phys. 75 (1981) 2489.

[2] U. Even, A. Amirav, S. Leutwyler, M.J. Ondrechen, Z. Berkovitch-Yellin and J. Jortner, Faraday Discussions Chem. Soc. 73 (1982) 153.

[3] A. Amirav, U. Even and J. Jortner, Chem. Phys. 67 (1982) 1.

[4] A. Amirav, U. Even and J. Jortner, J. Phys. Chem. 85 (1981) 309.

[5] A. Amirav, U. Even and J. Jortner, J. Chem. Phys. 74 (1981) 3475.

[6] U. Even and J. Jortner, J. Chem. Phys. 78 (1983) 3445.

[7] S. Leutwyler, U. Even and J. Jortner, J. Chem. Phys. 79 (1983) 5769.

[8] U. Even and J. Jortner, Faraday Discussions Chem. Soc. 73 (1982) 175.

[9] S. Leutwyler, A. Schmelzer and N. Meyer, J. Chem. Phys. 79 (1983) 5769.

[10] M.J. Ondrechen, Z. Berkovitch-Yellin and J. Jortner, J. Am. Chem. Soc. 103 (1981) 6586.

[11] J.B. Hopkins, D.E. Powers and R.E. Smalley, J. Phys. Chem. 85 (1981) 3739.

[12] F.H. Fung, W.E. Henke, T.R. Hays, H.L. Selzle and E.W. Schlag, J. Phys. Chem. 85 (1981) 3560.

[13] S. Leutwyler, U. Even and J. Jortner, Chem. Phys. Letters 86 (1982) 439.

[14] R.C. Weast, ed., Handbook of chemistry and physics (CRC Press, Cleveland, 1976).

530

[15] D. Bahatt, U. Even and J. Jortner, to be published.
[16] J. Synge, W. Lambert, P. Felker, A.H. Zewail and R.M. Hochstrasser, Chem. Phys. Letters 88 (1982) 266;
A. Amirav and J. Jortner, Chem. Phys. Letters 95 (1983) 295;
T.S. Zwier, E. Carrasquillo and D.H. Levy, J. Chem. Phys. 78 (1983) 5493;

T.J. Majors, U. Even and J. Jortner, J. Chem. Phys. 81 (1984) 2330.
[17] A. Warshel, J. Chem. Phys. 62 (1975) 214.
[18] A. Amirav, M. Sonnenschein and J. Jortner, Chem. Phys. 88 (1984) 199.
[19] M. Sage and J. Jortner, to be published.
[20] W.C. Herndon, J. Am. Chem. Soc. 98 (1976) 887.

Electron Localization in Alkali-Halide Clusters

Uzi Landman

*School of Physics, Georgia Institute of Technology, Atlanta, Georgia 30332, and Institute of Theoretical Physics,
Chalmers University of Technology, 412 96 Goteborg, Sweden*

and

Dafna Scharf and Joshua Jortner

Department of Chemistry, Tel Aviv University, 69978 Tel Aviv, Israel
(Received 14 January 1985)

The quantum path-integral molecular-dynamics method was applied to explore the structure, energetics, and dynamics of an excess electron interacting with an alkali-halide cluster. Four distinct modes of electron localization were established, which depend on the cluster composition, size, and structure; they involve an internal *F*-center defect, an external surface state, dissociative detachment of an alkali atom, and structural isomerization induced by electron attachment.

Structural, electronic, dynamic, and chemical characteristics of materials depend primarily on the state (phase) and the degree (size) of aggregation. Small clusters, i.e., finite aggregates containing 3–500 particles, exhibit unique physical and chemical phenomena, which are of both fundamental and technological significance, and provide ways and means to explore the "transition" from molecular to condensed-matter systems.[1] Theoretical studies of clusters were hampered by the relatively large number of particles, which renders the adaptation of molecular science techniques rather cumbersome, while the lack of translational symmetry inhibits the employment of solid-state methodology. Molecular-dynamics (MD) simulations, consisting of the generation of phase-space trajectories via the numerical integration of the (classical) equations of motion for a many-particle system, are particularly suitable for the study of the structure and dynamics of small clusters.[2,3] In this context, localized excess electron states in clusters[4] are of considerable interest with regard to the (nonreactive and reactive) mechanisms of electron attachment, the formation of bulk or surface states, and the role of the excess electron as a probe for the interrogation of the nuclear dynamics of the cluster. Futhermore, quantum phenomena are expected to be pronounced in such systems since the electron wavelength is comparable to the cluster size. In this paper we report on the structure, energetics, and dynamics of alkali-halide clusters (AHC) studied with classical MD, and of electron alkali clusters studied with the quantum path-integral MD method (QUPID).[5–8] AHC were chosen

since the nature of the interionic interactions is well understood and in view of the abundance of model calculations and experimental information of these systems.[9] Our QUPID calculations establish four modes of localization of an excess electron in AHC: (i) an *F*-center defect with the excess electron replacing an internal halide ion; (ii) a new surface state, i.e., a "surface *F* center" of the excess electron; (iii) dissociative electron attachment to AHC resulting in the formation of an "isolated" alkali atom; (iv) structural isomerization induced by electron attachment. Our calculations establish the compositional, structural, and size dependence of these various localization mechanisms.

The QUPID method[6–8] was applied to a system of an electron interacting with an AHC consisting of N ions (N_1 cations and N_2 anions). The interionic potential energy within the AHC is $V_{AHC} = \sum_{IJ} \Phi_{IJ}(R_{IJ})$, with the interionic pair potentials $\Phi_{IJ}(R_{IJ})$ being given by the Born-Mayer potential with the parameters determined by Fumi and Tosi.[10] The electron-AHC potential is $V_e(r) = \sum_I \Phi_{eI}(r - R_I)$ consisting of a sum of electron-ion potentials, which are described by the purely repulsive pseudopotential $\Phi_{eI}(r) = e^2/r$ for the electron-anion interaction and by the local pseudopotential[11] $\Phi_{eI}(r) = -e^2/R_c$, $r \leq R_c$, and $\Phi_{eI}(r) = -e^2/r$, $r > R_c$, for the electron–positive-ion interaction. The Hamiltonian is $H = K_e + V_e + K_{AHC} + V_{AHC}$, where K_e and K_{AHC} are the kinetic-energy operators for the electron (mass m) and of the ions (masses $M_I = M_1$ and M_2), respectively. Observables are obtained from the quantum partition function $Z = \lim_{p \to \infty} (Z_p)^p$ with

$$Z_p = \text{Tr}[\exp(-\tau K_{AHC})\exp(-\tau K_e)\exp(-\tau V_{AHC})\exp(-\tau V_e)],$$

where $\tau = \beta/p$ and $\beta = (k_B T)^{-1}$ is the inverse temperature. If we make use of the free particle propagator[12] Z_p is

$$Z_p = \prod_{a=1,2} \left(\frac{M_a}{2\pi\tau\hbar^2}\right)^{3N_a p/2} \left(\frac{m}{2\pi\tau\hbar^2}\right)^{3p/2} \int \prod_{I=1}^{N} d^3 R_I \prod_{I=1}^{p} d^3 r_I \exp[-\beta(V_{eff}^e + V_{eff}^I)], \tag{1}$$

where

$$V_{eff} = \sum_{i=1}^{p} \left[\frac{pm}{2\hbar^2\beta^2}(r_i - r_{i+1})^2 + V_e(r_i)/p \right]$$

and

$$V_{eff}^I = \sum_{I=1}^{N}\sum_{i=1}^{p} \frac{pM_I}{2\hbar^2\beta^2}(R_{I(i)} - R_{I(i+1)})^2 + V_{AHC}/p.$$

Equation (1) maps the quantum problem onto the classical statistical mechanics of $N+1$ particles, each consisting of a periodic chain (necklace) of p pseudoparticles (beads) with nearest-neighbor harmonic interchain interactions, whose strengths depend upon the masses (m, M_1, M_2), the temperature (T), and the pseudoparticle number (p). When the thermal wavelength [$\lambda_T = (\beta\hbar^2/M_I)^{1/2}$] is smaller than any relevant length scale, the Gaussian factor in Z_p reduces to a delta function and the necklace collapses

to a classical particle. This is the case for the ionic part of our system. The average energy of the system is given at equilibrium by

$$E = \frac{3N}{2\beta} + \langle V_{AHC} \rangle + K_e + p^{-1}\left\langle \sum_{i=1}^{p} V_e(r_i) \right\rangle$$

with the electron kinetic energy

$$K_e = \frac{3}{2\beta} + \frac{1}{2p}\sum_{i=1}^{p}\left\langle \frac{\partial V_e(r_i)}{\partial r_i} \cdot (r_i - r_p) \right\rangle$$

which consists of the free-particle term $(3/2\beta)$ and the contribution from the interaction (K_{int}) with the ions.[13] The statistical averages indicated by angular brackets are over the Boltzmann distributions as defined in Eq. (1). This formalism is converted into a numerical algorithm by noting[14] the equivalence of the sampling described above to that over phase-space trajectories generated via MD by the classical Hamiltonian

$$H = \sum_{i=1}^{p}\frac{m^*\dot{r}_i^2}{2} + \sum_{I=1}^{N}\frac{M_I\dot{R}_I^2}{2} + \sum_{i=1}^{p}\left[\frac{pm(r_i - r_{i+1})^2}{2\hbar^2\beta^2} + \frac{V_e(r_i)}{p} \right] + V_{AHC}. \tag{2}$$

the mass m^* being arbitrary and taken as $m^* = 1$ u.

Numerical simulations were performed for an electron interacting with sodium-chloride clusters at about room temperature. On the basis of examination of the stability of the variance of the kinetic-energy contribution K_{int}, the number of "electron beads" was taken as $p = 399$. By use of an integration step of $\Delta t = 1.03 \times 10^{-15}$ sec, long equilibration runs were performed [$(1-2) \times 10^4 \Delta t$]. The reported results were obtained via averaging over $8 \times 10^3 \Delta t$, following equilibration. The electron-ion pseudopotential parameters were varied by changing the cutoff radius R_c in the range $(3.22-5.29)a_0$. From QUPID calculations on a single Na atom, the atomic ionization potential is reproduced (see Table I) for $R_c = 5.29a_0$, which seems to be a too-high value for the characterization of this pseudopotential.[6] Therefore, on the basis of pseudopotential parametrization studies[11] and a recent QUPID study[8] of F centers in molten and solid KCl in which the same form of pseudopotential was employed, a value of $R_c = 3.22a_0$ (yielding a value of -0.3005 a.u. for the electron binding energy to Na$^+$, see Table I) is preferred. Fortunately, our conclusions regarding internal and surface-localization modes remain unchanged with respect to reasonable variations of this parameter. In simulations involving the electron-AHC interaction, different initial conditions were employed, two of which for the [Na$_{14}$Cl$_{13}$]$^+$ system are portrayed in Figs. 1(a) and 1(b). The resulting final state of the system was found to be independent of the initial conditions.

It has previously been suggested on the basis of zero-temperature structural calculations,[9] and has been confirmed by our classical MD simulations, that when

the size of the clusters increases ($N \geq 20$), the NaCl cyrstallographic arrangement is preferred for particular stability for clusters forming rectangular structures even if the number of positive and negative ions is not equal. Therefore, we have chosen to study first the interaction of an electron with [Na$_{14}$C$_{13}$]$^+$ and [Na$_{14}$Cl$_{12}$]$^{++}$ clusters, which exhibit pronounced stability. In Figs. 1(c) and 1(e), we present our results (using $R_c = 3.22a_0$) for the equilibrium electron-charge distribution obtained from 2D projections of the necklace edge points, and for the nuclear configuration of the clusters. In both cases the electron, which starts in either initial configuration as shown in Figs. 1(a), 1(b), has been localized. However, two distinct modes of electron localizations are exhibited involving *internal* and *external localization* for the doubly charged and singly charged cluster, respectively. The vacancy-containing configuration of the [Na$_{14}$Cl$_{12}$]$^{++}$ cluster stabilizes an internally localized excess electron state, with the e surrounded by six Na$^+$ ions in an octahedral configuration and by twelve Cl$^-$ ions [Fig. 1(e)] which is similar to the case of an F center in the extended solid. The electron affinity of the cluster $E_A = E_b^e + E_c$ is obtained by summing the electron binding energy

$$E_b^e = \frac{3}{2\beta} + K_{int} + p^{-1}\sum_{i=1}^{p}\langle V_e(r_i) \rangle$$

and the cluster reorganization energy $E_c = \langle V_{AHC} \rangle - \langle V_{AHC} \rangle_0$, where $\langle V_{AHC} \rangle_0$ is the potential energy of the "bare" AHC in the absence of the electron. The ionic configuration of the e-[Na$_{14}$Cl$_{12}$]$^{++}$ cluster is somewhat distorted; however, the gain in E_b^e(-0.249

TABLE I. Average equilibrium temperature ($\langle T \rangle$), interionic cluster potential energy ($\langle V_{\text{AHC}} \rangle$), electron interaction kinetic energy (K_{int}), electron kinetic energy $K_e = 3/2\beta + K_{\text{int}}$, e-AHC interaction potential energy ($\langle V_e \rangle$), electron binding energy (E_B^e), cluster reorganization energy (E_c), electron affinity of cluster (E_A), and Cartesian components of the "electron necklace" gyration radii (R_x^2, R_y^2, R_z^2). Atomic units are used (energy and $\langle T \rangle$ in Hartrees, length in Bohr radii). Variances are given in parentheses. Calculated values of $\langle T \rangle$ and $\langle V_{\text{AHC}} \rangle$ for the "bare" clusters: $[\text{Na}_{14}\text{Cl}_{14}]$, $0.976(0.111) \times 10^{-3}$, -3.7296; $[\text{Na}_{14}\text{Cl}_{13}]^+$, $0.948(0.106) \times 10^{-3}$, -3.5911; $[\text{Na}_{14}\text{Cl}_{12}]^{++}$, $0.954(0.093) \times 10^{-3}$, -3.3151; $[\text{Na}_5\text{Cl}_4]^+$, $1.01(0.38) \times 10^{-3}, -1.0999$.

|	$10^3 \langle T \rangle$	$\langle V_{\text{AHC}} \rangle$	$10^2 K_{\text{int}}$	K_e	$\langle V_e \rangle$	E_B^e	E_c	E_A	R_x^2	R_y^2	R_z^2
e-$[\text{Na}_{14}\text{Cl}_{13}]^+$	0.983	-3.4856	6.4195	0.0657	-0.2251	-0.1594	0.1055	-0.0539	5.4	7.0	9.8
$R_c = 3.22$	(0.035)		(0.633)								
e-$[\text{Na}_{14}\text{Cl}_{13}]^+$	0.972	-3.5768	1.5182	0.0166	-0.0700	-0.0534	0.0143	-0.0391	23.5	23.2	55.2
$R_c = 5.29$	(0.031)		(0.426)								
e-$[\text{Na}_{14}\text{Cl}_{12}]^{++}$	0.938	-3.2372	7.2203	0.0736	-0.3226	-0.2490	0.0799	-0.1691	4.6	6.8	6.3
$R_c = 3.22$	(0.028)		(0.767)								
e-$[\text{Na}_{14}\text{Cl}_{12}]^{++}$	0.948	-3.3143	1.9995	0.0214	-0.1365	-0.1151	0.0008	-0.1143	55.3	57.9	43.3
$R_c = 5.29$	(0.025)		(0.956)								
e-$[\text{Na}_5\text{Cl}_4]^+$	0.950	-1.0059	2.6389	0.0278	-0.3012	-0.2734	0.0940	-0.1794	2.2	2.0	2.5
$R_c = 3.22$	(0.132)		(0.582)								
e-$[\text{Na}_5\text{Cl}_4]^+$	0.946	-1.0483	3.5453	0.0369	-0.1876	-0.1508	0.0516	-0.0992	5.7	7.2	5.5
$R_c = 4.36$	(0.038)		(0.601)								
e-Na^+	1.038		0.713	0.0087	-0.3092	-0.3005			$R^2 = 3.6$		
$R_c = 3.22$	(0.442)		(0.638)								
e-Na^+	1.043		0.034	0.00198	-0.2299	-0.2280			$R^2 = 3.4$		
$R_c = 4.36$	(0.527)		(0.049)								
e-Na^+	1.084		0.012	0.0017	-0.18897	-0.1872			$R^2 = 4.9$		
$R_c = 5.29$	(0.574)		(0.032)								
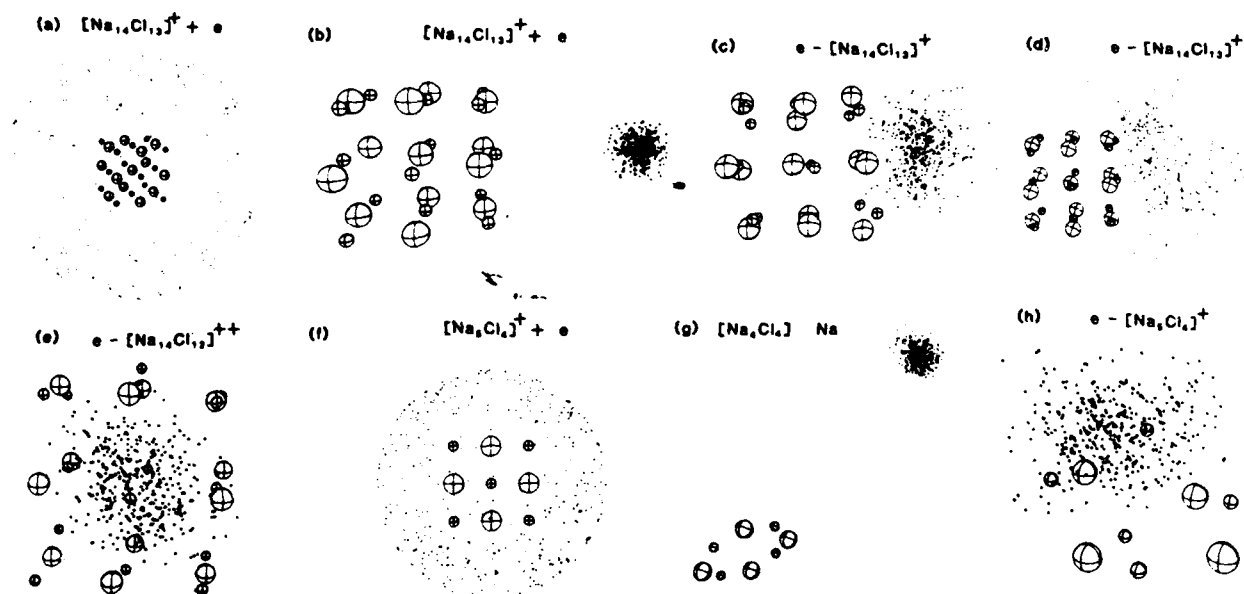
FIG. 1. Ionic configurations and "electron necklace" distributions for an excess electron interacting with sodium-chloride clusters. Small and large spheres correspond to Na^+ and Cl^- ions, respectively. Dots represent 2D projections of the "electron beads." (a),(b) Alternate initial configurations of $[\text{Na}_{14}\text{Cl}_{13}]^+ + e$ [in (b) the e bead is localized to the right of the cluster] which achieve the equilibrium configurations corresponding to surface states given in (c), $R_c = 3.22a_0$, and (d) $R_c = 5.29a_0$. (e) Equilibrium configuration of e-$[\text{Na}_{14}\text{Cl}_{12}]^{++}$, $R_c = 3.22a_0$, exhibiting an internal F center. (f) Initial state of e-$[\text{Na}_5\text{Cl}_4]^+$. (g) Equilibrium configuration of e-$[\text{Na}_5\text{Cl}_4]^+$ with $R_c = 3.22a_0$ resulting in dissociation of Na. (h) Equilibrium configuration of e-$[\text{Na}_5\text{Cl}_4]^+$ with $R_c = 4.36a_0$ which corresponds to structural isomerization.

a.u.) exceeds the loss in E_c (0.0799 a.u.) favoring internal localization (Table I). It is of interest to note that the total energy of e-$[Na_{14}Cl_{12}]^{++}$ is rather close to that of $[Na_{14}Cl_{13}]^+$, so that the electron binding energy in the cluster is similar to that of a negative ion, analogously to the situation for F-center formation in (extended) ionic crystals,[8] thus establishing the dominance of short-range attractive interactions in electron trapping (localization) phenomena. A drastically different localization mode is obtained in the e-$[Na_{14}Cl_{13}]^+$ system [Fig. 1(c)], where a surface state is exhibited. For $R_c = 3.22a_0$ the electron localizes around an Na^+ surface ion [Fig. 1(c)], leaving an essentially neutral $[Na_{13}Cl_{13}]$ cluster, which interacts with the (partially) neutralized Na atom mainly via polarization of the electron cloud (with a residual ionic binding of −0.002 a.u.). We refer to this state as a cluster-surface localized state, which bears close analogy with Tamm's crystal-surface states.[15] When the pseudopotential cutoff R_c increases, the surface state becomes more extended [see Fig. 1(d) for $R_c = 5.29a_0$] [the choice of an abnormally high value for R_c (i.e., $5.29a_0$) prevents internal localization in the $[Na_{14}Cl_{12}]^{++}$ cluster since the internal region is then predominantly repulsive (see Table I), resulting in a surface state]. A measure of the spatial extent of the localized electron is given by the gyration radius of the "electron necklace" $R^2 = (1/2p^2)\langle \sum_{i,j}(r_i - r_j)^2 \rangle$, which demonstrates (Table I) the enhanced localization in the e-$[Na_{14}Cl_{12}]^{++}$ system and the anisotropy of the electron distribution in the e-$[Na_{14}Cl_{13}]^+$ system. An estimation of the extent of the electron thermal wave packet is obtained also by

$$R_T = \left[\frac{p}{p-1} \sum_{i=1}^{p} \langle (r_i - r_{i+1})^2 \rangle \right]^{1/2}$$

which for a free electron at room temperature yields $R_T = \sqrt{3}\lambda_T \simeq 56a_0$ ($\lambda_T \simeq 32.34a_0$). In all the calculations reported herein R_T values of $52a_0$–$55a_0$ were obtained, i.e., the same as the free-electron value to within statistical significance (compare to typical interionic distance of $5a_0$ in NaCl clusters).

In smaller clusters novel effects of dissociative electron attachment and cluster isomerization induced by electron localization will be manifested. We have studied the smallest singly ionized cluster exhibiting high stability, i.e., $[Na_5Cl_4]^+$, for which the lowest energy configuration is planar with four Na^+ ions at the corners and one at the center of an approximate square.[9] This cluster possesses an isomeric structure (less stable by 0.014 a.u.) in which the ions are arranged in a distorted pyramidal configuration.[9] Adding

an electron to the ground-state planar configuration of $[Na_5Cl_4]^+$ (with the Na^+ pseudopotential being characterized by $R_c = 3.22a_0$) transforms the system into a neutral $[Na_4Cl_4]$ cluster with a planar ring structure and a dissociated neutral Na atom [Table I and Figs. 1(f) and 1(g), corresponding to the initial- and final-state configurations, respectively]. To demonstrate that this process is driven by the localization of e around a single Na^+ ion, we have performed further simulations by decreasing the cation-electron binding strength, taking $R_c = 4.36a_0$. In this case, extreme localization is not sufficiently counterbalanced by e binding. Instead, the planar structure transforms to the isomeric pyramidal configuration with the electron localized as a diffuse cloud about the tip of the pyramid [Fig. 1(h)]. Electron localization accompanied by structural isomerization will constitute a prevalent phenomenon for AHC with smaller e-cation binding energy, i.e., the heavier alkali metals. In view of the intimate interrelationship between structural isomerization and melting of clusters,[16] it will be interesting to explore the melting of such finite systems induced by electron localization.

[1]See papers in Ber. Bunsenges. Phys. Chem. **88** (1984).

[2]C. L. Briant and J. J. Burton, J. Chem. Phys. **63**, 2045 (1975).

[3]See review by F. F. Abraham, J. Vac. Sci. Technol. **82**, 534 (1984).

[4]J. Jortner, in Ref. 1, p. 188.

[5]D. Chandler and P. G. Wolynes, J. Chem. Phys. **79**, 4078 (1981).

[6]B. De Raedt, H. Sprik, and H. L. Klein, J. Chem. Phys. **80**, 5719 (1984).

[7]D. Chandler, J. Phys. Chem. **88**, 3400 (1984).

[8]M. Parrinello and A. Rahman, J. Chem. Phys. **80**, 860 (1984).

[9]T. P. Martin, Phys. Rep. **95**, 167 (1983).

[10]F. G. Fumi and M. P. Tosi, J. Phys. Chem. Solids **25**, 31, 45 (1964).

[11]R. W. Shaw, Phys. Rev. **174**, 769 (1968).

[12]L. S. Schulman, *Techniques and Applications of Path Integrals* (Wiley, New York, 1981).

[13]M. F. Herman, E. J. Bruskin, and B. J. Berne, J. Chem. Phys. **76**, 5150 (1982).

[14]D. Callaway and A. Rahman, Phys. Rev. Lett. **49**, 613 (1982).

[15]N. F. Mott and R. W. Gurney, *Electronic Processes in Ionic Crystals* (Oxford Univ. Press, Oxford, 1946).

[16]G. Natanson, F. Amar, and R. S. Berry, J. Chem. Phys. **78**, 399 (1983).

II.

VIBRATIONAL PREDISSOCIATION INDUCED BY EXCITON TRAPPING IN INERT-GAS CLUSTERS

Dafna SCHARF, Joshua JORTNER

School of Chemistry, Tel-Aviv University, 69978 Tel Aviv, Israel

and

Uzi LANDMAN

School of Physics, Georgia Institute of Technology, Atlanta, GA 30322, USA

The dynamics of exciton trapping, vibrational energy transfer and vibrational predissociation in an electronically excited state of Ar_{13} clusters was explored by classical molecular dynamics. Two distinct time scales were established for vibrational energy flow, which result in a molecular-type, reactive dissociation process of Ar atoms for this cluster.

The processes of energy acquisition, storage and disposal in clusters are of considerable interest for the elucidation of dynamic processes in finite systems, whose energy spectrum for electronic and nuclear excitations can be varied continuously by changing the cluster size [1]. In this context, an important issue involves the consequences of vibrational excitations of clusters. Such relaxation processes fall into two categories: (i) non-reactive vibrational energy redistribution in the cluster, which does not result in dissociation, and (ii) reactive dissociation or vibrational predissociation. The mechanisms of vibrational energy acquisition by a cluster can involve collisional excitation, optical photoselective vibrational excitation or electronic excitation followed by the degradation of electronic energy into vibrational energy. In charged clusters, the vibrational excitation resulting in both non-reactive and reactive relaxation, can originate from ionization followed by hole trapping in inert-gas clusters [2–5] and from electron attachment to alkali halide clusters [6]. Information regarding the reactive consequences of vibrational excitation of small neutral clusters in their ground electronic state stems from two sources. First, molecular dynamics computer simulations of the dissociation of Ar_n ($n = 4–6$) clus-

ters [7] can be accounted for in terms of the statistical theory of unimolecular reactions [8], which implies the occurrence of vibrational energy randomization in small clusters. Second, experimental molecular beam studies of optically vibrationally excited hydrogen-bonded $(HF)_n$ ($n = 2–6$) clusters [9] yield a lower limit of $>10^6$ s^{-1} for the vibrational predissociation rate at the excess vibrational energy of 3000 cm^{-1}, and do not yet provide information on the interesting issue of intramolecular vibrational energy redistribution in these systems. The non-reactive and reactive processes induced by the degradation of electronic energy into vibrational energy in clusters have not yet been elucidated. An interesting problem in this category involves the dynamical consequences of exciton trapping in rare-gas clusters (RGCs), which is the subject matter of this note. Extensive information is currently available regarding exciton trapping in solid and liquid inert gases [10]. Exciton trapping in the heavy rare-gas solids, i.e. Ar, Kr and Xe, exhibits two-centre localization, resulting in the formation of electronically excited, diatomic rare-gas excimer molecules. Electronic excitation of a RGC, R_n, is expected to result in an exciton state, which subsequently becomes trapped by self-localization. Although the details of

the energetics and spatial charge distribution of excitons in finite RGCs have not yet been explored, some information can be drawn from the analogy with the lowest electronic excitations in solid and liquid rare gases, which can adequately be described [10] either in terms of intermediate Wannier exciton states with large central cell corrections, or by strongly perturbed Frenkel excitons. Adopting the latter approach, the two lowest, dipole allowed, electronic excitations in RGCs can adequately be described in terms of tightly bound, Frenkel-type excitations with a parentage in the $^1S_1 \rightarrow ^3P_1$ and $^1S_0 \rightarrow ^1P_1$ atomic excitations, which are modified by large non-orthogonality corrections [10]. The energetic separation between these two electronic excitations corresponds to the spin–orbit splitting [10]. This description of the electronic excitations rests on a decidedly molecular description. An analogous molecular point of view [11] is adopted for the description of exciton trapping in RGCs. The process of exciton trapping in the heavy RGCs of Ar, Kr and Xe involves the formation of the diatomic excimer molecule R_2^*, which is characterized by a substantial binding energy for a high vibrational state. Energy exchange between the R_2^* excimer and the cluster in which it is embedded involves two processes:

(1) Short-range repulsive interactions between the expanded, Rydberg-type excited state of the excimer and the other cluster atoms result in a dilation of the local structure around the excimer, leading to energy flow into the cluster.

(2) Vibrational relaxation of the excimer induces vibrational energy flow into the cluster.
The vibrational energy released into the cluster by processes (1) and (2) may result in vibrational predissociation.

We have explored the dynamic implications of exciton trapping in RGCs by conducting classical molecular dynamics (MD) calculations [12,13] on electronically excited states of such clusters. Applications of MD to photophysical processes start to emerge. MD simulations of photochemical dissociation and radical back recombination in clusters were recently reported [14]. The present work constitutes an application of the MD technique for the dynamics of electronically–vibrationally excited states of large systems. As a model system we have chosen the Ar_{13} cluster. Our calculations are based on additive pairwise interactions. The ground states of the RGCs have been described by

additive Lennard-Jones pair potentials, $V(r) = 4\epsilon[(\sigma/r)^{12} - (\sigma/r)^6]$, which are specified by $\epsilon = 121$ K and $\sigma = 3.40$ Å [15]. In the electronically excited state the Ar_2^* excimer potential is represented by a Morse curve, $V(r) = D_e \{\exp[-2B(r/R_e - 1)] - 2\exp[-B(r/R_e - 1)]\}$ with the parameters $D_e = 0.78$ eV, $R_e = 2.32$ Å and $B = 5.12$ [16]. An important consequence of the electronic excitation involves the drastic modification of the interaction between the excimer and the ground-state atoms. On the basis of the analysis of Xe^*-Ar interactions [17], the Ar^*-Ar potential for each of the constituents of the excimer has been described in terms of a Lennard-Jones potential with the parameters ϵ^* and σ^*. We have taken for the energy $\epsilon^* = \epsilon$, while the distance scale ratio $\bar{\sigma} = \bar{\sigma}^*/\sigma$ has been chosen in the range $\bar{\sigma} = 1.0-1.2$. The appropriate Ar^*-Ar interaction is characterized by [17] $\bar{\sigma} = 1.10-1.15$, reflecting the enhancement of short-range repulsive interactions in the electronically excited Rydberg-type state.

The ground-state equilibrium configuration of Ar_{13} was generated following a lengthy equilibration (5 × 10^4 integration steps) at a temperature $T = 24$ K, which is lower than the melting temperature ($T \approx 40$ K) [18-20] of this cluster. We find that at this temperature the Ar_{13} cluster assumes the icosahedron structure, which is in accord with previous results [20, 21]. Electronic excitation was performed on a particular equilibrated ground-state cluster configuration. The electronic excitation was achieved (at the time $t = 0$) by the instantaneous switching on of the excimer potential between a pair of atoms and of the Ar^*-Ar potentials between the excimer and the ground-state atoms. We have adopted a local picture, disregarding the effects of electronic energy transfer within the cluster.

A fifth-order predictor–corrector method, which constitutes a very accurate version of the MD algorithm [22] has been used. The time increment in the ground state was $\Delta t = 1.6 \times 10^{-14}$ s. The larger forces and the abrupt velocity changes in the system following electronic excitation require shorter time increments. Accordingly, we have used $\Delta t = 1.6 \times 10^{-16}-5.0 \times 10^{-16}$ s in this electronically excited state. In all our MD calculations conservation of energy prevailed with an accuracy of 1 ppm.

In figs. 1a and 1b we show an overview of the dynamics of the nuclear motion following the electron-
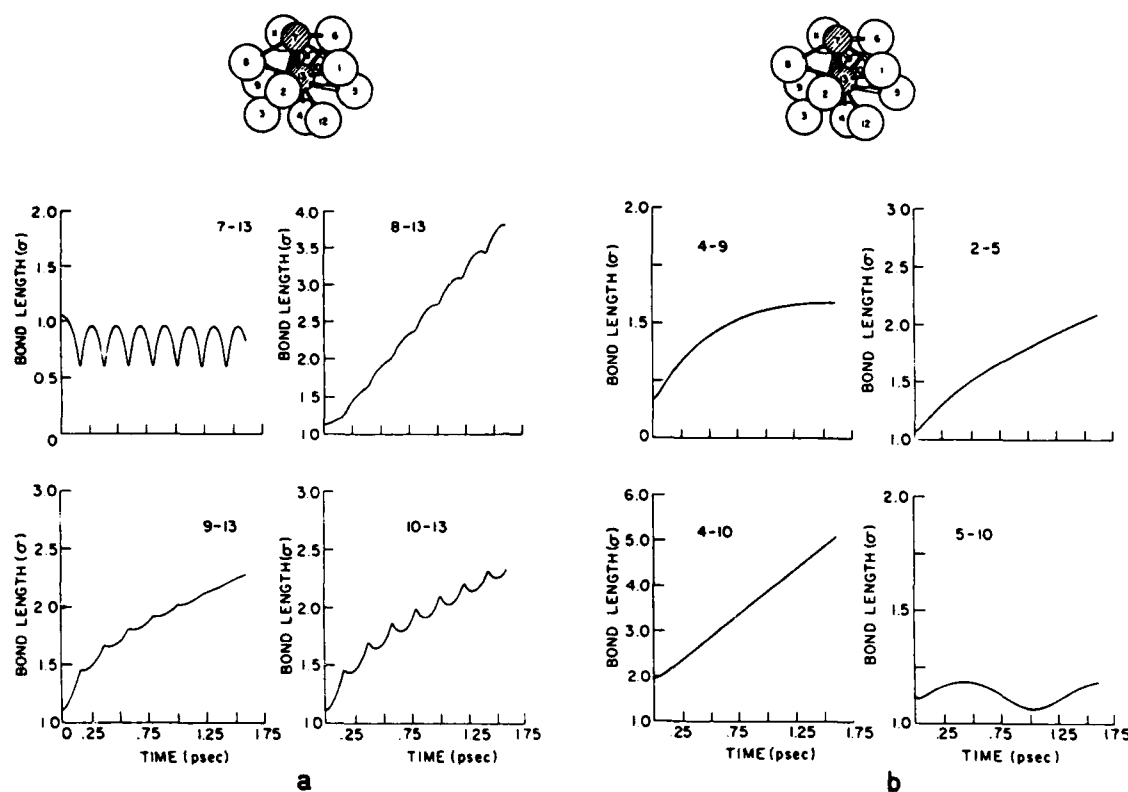
496

Fig. 1. Time dependence of interatomic distances in the electronically excited Ar_{13}^* cluster. The insert shows the ground-state equilibrium structure at 24 K. The labelling of atoms is indicated. The dashed atoms 7 and 13 form the excimer. Distances are in units of σ. The Ar^*-Ar interaction is characterized by $\bar{\sigma} = 1.20$. (a) Interatomic distances within the excimer and between the excimer atoms and some ground-state atoms. (b) Interatomic potentials between some ground-state atoms.

ic excitations, which is expressed in terms of the inter-atomic distances. The excimer exhibits a large-amplitude motion in a highly excited vibrational state, while all the other interatomic distances increase, indicating the initiation of the escape of the ground-state cluster atoms. Insight into the energy flow from the excimer into the cluster is obtained from the time dependence of the kinetic energy (KE), the potential energy (PE) and the total energy of the excimer (fig. 2). The strong oscillations in the PE and KE clearly indicate the persistence of the vibrational excitation of the excimer over a long time scale. Further detailed information concerning the implications of this ener-

gy flow on the cluster dissociation was inferred by considering the composition and the energetics of the "main fragment", i.e. the fragment which consists of the excimer together with ground-state atoms, with all the nearest-neighbour separations being smaller than 3σ, beyond which all interatomic interactions are negligibly small. The total energy within the main fragment was partitioned into two separate contributions: (i) the energy of the "reaction centre", which consists of the excimer PE and KE together with half of the sum of the potential energy of the Ar^*-Ar interactions, and (ii) the energy of the "bath subsystem", which involves the KE of the ground-state Ar atoms,
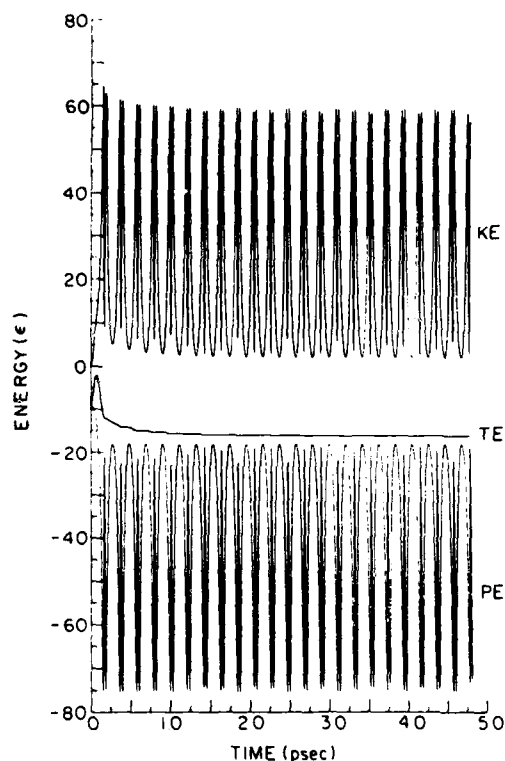
497

Fig. 2. Time dependence of the potential energy (PE), the kinetic energy (KE) and the total energy (TE) of the bare excimer in Ar_{13} ($\bar{\sigma}$ = 1.20). Energies are given in units of ϵ.

the potential energies of the Ar–Ar interactions and half of the sum of the potential energies of the Ar^*– Ar interactions. The time evolution of the various contributions to the total energy (fig. 3) portray the energy flow from the excitation centre into the "bath". However, the energy per atom does not equilibrate. Discontinuities (i.e. "steps") in the energy plots of fig. 3 mark the dissociation of the main fragment, with the decrease of the total energy corresponding to the KE of the ground-state atoms dissociating from it. A cursory examination of the time evolution of the composition of the main fragment (fig. 3) clearly indicates that the major fragmentation process involves the sequential stepwise dissociation, i.e. "evaporation", of single ground-state atoms from the main fragment. The

escape of the excimer from the main fragment has not been encountered. The dissociation process is dominated by the magnitude of the excited-state potential scale parameter $\bar{\sigma}$. For realistic values [17] of $\bar{\sigma}$ = 1.10–1.15, the threshold for cluster dissociation is exhibited on the time scale of ≈ 2–20 ps (fig. 4). In an extreme case, when extra excited-state repulsive interactions are switched off, i.e. when $\bar{\sigma}$ = 1.20, the onset for dissociation is exhibited on the 1 ps time scale and is complete within 10 ps.

From these MD results the following picture concerning vibrational energy flow and reactive dynamics of the Ar_{13} cluster emerges. The temporal persistence of the vibrational excitation of the excimer (fig. 2) and of the "reaction centre" (fig. 3) corresponds to a "mode selective" excitation of the excimer, with vibrational energy redistribution within the cluster being precluded by two effects. First, the difference in the characteristic frequencies of the (high frequency) dimer motion and the (low frequency) motion of the cluster. Second, the local dilation of the cluster structure around the excimer, which is induced by the short-range excimer–cluster repulsive interactions. The vibrational energy flow from the dimer into the cluster (figs. 2 and 3) consists of two stages.

(A) Ultrafast vibrational energy transfer due to repulsion, which occurs on the time scale of ≈ 200 fs (figs. 2 and 3). This energy transfer process is dominated by the magnitude of the scale parameter $\bar{\sigma}$, being prominent for $\bar{\sigma}$ = 1.10–1.20, with the amount of energy transferred from the excimer to the cluster decreasing with decreasing $\bar{\sigma}$ in the range $\bar{\sigma}$ = 1.20– 1.10, while the characteristic time scale for the process is practically invariant with respect to changes of $\bar{\sigma}$ in this narrow range. For $\bar{\sigma}$ = 1.00 this process is switched off.

(B) "Slow" energy transfer on the time scale of tens of picoseconds (for $\bar{\sigma}$ = 1.20) and up to hundreds of picoseconds (for $\bar{\sigma}$ = 1.00) due to vibrational relaxation of the excimer.

The dynamics of the cluster induced by these energy transfer processes involves reactive vibrational predissociation, as is apparent from figs. 3 and 4. This state of affairs is, of course, drastically different from that encountered in infinite systems, where a non-reactive process prevails when the phonon modes of the system are excited. A cursory examination of the dissociative dynamics (fig.4) of the Ar_{13} cluster fol-
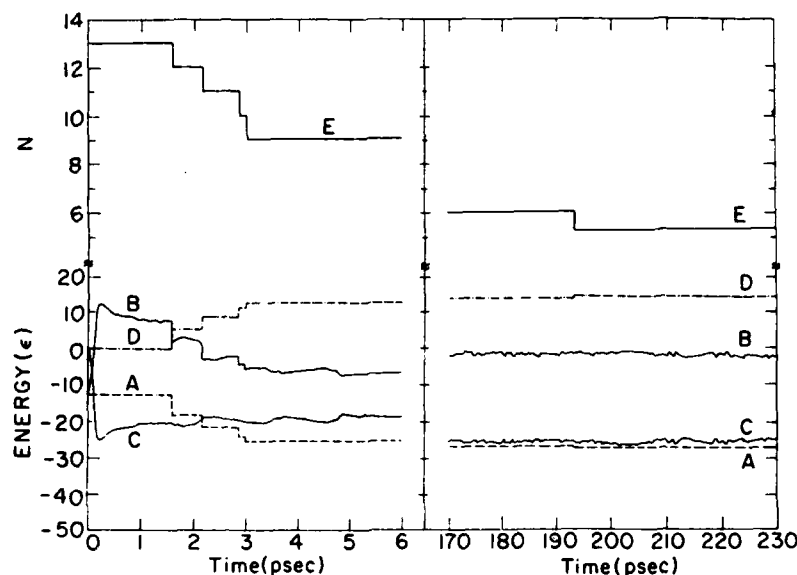
Fig. 3. Time evolution of fragmentation dynamics of the electronically exci ~d $(Ar)_{13}$ cluster ($\bar{\sigma} = 1.15$). (A) Total energy of the main fragment. (B) Total energy of the "bath subsystem". (C) Total energy of the "reaction centre". (D) Kinetic energy of the dissociated atoms. (E) Number of atoms in the main fragment. The steps in curves (A), (D) and (E) mark the stepwise dissociation of individual Ar atoms from the main fragment.

lowing excimer formation indicated that two reactive processes prevail.

(C) A fast stepwise "evaporation" of Ar atoms is exhibited on the time scale of ≈ 10 ps.

This process is induced by the energy transfer process (A). Subsequently, an additional reactive process appears (fig. 4), which involves:

(D) Slower vibrational predissociation of Ar atoms on the time scale $\geqslant 10$ ps. This dissociative process is induced both by energy transfer processes (A) and (B).

It is imperative to note that the short-time "explosion" of the electronically excited cluster is induced by energy transfer due to short-range repulsive interactions. When these interactions are switched off by taking $\bar{\sigma} = 1.00$, only mechanism (B) is operative for vibrational energy flow into the cluster and the cluster dissociative process, which again occurs by stepwise "evaporation" occurring on the time scale of 100–1000 ps. The appropriate excited-state repulsive physical parameter characterizing excimer–cluster interactions in RGCs is $\bar{\sigma} = 1.10–1.20$, and we expect the occurrence of energy flow predissociation induced by excited repulsive interactions to occur on the time
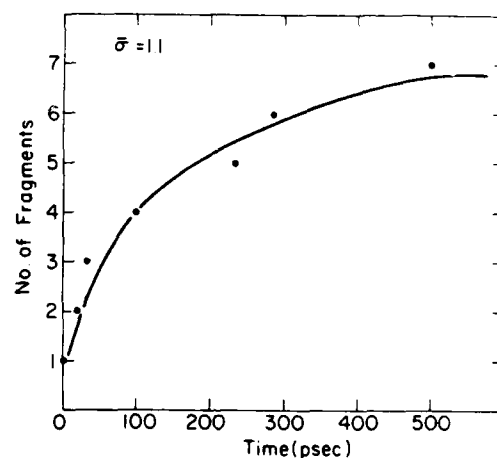

Fig. 4. The time evolution of the fragmentation of the electronically excited $(Ar)_{13}$ cluster ($\bar{\sigma} = 1.10$). Note the sequential "evaporation" of the single grond-state Ar atoms.

scale ≈ 10 ps. These predictions have not yet been subjected to an experimental test.

We conclude this analysis of molecular dynamics

499

in electronically excited states of RGCs with several comments. Firstly, a new mechanism of ultrafast vibrational energy flow induced by short-range repulsions has been documented. This mechanism will be of considerable importance for energy exchange between an extravalence (Rydberg) excitation and a cluster. Secondly, in small ($n = 13$) clusters the consequences of vibrational energy flow into the cluster involve a reactive dissociative process. Reactive vibrational predissociation manifests the dynamic consequence of vibrational energy flow into small clusters. Another extreme situation corresponds to infinite systems, where non-reactive vibrational energy redistribution prevails. It will be extremely interesting to increase the cluster size to establish the "transition" from reactive vibrational predissociation and "non-reactive" vibrational excitation of the cluster modes. Recent MD simulation on the dynamics of $Ar_{11}Xe_2^*$ and $Ar_{53}Xe_2^*$ clusters have established the "transition" from the reactive molecular-type behaviour in small clusters to the solid-state-type non-reactive behaviour in the large cluster [23]. Thirdly, the $Ar_{11}Ar_2^*$ electronically excited cluster provides an example of a system where "statistical" vibrational energy redistribution does not occur. The "mode selective" excitation of the excimer in the cluster constitutes a nice example for the violation of vibrational energy equipartitioning in a large finite system.

Acknowledgement

References

[1] J. Jortner, Ber. Bunsenges. Physik. Chem. 88 (1984) 188.

[2] H. Haberland, Surface Sci. 156 (1985) 305.

[3] J.J. Sáenz, J.M. Soler and N. Garcia, Surface Sci. 156 (1985) 121.

[4] J.J. Sáenz, J.M. Soler, N. Garcia and O. Echt, Chem. Phys. Letters 109 (1984) 71.

[5] E.E. Polymeropoulos and J. Brickmann, Surface Sci. 156 (1985) 563.

[6] U. Landman, D. Scharf and J. Jortner, Phys. Rev. Letters 54 (1985) 1860.

[7] J.W. Brady and J.D. Doll, J. Chem. Phys. 73 (1980) 2767.

[8] S.A. Rice, Advan. Chem. Phys. 47 (1982) 117.

[9] M.F. Vernon, D.J. Kraynovich, H.S. Kwok, J.M. Lisy, Y.R. Shen and Y.T. Lee, J. Chem. Phys. 77 (1982) 47.

[10] N. Schwentner, E.E. Koch and J. Jortner, Electronic excitations in condensed rare gases. Springer tracts in modern physics, Vol. 107 (Springer, Berlin, 1985).

[11] J. Jortner, E.E. Koch and N. Schwentner, in: Photophysics and photochemistry in the Vacuum Ultraviolets, eds. S.P. McGlynn, G.L. Findley and R.H. Huebner (Reidel, Dordrecht, 1985) p. 515.

[12] J.R. Beeler and G.L. Kulcinski, in: Interatomic potentials and simulation of lattice defects, eds. P.C. Gehlen, J.R. Beeler and J. Jaffee (Plenum Press, New York, 1972) p. 735.

[13] A. Raman and F.H. Stillinger, J. Chem. Phys. 55 (1971) 3336.

[14] F.G. Amar and B.J. Berne, J. Phys. Chem. 88 (1984) 6720.

[15] W.D. Kristensen, E.J. Jensen and M.J. Cotterill, J. Chem. Phys. 60 (1974) 4161.

[16] K.T. Gillen, R.P. Saxon, D.C. Lorentz, G.E. Ice and R.E. Olson, J. Chem. Phys. 64 (1976) 1925.

[17] I. Messing, B. Raz and J. Jortner, J. Chem. Phys. 66 (1977) 2239, 4577.

[18] G.L. Briant and J.J. Burton, J. Chem. Phys. 63 (1975) 2045.

[19] N. Quirke and P. Sheng, Chem. Phys. Letters 110 (1984) 63.

[20] J.B. Kaelberer and R.D. Etters, J. Chem. Phys. 66 (1977) 3233.

[21] M.R. Hoare and P. Pal, Advan. Chem. Phys. 40 (1979) 49.

[22] A. Nordsieck, Math. Comp. 16 (1962) 22.

[23] D. Scharf, J. Jortner and U. Landman, to be published.

ATOMIC AND MOLECULAR QUANTUM MECHANICS
BY THE PATH INTEGRAL MOLECULAR DYNAMICS METHOD

Dafna SCHARF, Joshua JORTNER

School of Chemistry, Tel-Aviv University, 69978 Tel Aviv, Israel

and

Uzi LANDMAN

School of Physics, Georgia Institute of Technology, Atlanta, GA 30332, USA

Received 16 August 1986

The quantum path integral molecular dynamics method was applied to studies of excess electron localization by a Na^+ ion and by a NaCl molecule. Spatial and energetic characterization of the ground state of the excess electron compare favorably with results of model potential calculations for Na and with SCF CI calculations for $NaCl^-$.

1. Introduction

The properties of an excess electron in condensed matter systems [1–3] and in finite clusters [4] are of fundamental importance. Excess electron states in dense fluids [5–7] and in clusters [8] have recently been explored using the quantum path integral formulation of statistical mechanics [9,10] utilizing the quantum path integral molecular dynamics method (QUPID) [5–10], as well as the Monte Carlo technique [11]. While extensive data are available concerning excess electron states in fluids [1–3], experimental information concerning excess electron in clusters [4] is meagre. Recent computer simulations, which demonstrated the energetic stability of a localized electron state and the possibility of isomerization induced by electron localization in alkali halide ionic clusters [8], are not yet amenable to confrontation with experiment. In this note we apply the QUPID method to electron binding to two simple systems, which involve the elementary ingredients of the alkali halide (AH) system used in previous studies [8], i.e. a Na^+ ion and a NaCl molecule. These calculations were undertaken to demonstrate that one can obtain quantitative information for the energetics and for the charge distribution of an excess elec-

tron attached to small ionic systems, establishing confidence in the QUPID method in conjunction with the pseudopotential formalism [12–14] for electron–ion interactions, and thus providing reliable results for electron localization in ionic clusters [8].

2. Methodology

The QUPID method was used to simulate an electron interacting with a Na^+ ion or with a NaCl (AH) molecule. While the heavy atoms, whose thermal wavelength is very small, are reasonably treated by classical mechanics, a quantum treatment is essential for the electron. The partition function Z for a single electron in the external potential of the ions V_e is

$$Z = \mathrm{Tr}[\exp(-\beta H_e)] , \tag{1}$$

where $H_e = K_e + V_e$, K_e is the electron kinetic energy and $\beta = 1/kT$. An approximate expression for the partition function, which is amenable to numerical computations, can be obtained [10] through the use of Trotter's formula and the free-particle propagator

in coordinate representation, yielding

$$Z \approx \mathrm{Tr}[\exp(-\beta K_c/P)\,\exp(-\beta V_c/P)]^P$$

$$= \left(\frac{Pm}{2\hbar^2\beta\pi}\right)^{3P/2}$$

$$\times \int \dots \int d\mathbf{r}_1 \dots d\mathbf{r}_P \exp[-\beta V_{\mathrm{eff}}(\mathbf{r}_1 \dots \mathbf{r}_P)] , \quad (2)$$

where m is the mass of the electron and the effective potential is

$$V_{\mathrm{eff}} = \sum_{i=1}^{P}\left(\frac{Pm}{2\hbar^2\beta^2}(\mathbf{r}_i - \mathbf{r}_{i+1})^2 + \frac{1}{P}V_c(\mathbf{r}_1 \dots \mathbf{r}_P)\right). \quad (3)$$

The external potential V_c incorporates the electron–ion interactions corresponding to the e–Na$^+$ interaction for Na and the sum of e–Na$^+$ and e–Cl$^-$ interactions for the NaCl$^-$ system. Core exclusion effects are very important for the e–Na$^+$ interaction and are dealt with through a local pseudopotential, which can be replaced by a two-parameter simple model potential [13,14]. The e–Na$^+$ model potential, V_{cA}, for the electron chain is [14]

$$V_{cA} = -\frac{1}{P}\sum_{i=1}^{P}\frac{e^2}{r_{iA}}, \qquad r_{iA} \geqslant R_c ,$$

$$= -\frac{1}{P}\sum_{i=1}^{P}\frac{e^2}{R_c}\theta(R_c - r_{iA}) , \quad r_{iA} \leqslant R_c , \quad (4)$$

where R_c is a cutoff radius and θ is the Heaviside step function. For Na$^+$ we take $R_c = 3.22$ au [14].

The e–Cl$^-$ interaction, V_{cH}, is modelled by a Coulomb repulsion from the closed-shell anion and thus the core exclusion contribution is expected to be very small. The Coulomb interaction is complemented by the electron-induced polarization interactions, which is operative at distances larger than the ionic radius, R_I, of the Cl$^-$ ion, and is corrected for the "self-energy" of the induced dipole. This core polarizability contribution accounts for electron correlation effects.

$$V_{cH} = \frac{1}{P}\sum_{i=1}^{P}\left(\frac{e^2}{r_{iH}} - \frac{e^2\alpha_H}{2r_{iH}^4}\right), \quad r_{iH} \geqslant R_I ,$$

$$= \frac{1}{P}\sum_{i=1}^{P}\frac{e^2}{r_{iH}}, \qquad r_{iH} < R_I , \quad (5)$$

where α_H is the anion polarizability. We note in pass-

ing that the polarizability contribution was not incorporated in the e–Na$^+$ potential, eq. (4), as the model potential parameters were chosen to fit the spectroscopic data.

For the interaction between the ions, V_{AH}, two model potentials were used. In the simplest form the interaction is a sum of the Coulomb attraction and the Born–Mayer repulsion with the parameters $\tilde{A}$ and ρ given by Fumi and Tosi (FT) [15],

$$V_{AH} = -e^2/R_{AH} + \tilde{A}_{AH}\exp(-R_{AH}/\rho) . \quad (6)$$

The second form for the interionic potential is based on a truncated Rittner model, which was developed by Brumer and Karplus (BK) [16]. It accounts for the charge–induced-dipole interaction via effective ionic polarizability α_H and α_A of the anion and the cation, respectively, and for the van der Waals attraction at short distances. The potential parameters $\tilde{A}'$, ρ' and c were given by BK [16]

$$V_{AH} = -e^2/R_{AH} + \tilde{A}'_{AH}\exp(-R_{AH}/\rho')$$

$$\quad - e^2(\alpha_A + \alpha_H)/2R_{AH} - c/R_{AH}^6 . \quad (7)$$

The average energy of the electron is evaluated at thermal equilibrium from the exact relation

$$E_e = -\partial \ln Z/\partial\beta , \quad (8)$$

resulting in

$$E_e = KE_e + PE_e , \quad (9)$$

where

$$KE_e = \frac{3P}{2\beta} - \frac{Pm}{2\hbar^2\beta^2}\left\langle\sum_{i=1}^{P}(\mathbf{r}_i - \mathbf{r}_{i+1})^2\right\rangle \quad (10a)$$

and

$$PE_e = \frac{1}{P}\sum_{i=1}^{P}V_c(\mathbf{r}_1 \dots \mathbf{r}_P) . \quad (10b)$$

KE_e is the kinetic energy and PE_e represents the potential energy of the electron. An estimator for the kinetic energy, which avoids the errors incurred by the subtraction of large quantities was advanced by Herman et al. [17],

$$KE_e = \frac{3}{2\beta}$$

$$+ \frac{1}{2P}\sum_{i=1}^{P}\left\langle\left(\frac{\partial V_{cA}}{\partial \mathbf{r}_i} + \frac{\partial V_{cH}}{\partial \mathbf{r}_i}\right)\cdot(\mathbf{r}_i - \mathbf{r}_P)\right\rangle . \quad (11)$$

505

The kinetic energy of the electron consists of the free particle term and the kinetic energy of interaction with the ions. Together with the energies of the classical particles, the energy of the system is

$$E = 3N/2\beta$$

$$+ \langle V_{AH} \rangle + KE_e + \langle V_{eA} \rangle + \langle V_{eH} \rangle . \qquad (12)$$

The averages, which are denoted by the angular brackets, are taken over the Boltzmann distribution as defined by eqs. (2) and (3). In the classical isomorphism the statistical ensemble averages can be replaced by averaging over trajectories generated via classical molecular dynamics by the Hamiltonian

$$H = \sum_{i=1}^{P} m^* \dot{r}_i^2$$

$$+ M_A \dot{R}_A^2 + M_H \dot{R}_H^2 + V_{eA} + V_{eH} + V_{AH}$$

$$+ \sum_{i=1}^{P} \frac{Pm}{2\hbar^2\beta^2} (r_i - r_{i+1})^2 . \qquad (13)$$

Since the equilibrium thermodynamic averages do not depend on the masses which appear in the kinetic energy term for the pseudo-particles, an arbitrary mass can be assigned to m^*. We note that the trajectories in the QUPID method do not correspond to the real-time dynamical evolution of the system and the method is limited to the calculation of equilibrium properties.

3. Numerical procedure

The preparation of the systems in thermal equilibrium (50 K) consisted of several stages. Initially, the electron bead particles ($P = 998$) which were distributed over a sphere around the Na$^+$ (or the NaCl), were allowed to approach the ion(s), while the kinetic energy was controlled. Then, constant energy trajectories for the MD Hamiltonian (eq. (13)) were generated for a large number of integration steps (5×10^4 in Na and 7.5×10^4 in NaCl$^-$) before averaging was performed over the subsequent integration steps (2×10^4 in Na and 5×10^4 in NaCl$^-$). Energy was conserved in all runs, to better than 0.05% over 10^5 integration steps.

Table 1
QUPID calculations for Na$^+$ + e. Potential energy (PE), kinetic energy (KE) and total binding energy (BE) of an electron to a Na$^+$ ion compared with the experimental ionization potential (IP) of a sodium atom. The energy variance is given in parentheses. All energies are given in hartree units

	PE	KE	BE	IP experiment [a]
eq. (10)	−0.2504	0.0657	0.1847	0.1889
	(0.0003)	(0.008)	(0.008)	
eq. (11)	−0.2504	0.0654	0.1850	
	(0.0003)	(0.0001)	(0.0004)	

[a] See ref. [18].

4. Results and discussion

4.1. e + Na$^+$

The calculated energies for the binding of the electron at 50 K are given in table 1. The kinetic energy value using the estimator given in eq. (11), is more accurate than that obtained from eq. (10a), in accord with previous results [8,11]. The binding energy compares well with the experimental results and with conventional quantum-mechanical calculations [19] and pseudopotential calculations [13], inspiring confidence in the QUPID method and the model potential which was employed for the alkali-ion–electron interaction. In fig. 1a we show a snapshot of the electron bead particles projected on a 2D plane, exhibiting a uniform spherical distribution around the sodium ion. The normalized radial distribution for the positions of the pseudo-particles (beads) around the Na$^+$ is given by the probability distribution function

$$g(r) = \frac{1}{P} \sum_r n(r, \Delta r) , \qquad (14)$$

where $n(r, \Delta r)$ is the number of pseudo-particles in a shell of radius r and thickness Δr, centered around the ion. $g(r)$ is compared with numerical information for the Hartree–Fock–Slater radial 3s wavefunction for the valence electron in sodium [19]. In fig. 2 we show the histogram of the averaged radial distribution of the bead particles along with the 3s probability distribution for the Na atom.

The extent of localization of the electron is closely related to the distribution of distances between the pseudo-particles, which represent points on the elec-
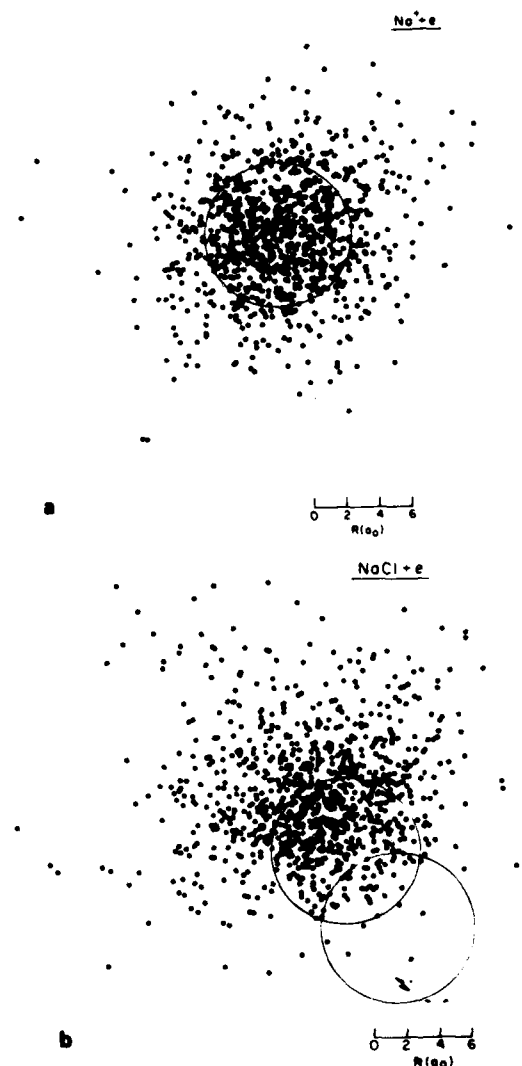
Fig. 2. Histogram of the calculated radial distribution for the electron bead particles for $e + Na^+$. The probability distribution for the 3s orbital in Na from a Hartree–Fock calculation [19] is given by the dashed line.

Fig. 1. Snapshots of the electron bead particles projected on a 2D plane. (a) $e + Na^+$, (b) $e + NaCl$. The large open circles correspond to the cutoff radius in the local model potential for the Na^+ core and for the ionic radius in Cl^-. The lower circle corresponds to the Cl^- anion.

tron path. We can estimate the "breadth" of the quantum particle by examining moments of the pseudo-particle distribution. We define

$$R_T^f = \left(\frac{P}{P-1} \sum_{i=1}^{P} \langle (r_i - r_{i+1})^2 \rangle \right)^{1/2} ,$$
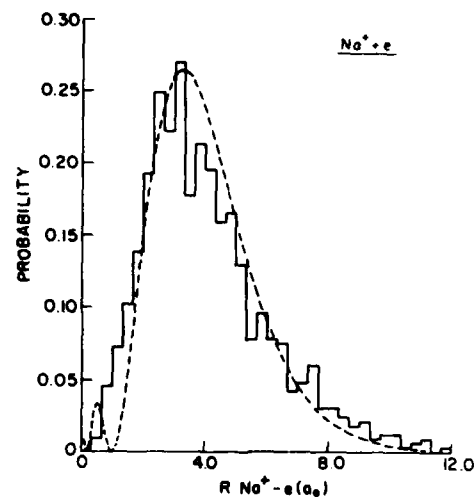
which for a free electron with the distances between pseudo-particles obeying Gaussian statistics yields $R_T^f = 3^{1/2} \lambda_T$, where $\lambda_T = \beta \hbar^2/m$ is the thermal wavelength of the electron. At 50 K, $\lambda_T \approx 80 \ a_0$ and $R_T^f = 120 \ a_0$, being close to the value of $R_T = 136 \ a_0$, which we find for the $e-Na^+$ system. The interactions of the quantum particle with the ions tend to confine the pseudo-particle chain to a "localized form". The second moment of the bead distribution is proportional to the gyration radius of the chain:

$$R_s^2 = \frac{1}{2P^2} \left\langle \sum (r_i - r_j)^2 \right\rangle . \tag{15}$$

We have found $R_s = 4.53 \pm 0.04 \ a_0$ with the three components, $R_{gx} = 2.64 \pm 0.05 \ a_0$, $R_{gy} = 2.66 \pm 0.4 \ a_0$ and $R_{gz} = 2.55 \pm 0.12 \ a_0$, exhibiting an isotropic electron distribution centered around the ion. The value for R_s is considerably lower than λ_T.

The compression of the pseudo-particle chain (degree of localization) can be analyzed in terms of the self-pair time-correlation function [20]:

$$R^2(t-t') = \langle |r(t) - r(t')|^2 \rangle . \tag{16}$$

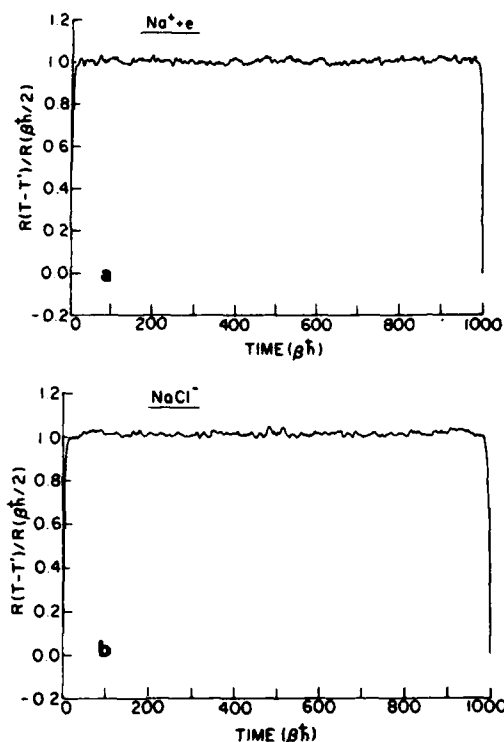$R(t-t')$ is the rms value of the displacement between

507

Fig. 3. The self-pair time-correlation function. The values of $R(t-t')$ are normalized to the corresponding characteristic length $R(\beta\hbar/2)$. (a) $e+Na^+$, (b) $e+NaCl$.

two points on the electron path separated by an imaginary time increment $0 \leq t-t' \leq \beta\hbar$. The characteristic size of such a chain is given by $R(\beta\hbar/2)$ [20]. A localized configuration of the quantum particle chain corresponds to a pronounced deviation of R from the free-particle value. We have found that $R(\beta\hbar/2) = 2.53\ a_0$, whereas $R_{free} = (\frac{1}{4})^{1/2}(\beta\hbar^2/m)^{1/2} \approx 69\ a_0$. Accordingly, the localization condition is well met, as is expected. In fig. 3a we plot $R(t-t')$ versus time. For a localized state, fluctuations in $R(t-t')$ are inhibited due to the dominance of the ground-state contribution, yielding independence of $R(t-t')$ on t, except for small intervals of magnitude τ near 0 and $\beta\hbar$. The range of variation of $R(t-t')$ at the edges of the interval (in $\beta\hbar$ units) is equal to the reciprocal of the mean excitation energy to the manifold of the excited states, i.e. mainly to the first excited state. We have found this mean excitation

energy to be 2.1 ± 0.2 eV, which agrees favorably with the experimental values 2.102 and 2.104 eV for the lowest electronic excitations of Na.

4.2. e+NaCl

The binding energy of the electron to the NaCl diatomic molecule was calculated by taking the difference between the total energy of $NaCl^-$ and of NaCl. The calculated energies and equilibrium distances are given in table 2 for $NaCl^-$ and in table 3 for NaCl. The calculations for the NaCl molecule were performed by classical MD. We have found the calculated excess electron binding energy, i.e. the electron affinity of NaCl to be in the range $EA = 0.9-1.0$ eV with an uncertainty of ± 0.1 eV. The equilibrium distance of $NaCl^-$ is calculated to be $R_e = 4.66-4.84$ a_0. The electron affinity calculation of Jordan et al. for $NaCl^-$ in an unrestricted Hartree–Fock method [22] resulted in $EA = 0.65$ eV for the equilibrium ion separation $R_e = 4.74\ a_0$. The agreement between the Hartree–Fock result [22] and ours for EA and for R_e is as good as can be expected in view of the uncertainties inherent in both the self-consistent field method and in our use of simple model potentials.

Table 2
QUPID calculations for NaCl–e. Kinetic energy (KE), potential energy (PE), total energy (E_{tot}) for the classical ions and for the electron. Under electron K_{est} and KE are the kinetic energies according to eqs. (11), (10), respectively. Total energy of NaCl + e (E_{tot}) and the binding energy for the electron (BE). Equilibrium distance (R_e). Numbers in parentheses represent the standard deviation. Energies in hartrees and distance in a_0. $T = 50$ K

	BK (eq. (7))		FT (eq. (6))	
ions				
KE	3.3×10^{-4}	(2×10^{-4})	5×10^{-4}	(2×10^{-4})
PE	-0.1953	(6×10^{-4})	-0.197	(1×10^{-3})
E_{tot}	-0.1950	(8×10^{-4})	-0.196	(1×10^{-3})
electron				
KE_{est}	0.048	(3×10^{-3})	0.0497	(3×10^{-3})
KE	0.048	(9×10^{-3})	0.0496	(8×10^{-3})
PE	-0.085	(2×10^{-3})	-0.0900	(2×10^{-3})
E_{tot}	-0.037	(5×10^{-3})	-0.0410	(5×10^{-3})
NaCl + e				
E_{tot}	-0.232	(5×10^{-3})	-0.2374	(6×10^{-3})
BE	0.034	(5×10^{-3})	0.0382	(6×10^{-3})
R_e	4.66	(4×10^{-2})	4.84	(7×10^{-2})

Table 3

Molecular dynamics calculations for NaCl. Potential energy (PE), kinetic energy (KE), total energy (E_{tot}) and equilibrium distance R_c. Numbers in parentheses represent the standard deviation. Energies in hartrees, R_c in a_0. The experimental data [21] are given for a monomer in low-pressure gas phase ($T \approx 950$ K)

	PE	KE	E_{tot}	R_c
FT (eq. (7))				
$T = 50$ K	-0.1975098 (5×10^{-7})	7.94×10^{-5} (4×10^{-7})	-0.1974304 (9×10^{-7})	4.370 (5×10^{-3})
$T = 950$ K	-0.19750 (1×10^{-5})	0.001500 (6×10^{-6})	-0.19600 (2×10^{-5})	4.38 (2×10^{-2})
BK (eq. (8))				
$T = 50$ K	-0.1992323 (5×10^{-7})	7.99×10^{-5} (4×10^{-7})	-0.1991524 (9×10^{-7})	4.550 (5×10^{-3})
$T = 950$ K	-0.19922 (1×10^{-5})	0.00150 (1×10^{-5})	-0.19772 (2×10^{-5})	4.56 (1.6×10^{-2})
experimental	–	–	-0.2047	4.4598

Using the BK potential we estimate the relative contributions of the various components to the energy of NaCl, with the Born–Mayer interactions accounting for $\approx 90\%$, the charge-polarizability interactions being $\approx 9.5\%$, while the van der Waals interaction contributions contributing $\approx 0.5\%$ to the PE of the ions. For the electron–NaCl interactions, the Coulomb interaction accounts for $\approx 98\%$, and the induced polarization interaction yields $\approx 2\%$ of the potential energy of the electron. The electron kinetic energy consists of a $\approx 95\%$ contribution from the Coulomb terms, 4.5% from the induced dipole interaction and $\approx 0.5\%$ from the free-particle kinetic energy.

In fig. 1b we show a snapshot of the electron chain of pseudo-particles projected on a 2D plane. In fig. 4 we show the radial distribution of the electron bead around the Na$^+$ ion and around the Cl$^-$ ion. It is evident that the electron is mainly localized around the Na$^+$ ion, being strongly repelled from the Cl$^-$ core, as expected. The gyration radius $R_g = 5.23\text{--}5.03 \pm 0.05$ a_0 is larger than the gyration radius for the 3s electron in Na. The radial distribution exhibits a peak at a larger distance from the core of the Na$^+$ ion relative to the 3s electron in Na. $R(\beta\hbar/2) \approx 2.75$ a_0 is much smaller than λ_T. Thus the localization condition is well met, as is evident from fig. 3b, where we show $R(t-t')$ versus time.

We conclude that NaCl$^-$ constitutes a relatively stable molecule, which is in accord with the SCF calculations [22]. The electron distribution possesses cylindrical symmetry with the intermolecular bond direction a the axial symmetry direction. The electron distribution is peaked behind the Na$^+$ and away
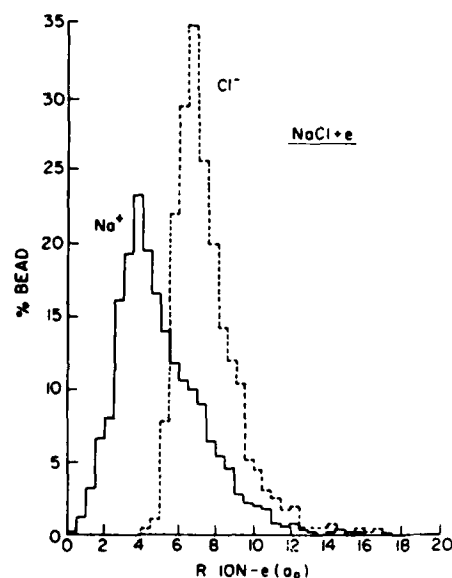

Fig. 4. Histograms of the radial distribution in the e + NaCl system for the electron bead particles around the Na$^+$ core (solid line) and the Cl$^-$ core (dashed line).

from the Cl$^-$ ion, with the distance between the maximum of the electron distribution and the Cl$^-$ being about twice its distance to the Na$^+$ ion. We find that the degree of localization of the electron in the NaCl$^-$ molecule is diminished in comparison with that found in the e–Na$^+$ system. Finally, the bond length in the NaCl$^-$ molecule is large in comparison with that of the neutral NaCl molecule.

We have demonstrated that the QUPID method in

509

conjunction with model potentials constitutes a reliable scheme for the exploration of electron binding to NaCl, and most likely to other alkali halide molecules. This conclusion inspires confidence in the application of this approach to the interesting problem of electron localization in alkali halide clusters which, as we have shown recently, can result in bulk states, surface states, reactive dissociation and cluster isomerization induced by electron attachment [8].

Acknowledgement

References

[1] N.F. Mott and E.A. Davis, in: Electronic processes in non-crystalline materials (Clarendon Press, Oxford, 1971).

[2] E.J. Hart and M. Anbar, eds., The hydrated electron (Wiley, New York, 1970).

[3] J. Jortner and N.R. Kestner, eds., Electron in fluids (Springer, Berlin, 1973).

[4] J. Jortner, Ber. Bunsenges. Physik. Chem. 88 (1984) 188.

[5] M. Parrinello and A. Rahman, J. Chem. Phys. 80 (1984) 86.

[6] J. Bartholomew, R.W. Hall and B.J. Berne, Phys. Rev. B32 (1985) 548.

[7] C.D. Jonah, C. Romero and A. Rahman, Chem. Phys. Letters 123 (1986) 209.

[8] U. Landman, D. Scharf and J. Jortner, Phys. Rev. Letters 54 (1985) 1860.

[9] R.P. Feynman and A.R. Hibbs, Quantum mechanics and path integrals (McGraw-Hill, New York, 1965).

[10] L.S. Schulman, Techniques and applications of path integrals (Wiley, New York, 1981).

[11] D.L. Freeman and J.D. Doll, J. Chem. Phys. 82 (1985) 462.

[12] V. Heine, Solid State Phys. 24 (1970) 1.

[13] J.V. Abarenkov and V. Heine, Phil. Mag. 12 (1965) 529.

[14] R.W. Shaw, Phys. Rev. 174 (1968) 769.

[15] F.G. Fumi and M.P. Tosi, J. Phys. Chem. Solids 25 (1964) 31, 45.

[16] P. Brumer and M. Karplus, J. Chem. Phys. 58 (1973) 3903.

[17] M.F. Herman, E.J. Bruskin and B.J. Berne, J. Chem. Phys. 76 (1982) 5150.

[18] R.C. Weast, ed., Handbook of chemistry and physics, 62nd Ed. (CRC Press, Boca Raton, 1982).

[19] F. Herman and S. Skillman, Atomic structure calculations (Prentice-Hall, Englewood Cliffs, 1963).

[20] A.L. Nichols III, D. Chandler, Y. Singh and D.M. Richardson, J. Chem. Phys. 81 (1984) 5109.

[21] E.J. Mawhorte, M. Fink and J.G. Hartley, J. Chem. Phys. 83 (1985) 4418.

[22] K.D. Jordan and J.J. Wendoloski, Mol. Phys. 35 (1978) 223.

Optical selection studies of electronic relaxation from the S_1 state of jet-cooled anthracene derivatives

Aviv Amirav, Chanan Horwitz, and Joshua Jortner

Sackler Faculty of Exact Sciences, School of Chemistry, Tel Aviv University, 69978 Tel Aviv, Israel

In this paper we explore the energy dependence of the interstate electronic relaxation rates k_{nr} from the S_1 manifold of anthracene and seven of its isotopic and chemical derivatives, which were inferred from quantum yield data. Absolute fluorescence quantum yields Y from groups of rotational states within the electronic origin $S_1(0)$ and from vibrational states were obtained over the excess energy $E_v = 0$–3000 cm^{-1} above $S_1(0)$ by the simultaneous interrogation of the fluorescence excitation spectra and of the absorption spectra in seeded, pulsed, planar supersonic jets of Ar. Additional information was obtained from quantum yield data of van der Waals (vdW) complexes of these molecules with Ar. The fluorescence quantum yields from the $S_1(0)$ of anthracene, 9-cyano-anthracene, and 9,10-dibromoanthracene were found to be independent of the rotational state, providing further evidence for the rotational independence of k_{nr} from a single doorway state. From the Y data of the electronic origins and from the E_v dependence of Y we conclude that intersystem crossing (ISC) dynamics of the S_1 manifold is dominated by the interplay between two classes of nonreactive coupling and/or relaxation: (i) Interstate coupling, involving the superposition of direct $S_1 \rightarrow (T_1)$ ISC together with $S_1 \rightarrow (T_x) \rightarrow (T_1)$ mediated ISC through a sparse or dense (T_x) manifold of a higher triplet state; (ii) Intrastate coupling within the S_1 manifold, which sets in with increasing E_v and which results in intramolecular vibrational energy redistribution (IVR) at high E_v. The dominant role of mediated interstate coupling in ISC dynamics from $S_1(0)$ and from low E_v states was inferred from the inverse deuterium isotope effect on the ISC rates, the extreme sensitivity of k_{nr} of deuterated anthracene to a single H atom substitution, and to level shifts induced by complexing with Ar, as well as from the three-orders-of-magnitude difference between the k_{nr} values from the $S_1(0)$ of 9-bromoanthracene and of 9,10-dibromoanthracene. The onset of the mediated ISC is documented by an abrupt drop of Y in the narrow ($E_v = 617$–805 cm^{-1}) energy range for 9,10-dichloroanthracene and by the oscillatory energy dependence of Y vs E_v and the extreme energy sensitivity of Y in the range $E_v = 157$–800 cm^{-1} of 9,10-dibromoanthracene, which is attributed to near-degeneracies between S_1 states and the mediating (T_x) states. These resonance effects can be drastically modified by dispersive level shifts induced by complexing with Ar. At high excess vibrational energies some universal features of the E_v dependence of k_{nr} are exhibited. These involve a gradual increase of k_{nr} with increasing E_v at medium energies ($E_v = 1000$–1800 cm^{-1}), which correspond to the intermediate level structure for intrastate coupling and a very weak E_v dependence of k_{nr} at high energies ($E_v = 1800$–3000 cm^{-1}), which manifest the effect of statistical intrastate IVR on interstate ISC.

I. INTRODUCTION

The dependence of the interstate radiationless transition rates from photoselected electronically–vibrationally excited states of large collisionless molecules on their excess vibrational energy is central for the elucidation of the processes of intramolecular dynamics. The pioneering work of Schlag and van Weyssenhoff,[1] Parmenter,[2] Rice,[3] Lim,[4] and their colleagues focused on optical selection studies of interstate radiationless transitions in the low-pressure gas phase. The information stemming from bulb experiments was intrinsically limited due to thermal inhomogeneous broadening effects, e.g., rotational broadening and vibrational congestion, which precludes photoselective vibrational excitation. Photoselection of well-characterized rotational–vibrational electronically excited states of large "isolated" molecules can be accomplished in seeded supersonic expansions.[5,6] Basic information on optical selection in interstate

radiationless decay from the S_1 manifold of large molecules has emerged recently from time-resolved spectroscopy in jets.[6–23] Supplementary and complementary information can be obtained from energy-resolved observables, e.g., fluorescence quantum yields. Relative fluorescence quantum yields from different groups of rotational states in the S_1 electronic–vibrational origin of jet-cooled aniline was explored by Amirav et al.[24] Relative fluorescence quantum yields from photoselected vibrational states in the S_1 manifold of jet-cooled large molecules were reported by Levy et al.[25] for transstilbene and by us for 9,10-dichloroanthracene[26] and transstilbene.[26] Subsequently, we have measured[27] the absolute fluorescence quantum yields from the vibrationless electronic origin $S_1(0)$ of several aromatic molecules and their derivatives. Recently, we have extended the experimental methodology to obtain quite extensive information on the excess vibrational energy dependence of the absolute fluorescence quantum yields from photoselect-

ed vibrationally excited states in the S_1 manifold on a variety of jet-cooled large aromatic molecules.[28-31] These studies have provided information on both nonreactive electronic relaxation and on reactive photochemistry in isolated large molecules.

In this paper we focus on optical selection studies of nonradiative electronic relaxation from the S_1 manifold of anthracene and some of its derivatives, i.e., anthracene-D_{10}, anthracene-D_9H, 9-methylanthracene (9MeA), 9-cyanoanthracene (9CNA), 9,10-dichloroanthracene (9,10DCA), 9,10-dibromoanthracene (9,10DBA), and 9-bromoanthracene (9BA), as well as some of their van der Waals (vdW) complexes with Ar. We report on the dependence of the absolute fluorescence quantum yields Y from photoselected vibrational states on the excess vibrational energy E_v above the S_1 electronic origin of these jet-cooled molecules and complexes. The absolute fluorescence quantum yields were determined from the simultaneous interrogation of the fluorescence excitation spectra and the absorption spectra of these molecules in seeded, pulsed, planar, supersonic jets,[24,26-30] using a pulsed xenon lamp and a monochromator and adopting the calibration method previously advanced by us.[27] The refinement of our experimental techniques allows for the accurate determination of absolute fluorescence quantum yields in the range $1-10^{-4}$. Accordingly, our experimental approach can provide information on fast intramolecular relaxation times from photoselected internal states on the ~1 ps time domain. The information emerging from our study of electronic relaxation from the S_1 manifold of jet-cooled anthracene, its derivatives, and some vdW complexes can be summarized as follows:

(1) Mediated intersystem crossing. Electronic relaxation from the S_1 electronic manifold of these molecules proceeds via S_1-T_1 intersystem crossing (ISC), which is mediated by a higher triplet (T_x) state.[32-45] While the occurrence of the $S_1-T_x-(T_1)$ mechanism in condensed phases has been documented previously on the basis of the temperature dependence of ISC, energetic data, and the buildup times of triplet–triplet absorption,[32-45] the present results provide new information on the energetic spread of the T_x states and their role in mediating the radiationless decay of specific vibronic levels in the S_1 manifold of this class of molecules under collisionless conditions.

(2) The onset of mediated intersystem crossing. A "step-like" dependence of the fluorescence quantum yield vs the excess vibrational energy, which is manifested by an abrupt drop of Y in a narrow range of E_v, is exhibited in certain compounds, e.g., 9,10DCA and is attributed to the onset of the mediated intersystem crossing.

(3) The control of electronic relaxation by microscopic solvent effects on the molecular energy levels. The dispersive stabilization of the S_1 state by vdW complexing with rare-gas atoms[47] provides a novel approach for the exploration of the remarkable quantitative modification of ISC dynamics, which is induced by small level shifts of the S_1 levels relative to the mediating T_x states.

(4) Resonance effects. A strong oscillatory dependence of Y vs E_v for 9,10DBA presumably manifests novel resonance effects of the mediating states on intersystem crossing.

A preliminary report of this effect was presented.[48]

(5) The role of vibrational energy redistribution (IVR) on electronic relaxation. Intersystem crossing at high vibrational excitation of the S_1 manifold exhibits a universal trend of weak energy dependence of the lifetimes on E_v, manifesting the consequences of intrastate IVR on interstate electronic relaxation.

II. EXPERIMENTAL

A scheme of the experimental setup is shown in Fig. 1. A pulsed linear nozzle slit (Fig. 2) generated a pulsed planar jet of the large molecule seeded in Ar. The pulsed nozzle triggered a pulsed lamp through a variable delay unit, achieving temporal matching of the light and gas pulses. The light pulse was focused onto the entrance slit of the monochromator and then refocused parallel to the long axis of the linear nozzle. The light was detected both before and after crossing the supersonic expansion and the difference was monitored by a differential amplifier, resulting in the absorption signal which was normalized to the incident intensity. The fluorescence was focused and detected in a perpendicular direction to both the light pulse and the gas pulse propagation directions. All the signals, i.e., the fluorescence excitation, the absorption, and the reference light intensity were simultaneously detected and electronically processed using a triple-gated amplifier, a voltage divider, and a double pen recorder. The absorption and fluorescence spectra, both being normalized to the incident light intensity, were simultaneously recorded. In what follows, the components of the system will be described.

A. Vacuum system

The pumping system consisted of a 4 in. diffusion pump (Varian VHS 4) and two mechanical pumps (Edwards)

PULSED LINEAR NOZZLE
SPECTROPHOTOMETER
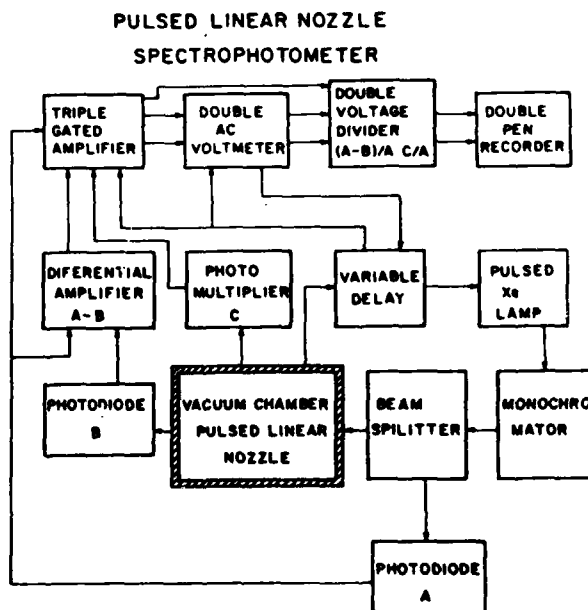

FIG. 1. Experimental setup for the measurement of absorption fluorescence excitation and quantum yields in seeded, pulsed planar supersonic expansions.
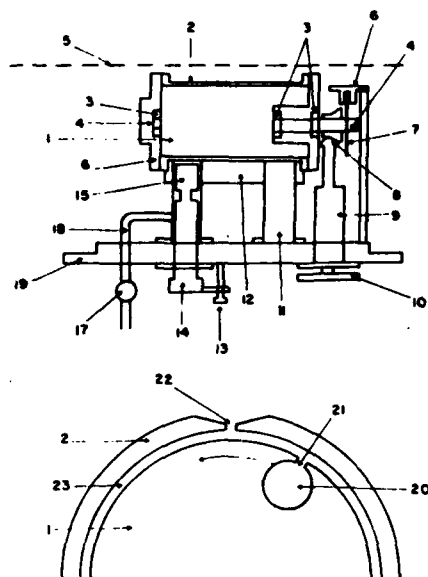
PULSED LINEAR NOZZLE

FIG. 2. A schematic diagram of the pulsed linear nozzle source. (1) rotating cylinder, (2) stator, (3) two flanges with ball bearings, (4) axle, (5) direction of light pulses, (6) optical switch serving for triggering of light pulses, (7) slotted disk, (8) two conical gears, (9) ferrofluid rotatory vacuum feedthrough, (10) motor pulley, (11) mechanical support, (12) heating and cooling block, (13) adjusting screw for sample compartment, (14) sample compartment handle, (15) sample compartment, (16) flange-stator sealing (metal to metal), (17) gas valve, (18) gas tube, (19) mounting flange, (20) gas reservoir, (21) linear slit in the rotor, (22) linear slit in the stator, (23) 25 μ tolerance between stator and rotor (lubricated).

with pumping speeds of 200 ℓ/min and 350 ℓ/min. The vacuum system contained a baffled entrance and exit CaF_2 windows. A quartz lens (51 mm focal length and diameter) served for the collection of the fluorescence light and also acted as a vacuum window. The pulsed nozzle and a liquid N_2 cold trap were located in the two main flanges of the vacuum chamber.

B. Pulsed linear nozzle

The pulsed linear nozzle, which is described in Fig. 2, constitutes a refined version of the linear nozzle developed in this laboratory.[24] This mechanically operated device has a rotating cylinder with a gas mixture reservoir and the gas mixture was expanded through a linear slit. A rotating cylinder (rotor) with a slit was spun inside a fixed stator, which also had a slit. Two linear nozzles were used with slit dimensions of 0.32×90 mm and of 0.22×35 mm. The temporal overlap of the rotor's and stator's slits allows for the expansion of the gas mixture into the vacuum chamber, resulting in the formation of the pulsed planar jet. The rotor was mounted on two flanges with ball bearings and the axle was driven by two conical gears, one of which was mounted on a ferrofluid rotatory vacuum feedthrough. The rotor was rotated by an a.c. motor, which was coupled to the rotor by an O-ring belt connection. The diameter of the rotor slit was 50 mm, with a tolerance of 20–30 μ. The nozzle could be heated

(cooled) using a heating (cooling) block. The sample compartment can be detached and taken out of the evacuated nozzle by swinging the compartment handle, and its temperature could be adjusted by using a screw which could change its distance from the heating block. The nozzle could be operated in the temperature range up to 220 °C. Ar gas in the pressure range $p = 50$–200 Torr that was fed from a valve and a tube through the sample compartment chamber and subsequently passed to the gas reservoir through a groove. The backing pressure was controlled using a needle valve and a manometer (not shown in Fig. 2). A slotted disk and an infrared optical switch (Spectronix 1874) served for the triggering of the pulsed lamp.

The nozzle was operated at a frequency of 5–13 Hz, resulting in 150–350 μs, gas pulses. This pulsed linear nozzle constitutes a reliable device, which was routinely operated for periods exceeding 24 h. The device could be operated for several months before a mechanical failure would be encountered or a lubrication service required.

C. Light source

We have used a short-arc xenon lamp (Osram XBO 75 w/2), which was ignited and simmered at 3–5 A, utilizing Oriel's universal power supply. The simmered lamp was pulsed using a 45 μF capacitor charged to 100–200 V in conjunction with a capacitor charger.[49] This mode of operation results in the increase of the brightness of the lamp by about three orders of magnitude, as compared to the conventionally operated lamp. The intensity of the pulsed simmered lamp measured at the monochromator exit slit at 0.4 Å resolution was 10^{-10} J. The stability of individual pulses (pulse duration 24 μs) was about 1%, and after comparison with the reference signals the noise was found to be better than 0.1% for a single pulse.

D. Optics and detectors

The pulsed light beam was focused with a single 1 in. lens (1 in. focal length) onto the entrance slit of a monochromator. Two monochromators were used:

(1) A 0.3 m McPherson 218 monochromator equipped with a grating of 2400 lines/mm. The spectral resolution attained with slits of 30 μ was 0.4 Å (2.8 cm^{-1} at 3700 Å).

(2) A 0.75 m/spex monochromator equipped with a 2400 lines/mm grating. The spectral resolution was 0.11 Å for 15 μ slits (0.8 cm^{-1} at 3700 Å). The spectral resolution attained at slits of 6 μ (as determined by the splitting of the Hg lines) was 0.06 Å. Typical resolutions routinely used in our work were in the range 0.06–0.6 Å (0.4 cm^{-1} – 4 cm^{-1}).

The light from the monochromator was split by a beam splitter, consisting of a partially mirrored CaF_2 window or a pair of sapphire windows for reference light detection. The beam from the monochromator before passing through the beam splitter was focused using a 1 in. lens (4 in. focal length) parallel to the long axis of the slit nozzle at a distances of $x = 6$–16 mm from the slit. Both the direct and the reference pulsed light beams were detected with vacuum

photodiodes (Hammamatsu R645 or R727). The fluorescence was detected using a photomultiplier (Hammamatsu R269).

E. Electronics and data processing

All the techniques employed in this work were home-made. The reference signal I_0 and the direct transmission signal I were fed to a differential amplifier with adjustable relative gain for zeroing in the absence of absorption. The relative absorption signal $(I_0 - I)$, obtained from the differential amplifier, the fluorescence signal I_F and the reference signal, I_0, were simultaneously processed using a triple-gated amplifier. In order to correct the chromaticity of the beam splitter and to obtain a flat absorption baseline, we have used a double ac voltmeter which is connected with the variable delay unit. This piece of electronics doubled the number of light pulses relative to the number of gas pulses. In this setup the difference signal $(I_0 - I)$ and the fluorescence signal were simultaneously measured by the gate amplifier with a single pulse gating. These signals were sent to the double ac voltmeter which measured the difference between the synchronized and unsynchronized signal pulses. The reference signal I_0 was measured by the gated amplifier and used for normalization using a voltage divider. Such an on-line comparison between I and I_0 was corrected for absorption baseline spectral drifts. The proper timing of the gas pulse and of the light pulse was achieved by using a variable delay unit, which could be operated in the range $10 \mu s$–10 ms.

F. Data recording

The absorption $(I_0 - I)/I_0$ and the normalized fluorescence I_F/I_0 were simultaneously recorded using a double pen recorder. Absorption spectra and fluorescence excitation (LMIF) lamp-induced fluorescence spectra were recorded. Accurate quantum yield data were obtained by recording the fluorescence excitation and the absorption at a fixed wavelength, increasing the time constant to obtain a high precision, while the baseline was recorded with a delay of 10 ms. In addition, quantum yield data were obtained in a narrow spectral range and with a high time constant to correct for the small contribution of dimers to the absorption spectrum and to the fluorescence background.

Absolute quantum yields Y were determined using the calibration scheme previously developed by us,[27] which rests on the simultaneous measurements of relative quantum yields from the electronic origins of a pair of molecules in a binary doped supersonic expansion, and the assignment of a value of $Y = 1$ to fluorescence from the electronic origins of transstilbene and of 9,10DCA.[27] Absolute fluorescence quantum yields in the range $Y = 1 - 10^{-4}$ could be routinely recorded. The uncertainty of the Y data was estimated to be 2% for intense spectra features, while for weak spectral features the accuracy was 10%.

G. Chemicals

All the chemicals used by us were commerically purchased. Care must be taken to ensure the purity of those materials, whose consituent molecules exhibit a low fluorescence quantum yield in the jet. In such a system, a minor amount of an impurity with a high Y will exhibit a spurious fluorescence signal. A typical example for a trace of impurity fluorescence is provided in Fig. 3, where we portray a portion of the fluorescence excitation and the absorption spectra of 9-bromoanthracene, whose electronic origin at 3742 Å is characterized by $Y = 0.0024$. The intense spectral feature in the fluorescence excitation at 3610.2 Å, which is masked by the noise in the absorption spectrum, corresponds to the electronic origin of the anthracene molecule ($Y = 0.67$). The anthracene molecule, which is present as an impurity in 9BA at a concentration of about 1%, provides the dominant spectral feature in the fluorescence excitation spectrum, but is buried within the noise in the absorption spectrum of the low-Y 9BA.

III. RESULTS AND DISCCUSION

A. Rotational structure of the electronic origin

A partial resolution of the rotational contour of the electronic origin of the first spin-allowed $^1S_0 \rightarrow {}^1S_1$ electronic transition of anthracene-H_{10}, anthracene-D_9H, and anthracene-D_{10} could be accomplished under our experimental conditions of 0.5–1 cm^{-1} spectral resolution. Figure 4 shows the characteristic B-type (perpendicular) rotational contours of the three isotopic molecules, obtained by LMIF and absorption spectroscopy. These experimental results are in
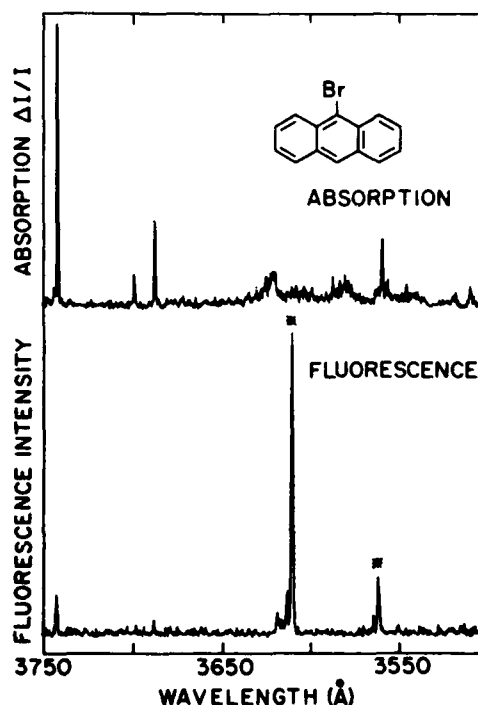

FIG. 3. Absorption spectrum (top curve) and fluorescence excitation spectrum (lower curve) over the range 3750–3550 Å of 9BA in a pulsed planar jet of Ar. Stagnation pressure $p = 110$ Torr and nozzle temperature $T = 140$ °C. Distance from nozzle $X = 10$ mm. The intense feature at 3610 Å in the fluorescence excitation spectrum is due to anthracene impurity.
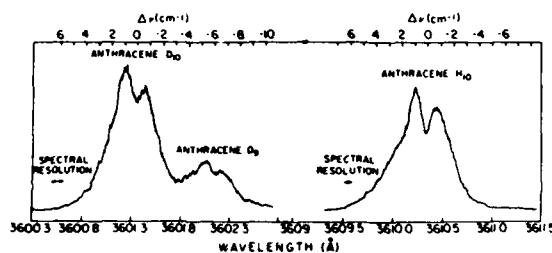
FIG. 4. Fluorescence excitation spectra of the electronic origins of anthracene-H_{10}, anthracene-D_9H, and anthracene-D_{10} in a pulsed planar jet of Ar $p = 100$ Torr, $T = 140$ °C, $X = 10$ mm. The spectral resolution is marked on the figure.

accord with recent LIF jet spectra of anthracene[18] and with the well-established theoretical assignment of this electronic transition to the short axis polarized $^1A_{1g} \rightarrow {}^1B_{2u}$ excitation.[50] An analysis of the rotational contours of anthracene was previously performed,[18] assuming that the rotational constants are invariant upon electronic excitation. We have conducted numerical simulations of the rotational contours of anthracene, accounting for the (small) changes in the rotational constants. The rotational constants for the two combining states (Table I) were calculated using the Ross–McHough recipe.[51] These were derived from the molecular structures of the $^1A_{1g}$ and $^1B_{2u}$ states, being based on the bond-length–bond-order relations using Pariser's wave functions.[50] The ground state rotational constants are close to those inferred by Lambert et al.[18] from structural data. The numerical simulations were conducted using the asymmetric rotor program of Birss and Ramsay.[52] The range of J values was taken from $J = 0$ to $3J$ max, where J max corresponds to the most populated J value at a given temperature. The K values were taken in the range $K = 0$–50. Convolution of the experimental spectral resolution was performed by assigning a width of 0.5 cm^{-1} to each line. Typical results for simulations in the temperature range $T = 2$–40 K are presented in Fig. 5. Regarding the accuracy of the excited-state rotational constants, we have found that at low temperatures, which are of interest to us, small changes ($\sim 1\%$) in A', B', and C' result in negligible changes in the energetic parameters of the low-temperature rotational contours and in quite a marked change in the intensity distribution within the contour (Fig. 6). The experimental data for the intensity ratio between the maxima of the P and R branches favor the values of ΔA, ΔB, and ΔC of Table I over the first-order intelligent guess[18] $\Delta A = \Delta B = \Delta C = 0$. Figure 7 shows the comparison between the experimental LMIF spectrum of the S_1 origin of anthracene-H_{10} and the "best fit" of the simulated spectrum. A typical rotational temperature of this large molecule in the planar jet is $T_R = 20$ K under our ex-
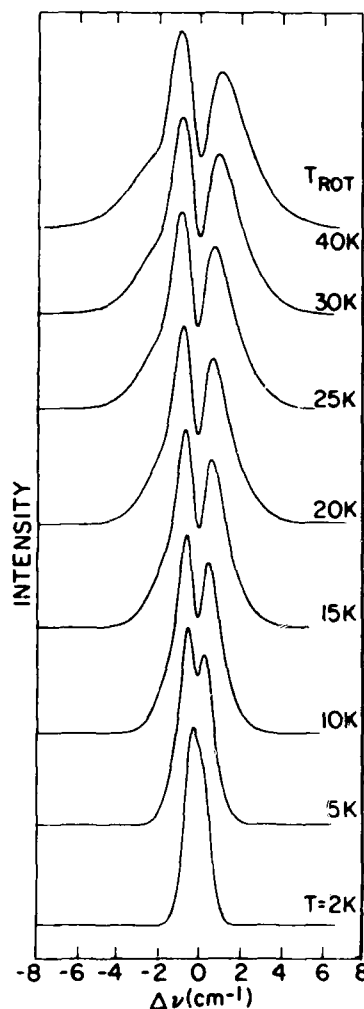

FIG. 5. Numerical simulations of the temperature dependence of the rotational contours for the 0–0 band of anthracene for rotational temperatures $T_{rot} = 2$–40 K. Rotational constants from Table I. Spectral resolution 0.5 cm^{-1}.

perimental conditions. This relatively high rotational temperature is a consequence of the short-interrogation distance $X = 10$ mm from the nozzle, the high relative concentration (up to $\sim 1\%$) of the large molecule in the expansion, and the large cross section (1×4 mm) of the interrogating light beam.

B. Fluorescence quantum yield from the electronic origin

The fluorescence quantum yield for the S_1 electronic origin was found to be independent of the rotational state. Excitation of groups of rotational states within a spectral width of 0.5 cm^{-1} within the low energy P branch (which also contain a contribution from the Q branch) and from the high energy R branch revealed that the absolute quantum yield is independent of the rotational quantum numbers $J'K'$ (Fig. 8). Similar results were obtained for Y from the electronic origin of 9,10DBA ($Y = 0.72$) and of 9CNA
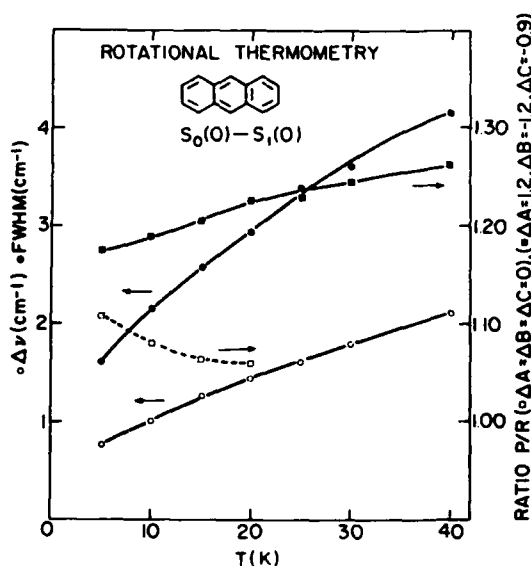
TABLE I. Rotational constants for anthracene (in cm^{-1}).

State	A	B	C
S_0	0.071 70	0.015 12	0.012 49
S_1	0.071 82	0.015 00	0.012 40

FIG. 6. The rotational temperature dependence of the separation (Δv) of the $P(+Q)$ and R branches, the width of the rotational contour at 50% intensity point (FWHM) and the intensity ratio between the maxima of the P and R branches (ratio P/R) for the electronic origin of anthracene. The P/R ratio is very sensitive to the changes in the rotational constants between the two electronic states. $\square$ P/R ratio for $\Delta A = \Delta B = \Delta C = 0$; $\blacksquare$ P/R ratio for the data of Table I, with the values of ΔA, ΔB, and ΔC being given in units of 10^{-4} cm^{-1}.

($Y = 1.0$). The dominant nonradiative decay channel for the $S_1(0)$ electronic origin involves interstate electronic relaxation, which is due to S_1-triplet intersystem crossing (ISC) with the final triplet dissipative channel corresponding to the statistical limit. The invariance of the fluorescence quantum yield to the group of rotational states provides additional evidence that electronic relaxation in the statistical limit is invariant with respect to the rotational state. This result is supported by previous experimental work on the
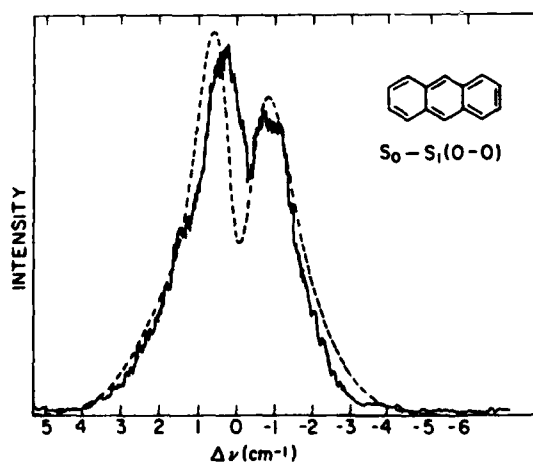

FIG. 7. A comparison between the experimental spectrum of the electronic origin of anthracene in a planar supersonic jet $P = 110$ Torr, $T = 130$ °C, $X = 10$ mm, spectral resolution 0.5 cm^{-1} (solid curve) with the numerical simulation of the rotational contour at $T_{rot} = 20$ K.
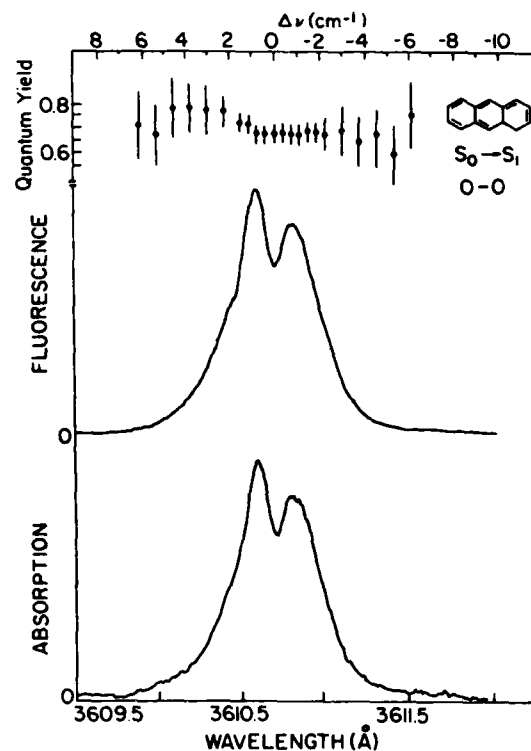

FIG. 8. Absorption spectrum, fluorescence excitation spectrum, and absolute fluorescence quantum yields from the $S_0 \rightarrow S_1$ electronic origin of anthracene. $P = 110$ Torr, $T = 140$ °C, $X = 6$ mm, spectral resolution 0.6 cm^{-1}.

rotational independence of electronic relaxation from the S_1 electronic origin of aniline,[24] of tetracene,[8] and of the rotational state independence of ISC of single rovibronic levels in the S_1 manifold of benzene,[54(c)] and with theoretical calculations.[53] Four remarks regarding the rotational state independence of nonreactive intramolecular radiationless processes are in order:

(1) The rotational independence of the electronic relaxation observed herein pertains to the decay of an "isolated" doorway state, i.e., the electronic origin which is coupled by $J'K'$ independent, that is, spin–orbit interaction V to a "statistical" background manifold. In this case the decay rate $\Delta = 2\pi V^2 \rho$ and the quantum yield $Y = \Gamma_r/(\Gamma_r + \Delta)$, with Γ_r being the radiative width of the doorway state, are independent of $J'K'$.[53]

(2) At higher vibrational energies of the S_1 manifold when Coriolis coupling between S_1 vibrations prevails, the fluorescence quantum yield may be dependent of $J'K'$.[54-56]

(3) In the intermediate level structure, for interstate coupling, where the doorway state is coupled to a sparse background manifold, the quantum yield is $Y \sim \Gamma_r/N\langle\gamma\rangle$, with $\langle\gamma\rangle$ being an (average) decay width of the background states and N is the dilution factor.[29] The breaking of K selection rules for interstate coupling may result in the dependence of N on J', leading to the dependence of the quantum yield on J'. In this case the rotational dependence of the quantum yield originates from the J' dependent dilution of the radiative lifetime.[29]

(4) The intermediate level structure may prevail for either interstate or intrastate coupling with K selective Coriolis coupling between the background states whereupon Y will become rotational state dependent.[57]

The present situation for the decay of S_1 origin corresponds to case (1).

C. Quantum yields from electronic origins of anthracene and some of its isotopic derivatives

A large inverse deuterium isotope effect for electronic relaxation, i.e., intersystem crossing (ISC) from the $S_1(0)$ electronic origin of jet-cooled anthracene-H_{10} and anthracene-D_{10} was inferred from quantum yield data[28] and confirmed by decay lifetime measurements.[19,22] We have measured the absolute fluorescence quantum yields at the $S_1(0)$ electronic origin of anthracene-H_{10}, anthracene-D_9H and anthracene-D_{10}, all of which were interrogated at the dip of the B-type rotational contour. A preliminary report of the Y data between the R and the $P(+Q)$ branches for anthracene-H_{10} and anthracene-D_{10} has been provided.[28] In Table II we present these Y data together with the lifetime, τ, data of Schlag,[23] Lim,[22] and Zewail,[19] which result in the pure radiative lifetime τ_{rad} and the ISC rates k_{nr}. From these results the following is apparent:

(1) The pure radiative lifetimes are invariant with respect to isotopic substitution, as expected.

(2) A very large inverse deuterium isotope effect, i.e., $k_{nr}(D_{10})/k_{nr}(H_{10}) \simeq 15$, is exhibited on the ISC rate from the $S_1(0)$ origin of anthracene-D_{10} relative to that of anthracene-H_{10}.

(3) A dramatic decrease of the ISC rate from the $S_1(0)$ origin, i.e., $k_{nr}(D_9H)/k_{nr}(D_{10}) \simeq 1/7$, is induced by a single H atom substitution.

It has been pointed out[22,28] that the huge inverse deuterium isotope effect on the $S_1 \to T_1$ ISC from the $S_1(0)$ state cannot be accounted for in terms of the conventional arguments based on the role of Franck–Condon factors in interstate coupling, rather this effect was attributed to ISC, which is mediated by a manifold of (T_x^k) triplet vibronic levels and which corresponds to a higher triplet state. The relevant coupling scheme is

$$|S_1\rangle \xrightarrow{V_{so}} \{|T_x^k\rangle\} \xrightarrow{V_{vib}} \{|T_1\rangle\}, \tag{1}$$

where V_{so} and V_{vib} represent spin–orbit and vibronic coupling, respectively. The $\{|T_x^k\rangle\}$ manifold in the vicinity of $S_1(0)$ is assumed to be sparse, whereupon the $|S_1\rangle \to \{|T_x^k\rangle\}$ coupling for all k states correspond to an off-resonant situation. Under these circumstances the nonradiative decay rate of $|S_1\rangle$ is given by the second-order contribution[28]

$$\gamma_{11}(S_1) = \sum_k |V_{so}^{(k)}|^2 \Delta_k / \{[E(S_1) - E(T_x^k)]^2 + (1/2\Delta_k)^2\}, \tag{2}$$

where $V_{so}^{(k)} = \langle S_1|V_{so}|T_x^k\rangle$ represents spin–orbit coupling between the zero-point vibrational level of S_1 and a vibrational level k in the sparse T_x manifold, while $\Delta_k = 2\pi|\langle T_x^k|V_{vib}|T_1\rangle|^2\rho$ is the decay width of the $|T_x^k\rangle$ state due to its internal conversion to the dense statistical $\{|T_1\rangle\}$ manifold. The ISC rate, Eq. (2), contains a cumulative contribution for several mediating states. Both the widths Δ_k and the spin–orbit coupling terms are expected to exhibit a small normal deuterium isotope effect. The large inverse deuterium isotope effect was attributed[22,28] to the sensitivity of the energy defects $|E(S_1) - E(T_x^k)|$, which appear in Eq. (2), on the isotopic substitution. The following implications of this result are apparent:

(A) Inverse deuterium isotope effect on $\gamma_{11}(S_1)$. Since the $\{|T_x^k\rangle\}$ vibrational manifold is more dense in the vicinity of $S_1(0)$ of anthracene-D_{10} than of anthracene-H_{10}, some of the energy defects $|E(S_1(0) - E(T_x^k)|$ are expected to be smaller for deuterated anthracenes, resulting in the enhancement of γ_{11}.

(B) Level structure sensitivity of γ_{11}. The remarkable decrease of k_{nr} by a single H atom substitution (Table II) together with the irregular dependence of k_{nr} on the isotopic substitution (Table II) manifest the crucial role of energetic shifts of the mediating state. A single H atom substitution of perdeuteroanthracene results in the following effects: (i) A change in the level structure of the $\{|T_x^k\rangle\}$ manifold, which results in energetic shifts of the mediating states relative to $S_1(0)$. (ii) An energetic shift of the $S_1(0)$ origin. According-

TABLE II. Quantum yields from the S_1 electronic origins of anthracene and its deuterated derivatives.

Molecule	$(cm^{-1})^a$	Y^b	$\tau_{rad}k_{nr}{}^c$	τ (ns)$^{d-g}$	τ_{rad} (ns)^h	k_{nr} (s^{-1})
Anthracene-H_{10}	0	0.67	0.49	4.0^d 4.4^e	32 ± 3	0.15 × 10^8
Anthracene-D_9H	7	0.49	1.04	17^d	34 ± 3	0.31 × 10^8
Anthracene-D_{10}	69	0.134	6.69	18^d 21.5^e 20^f 18^g	30 ± 3	2.23 × 10^8

^{a}Spectral shifts of electronic origin relative to that of anthracene-H_{10}.
^{b}Absolute quantum yields. Present work.
^{c}Calculated from $\tau_{rad}k_{nr} = (Y^{-1} - 1)$
^{d}Reference 22.
^{e}Reference 19.
^{f}Reference 23.
^{g}A. Amirav and J. Jortner (unpublished).
^{h}Calculated from $\tau_{rad} = Y^{-1}\tau$.

ly, the energetic defects $|E(S_1(0) - E(T_z^k)|$ are modified, resulting in a marked change in γ_{11}. This level structure sensitivity manifests near-resonance effects of the mediating states on the ISC rate. In the rationalization of the surprising inverse deuterium isotope effect and level structure sensitivity of $S_1(0)$ for the isotopic species of anthracene, the role of level shifts originating from effects (i) and (ii) cannot be disentangled. This can be accomplished by the exploration of fluorescence quantum yields from vdW complexes of deuterated anthracenes with Ar, which leaves the $\{|T_z^k\rangle\}$ manifold practically invariant, and result in an energetic shift of the $S_1(0)$ origin relative to the $\{|T_z^k\rangle\}$ states.

D. Erosion of the inverse deuterium isotope effect by complexing with Ar

The formation of vdW molecules consisting of large aromatic molecules bound to rare-gas atoms is well documented.[47] The exploration of microscopic solvation effects on the spectral shifts of aromatic, rare-gas vdW complexes has resulted in extensive information on the energetics of the $S_1(0)$ electronic origin, relative to the vibrationless ground state. For heavy rare-gas atoms, i.e., Ar, Kr, and Xe these red spectral shifts are dominated by dispersive interactions, resulting in the lowering of the energy of the $S_1(0)$ state of the complex relative to that of the bare molecules. A typical example is provided in Fig. 9 which portrays the LMIF spec-
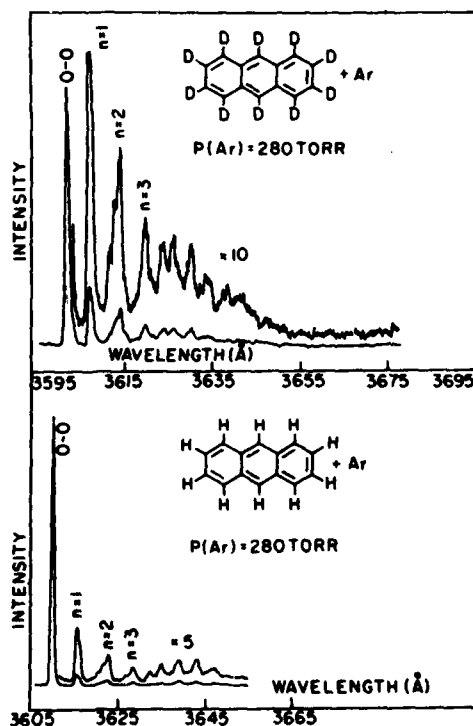
tra of anthracene–Ar_n being in accord with previous data,[58] and of perdeuterated anthracene–Ar_n, which reveal the gradual red shifts of these complexes, with increasing coordination number. The dominating contribution of these red shifts originates from dispersive interactions, which are considerably larger for the $S_1(0)$ state than for the states in the $\{|T_z^k\rangle\}$ manifold. Provided that an anthracene molecule is complexed with an "inert" ligand, which does not modify the intramolecular spin–orbit coupling interaction, one expects a dramatic modification of the mediated nonradiative ISC rate from $S_1(0)$ due to the modification of the energy defects $|E[S_1(0)] - E(T_z^k)|$ in Eq. (2). This expectation is born out by the measurements of the quantum yields from the electronic origins of the vdW complexes of anthracene Ar_1 and perdeuteroanthracene Ar_1, where the Ar atom constitutes nearly an inert ligand, which does not exhibit an external heavy atom effect on ISC. In Fig. 10 we present the absorption and LMIF spectra of the bare isotopic molecules and their complexes with Ar, being labeled as the bare isotopic molecules and their complexes with Ar, which are labeled as $n = 1$. The absolute quantum yields result in the
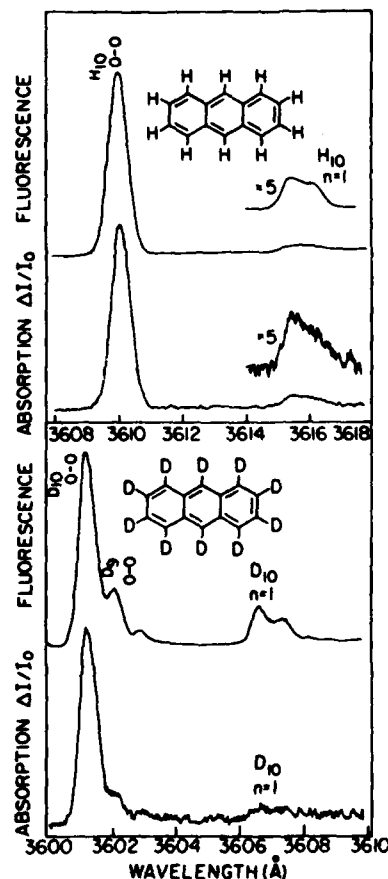
FIG. 9. Fluorescence excitation spectra in the range 3600–3670 Å of anthracene-D_{10} and anthracene-H_{10} at high stagnation pressure of Ar $P = 280$ Torr. The electronic origins of the bare molecules are marked 0–0. The spectral features of the electronic origins of anthracene Ar_n and of anthracene-D_{10} Ar_n are exhibited towards lower energies of the bare molecules electronic origin. The coordination number n of the complexes, assigned on the basis of the order of appearance of these features, is marked on the spectra.

FIG. 10. Absorption spectra and fluorescence excitation spectra of anthracene and anthracene-D_{10} in the spectral range 3600–3610 Å at high stagnation pressure of Ar $P = 220$ Torr for anthracene-H_{10} and $P = 160$ Torr for anthracene-D_{10}. $T = 136$ °C, and $X = 6$ mm. The electronic origins of the bare molecules are marked 0–0. The electronic origins of the anthracene Ar and of anthracene-D_{10} Ar complexes are marked by H_{10} $n = 1$ and D_{10} $n = 1$, respectively.

product of the nonradiative rate and the pure radiative lifetime.

$$k_{nr}\tau_{rad} = Y^{-1} - 1. \tag{3}$$

The values of $k_{nr}\tau_{rad}$ (Table III) reveal a dramatic decrease of the k_{nr} value for perdeuterated anthracene–Ar_1 relative to that of the bare molecule. Furthermore, the values of $k_{nr}\tau_{rad}$ for the Ar complexes of perdeuteroanthracene and of anthracene are practically identical, exhibiting the erosion of the large inverse deuterium isotope effect on ISC due to the modest shift of the $S_1(0)$ state by -43 cm^{-1}. We note in passing that the twofold increase of the values of $k_{nr}\tau_{rad}$ for anthracene. Ar_1 relative to that of bare anthracene can originate from these causes (i) The modification of the pure radiative lifetimes by complexing. The increase of τ_{rad} of anthracene derivatives by the binding of an Ar atom is small $(10\%-20\%)^{59}$ and cannot account for this effect. (ii) A small increase of the spin–orbit coupling by Ar, enhances k_{nr}. (iii) Vibrational predissociation within the (T_x) manifold of the complex, results in the broadening of the mediating states enhancing k_{nr}. For this mechanism to be operative, the energy gap between the $S_1(0)$ origin and of the electronic origin of the (T_x^k) manifold should exceed the binding energy $(D \simeq 700$ cm$^{-1})$ of the argon atom.[72] In any case, the dramatic disappearance of the inverse deuterium isotope effect in anthracene Ar_1 demonstrates the potential of vdW complexing in controlling the mediated interstate dynamics by the induction of the microscopic level shifts by vdW complexing.

E. Quantum yields from the electronic origins of some anthracene derivatives

Conventional wisdom has attributed the electronic relaxation from the S_1 manifold of anthracene and its derivatives to be dominated by ISC.[32-46] Qualitative correlations[60] indicate that the contribution of the $S_1 \rightarrow S_0$ internal conversion to electronic relaxation is minor, with the quantum yield for the populations of the S_0 channel being ~ 0.01. Accordingly, the absolute fluorescence quantum yields from the $S_1(0)$ electronic origins of five anthracene derivatives reported herein (Table IV) provide information on the general patterns of ISC in these compounds. The interstate nonradiative decay of $S_1(0)$ or any other vibronic state of S_1 may proceed by two interstate coupling mechanisms: (i) direct $|S_1\rangle - \{|T_1\rangle\}$ coupling which is characterized by the rate

$$\gamma_1(S_1) = 2\pi |\langle S_1|V_{so}|T_1\rangle|^2 \rho, \tag{4}$$

and (ii) mediated coupling whose rate is determined by the rate $\gamma_{II}(S_1)$, Eq. (2). The total ISC decay rate $\gamma(S_1)$ of a S_1 state is given by the additive contribution

$$\gamma(S_1) = \gamma_1(S_1) + \gamma_{II}(S_1). \tag{5}$$

The unity quantum yield for the $S_1(0)$ electronic origins of 9,10-dichloroanthracene (9,10DCA) and of 9-cyanoanthracene (9CNA) imply that both decay channels (i) and (ii) are closed at this energy. Accordingly, direct $|S_1(0)\rangle - \{|T_1\rangle\}$ coupling is poor in these molecules, which are characterized by a medium spin–orbit coupling, while the electronic origin of the sparse mediating manifold is located above $S_1(0)$, or just slightly below it, so that no mediating vibrational state is in resonance with $S_1(0)$. The reduction of Y below unity for 9-methyl anthracene (9MA) is tentatively attributed to mechanism (ii) with $\gamma = \gamma_{II}$, as is the case for anthracene and its deuterated derivatives, which were alluded to in Secs. III C and III D. Proceeding to the decay characteristics of $S_1(0)$ of molecules containing heavy atoms, which are characterized by a high spin–orbit coupling, i.e., bromoanthracene, we note the large three orders of magnitude difference between the quantum yields and the nonradiative decay rates of $S_1(0)$ of 9,10DBA for which $Y = 0.72$ and of 9BA for which $Y = 2.4 \times 10^{-3}$. The efficient ISC from $S_1(0)$ of 9BA $(Y = 2.4 \times 10^{-3})$ is attributed to the superposition of the direct mechanism (i) and the mediated mechanism (ii), both of which are enhanced by the internal heavy atom effect on the spin–orbit coupling terms $\langle S_1|V_{so}|T_1\rangle$ in Eq. (4) and $\langle S_1|V_{so}|T_x^k\rangle$ in Eq. (2). The operation of mechanism (ii) for 9BA implies that the electronic origin $T_x(0)$ of the mediating triplet is located below $S_1(0)$, ensuring effective resonance coupling between $S_1(0)$ and the mediating manifold. The dominating role of mechanism (ii) in 9BA is reflected by the dramatic differences between the Y values from $S_1(0)$ of 9BA $(Y = 2.4 \times 10^{-3})$ and of 9,10DBA $(Y = 0.72)$. The modest heavy atom effect on ISC from $S_1(0)$ of 9,10DBA is due solely to the enhancement of the direct mechanism (i) by the internal spin–orbit effect, while the mediating channel (ii) is blocked, with $T_x(0)$ being located above $S_1(0)$ in this molecule. Thus, in 9,10DBA $\gamma = \gamma_1$, while in 9BA $\gamma \simeq \gamma_1 + \gamma_{II}$ with $\gamma_{II} \gg \gamma_1$, due to the dominating contribution of near-resonant mediating states to ISC.

Up to this point we were concerned with the ISC from the electronic origins. Under the circumstances, the exclusive nonradiative decay channel involves interstate electronic relaxation. We now proceed to explore the decay characteristics of higher vibrational excitations in the S_1 manifold, which may involve the combination of interstate

TABLE III. Quantum yields for the $S_1(0)$ origin of Ar complexes.

Molecule	Y	$k_{nr}\tau_{rad}$
Anthracene-H_{10}	0.67	0.49
Anthracene-H_{10} Ar	0.49	1.04
Anthracene-D_{10}	0.134	6.69
Anthracene-D_{10} Ar	0.50	1.00

TABLE IV. Quantum yields from the $S_1(0)$ electronic origin of anthracene derivatives.

Molecule	(cm^{-1})[a]	Y[b]	$k_{nr}\tau_{rad}$
9-methylanthracene	26 943	0.58	0.75
9-cyanoanthracene	26 171	1.00	...
9,10-dichloroanthracene	25 950	1.00	...
9,10-dibromoanthracene	25 877	0.72	0.39
9-bromoanthracene	26 724	0.0024	416

[a] Accuracy of peak position ± 3 cm^{-1}.
[b] Accuracy of absolute quantum yields is estimated to be 3%.

electronic relaxation and intrastate vibrational energy redistribution (IVR).

F. Vibrational level structure of anthracene and its derivatives

The vibrational excitations of anthracene in the S_1 manifold, which were obtained by LMIF and absorption spectroscopy (Fig. 11) and the vibrational level structure of anthracene in the S_0 state, which was obtained from dispersed fluorescence resulting from excitation into $S_1(0)$ (Fig. 12), are in excellent agreement with the LIF (laser-induced fluorescence) data of Zewail et al.[18] and with model calculations.[61] The vibrational level structure of the S_1 state for perdeutroanthracene MeA, 9CNA, 9,10DCA, 9,10DBA, and 9BA is displayed in a concise way in Figs. 16–21, and is confronted in Table V with the characteristic vibrations of anthracene. Seven prominent a_g vibrations out of 15 were easily identified in the S_1 state of anthracene-H_{10} which exhibit only a small energetic shift between S_0 and S_1 (Table V). The 387, 1168, 1380, 1420, and 1514 cm^{-1} (or 1554 cm^{-1}) vibrations in the S_1 manifold of anthracene-H_{10} exhibit a weak dependence on chemical substitution in the ninth or the ninth and tenth positions (Table V). The ~750 cm^{-1} a_g vibration in anthracene-H_{10} is expected to be drastically shifted by isotopic and chemical substitution,[61] so that the prominent vibrational feature in the range of 700–800 cm^{-1} for substituted anthracenes corresponds to a progression or combination band(s). The unique assignment of the S_1 vibrational structure above 700 cm^{-1} is complicated by
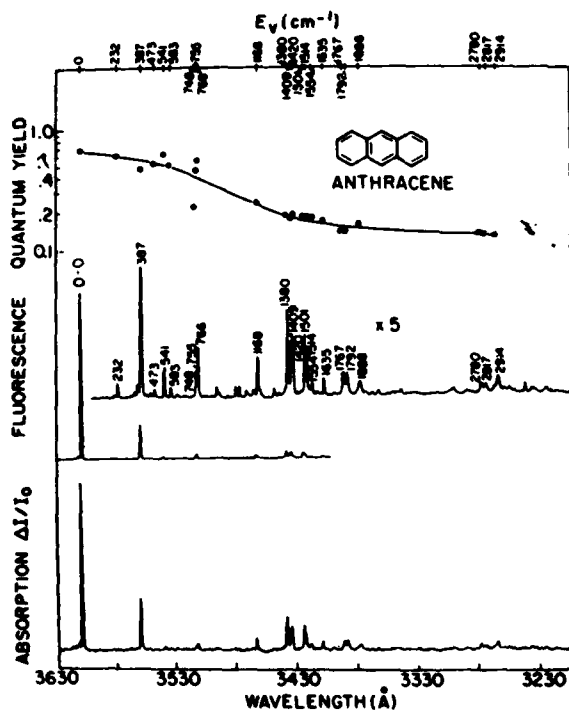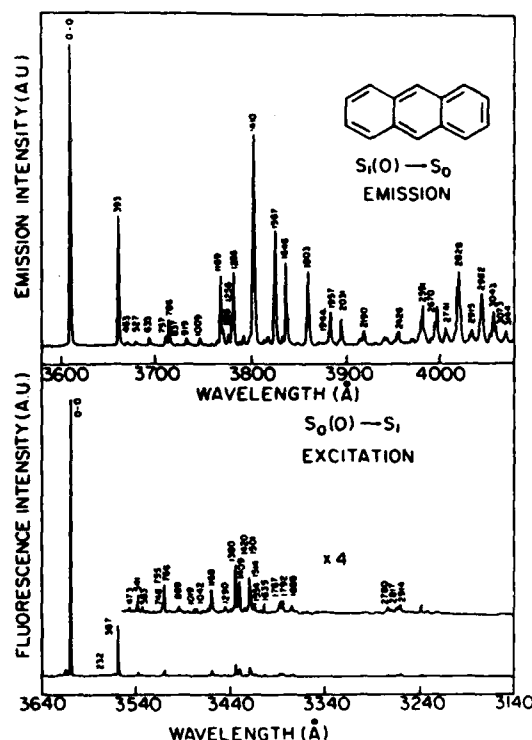
FIG. 12. Fluorescence excitation spectrum of anthracene at spectral resolution of 2 cm^{-1} (lower curve) and energy resolved emission from $S_1(0)$ of anthracene at spectral resolution of 5 cm^{-1} (upper curve). Numbers represent the vibrational excitations above the electronic origins of S_1 or of S_0.

the appearance of Fermi resonances (Table V), which essentially originate from intrastate anharmonic coupling effects and result in splittings of 1–10 cm^{-1}.[8] Typical examples are the 748, 755, and 766 cm^{-1} bunch of states and the 1380, 1409, and 1420 cm^{-1} bunch of states in the S_1 level structure

FIG. 11. Absorption spectrum and fluorescence excitation spectrum of anthracene-H_{10} over the range 3630–3230 Å. $P = 130$ Torr, $T = 138$ °C, and $X = 6$ mm, spectral resolution 3 cm^{-1}. The numbers represent the vibrational excitations above the S_1 electronic origin in cm^{-1}. The points (● ● ●) represent the absolute fluorescence quantum yields. The upper curve was drawn for the sake of visual display.
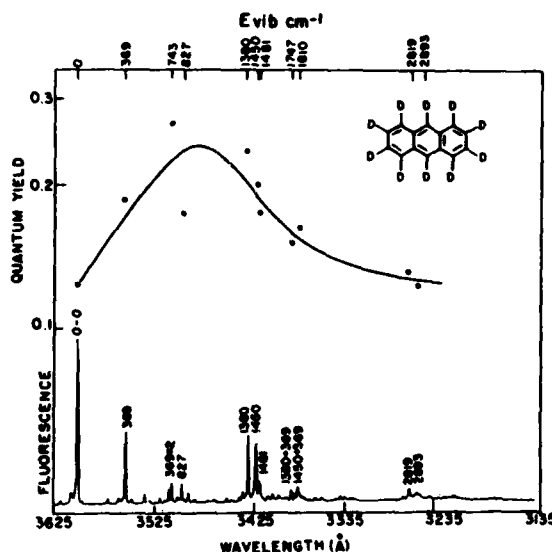
FIG. 13. Fluorescence excitation spectrum and absolute fluorescence quantum yields of anthracene-D_{10} in the spectral range 3625–3235 Å. $P = 110$ Torr, $T = 130$ °C, and $X = 6$ mm. Notation as in Fig. 11.
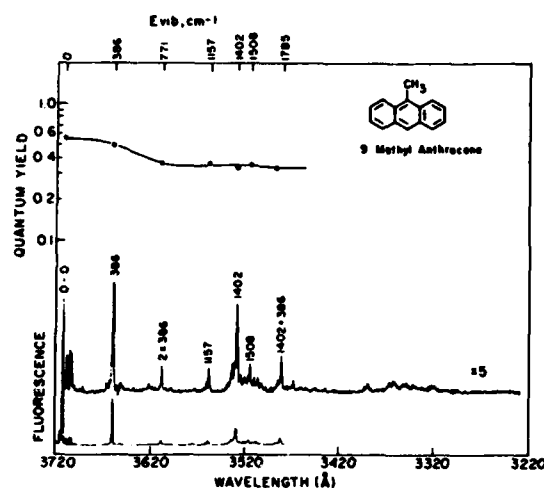
FIG. 14. Fluorescence excitation spectrum and absolute fluorescence quantum yields of 9-methyl anthracene in the spectral range 3720–3220 Å. $P = 110$ Torr, $T = 130$ °C, and $X = 6$ mm. Notation as in Fig. 11.

of anthracene (Fig. 19). These Fermi resonances provide one type of intrastate anharmonic interactions[65–67] which, together with the Coriolis interaction[54–56] are responsible for IVR at higher energies, where the S_1 manifold becomes denser.

Another interesting implication of Fermi resonance effects is the breakdown of the mirror symmetry between the absorption (or LMIF) spectrum and the energy-resolved emission spectra at higher excess vibrational energies. A cursory examination of Figs. 12 and 20 reveals that the

FIG. 16. Absorption spectrum, fluorescence excitation spectrum, and absolute fluorescence quantum yields of 9,10-dicloroanthracene over the spectral range 3865–3375 Å. $P = 100$ Torr, $T = 140$ °C, and $X = 6$ mm. Notation as in Fig. 11.

FIG. 15. Absorption spectrum fluorescence excitation spectrum and absolute fluorescence quantum yields of 9-cyanoanthracene in the spectral range 3828–3328 Å. $P = 110$ Torr, $T = 135$ °C, and $X = 6$ mm. Notation as in Fig. 11.

FIG. 17. Absorption spectrum, fluorescence excitation spectrum, and absolute fluorescence quantum yields 9, 10-dibromoanthracene over the spectral range 3875–3375 Å. $P = 100$ Torr, $T = 145$ °C, and $X = 6$ mm. Notation as in Fig. 11.
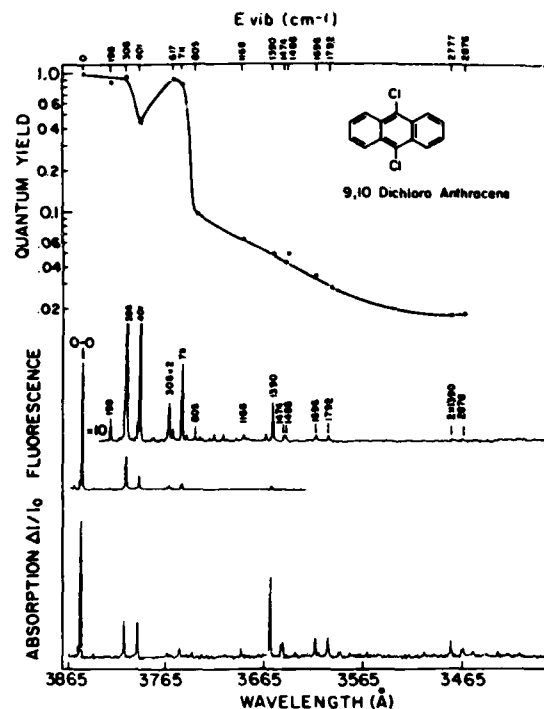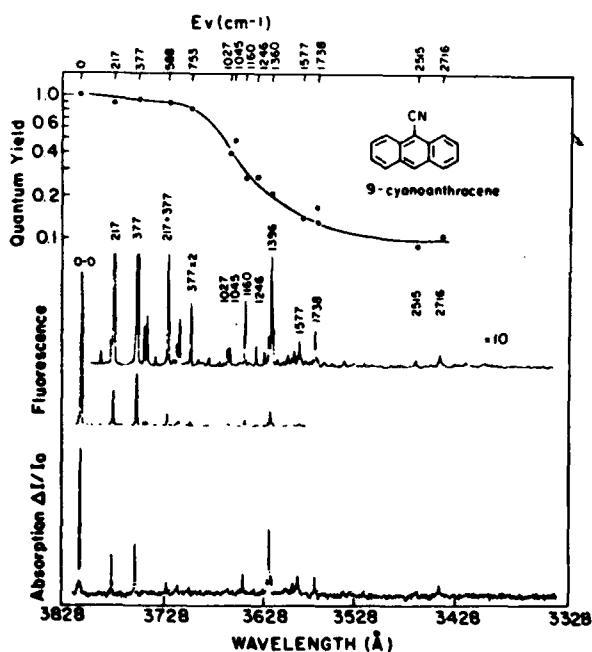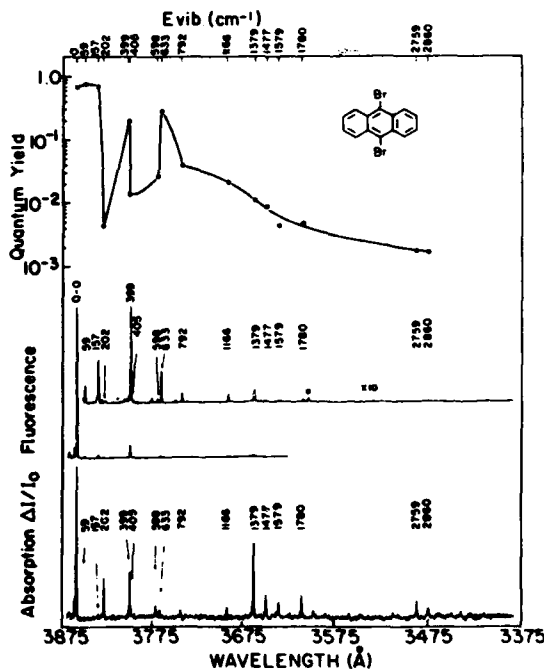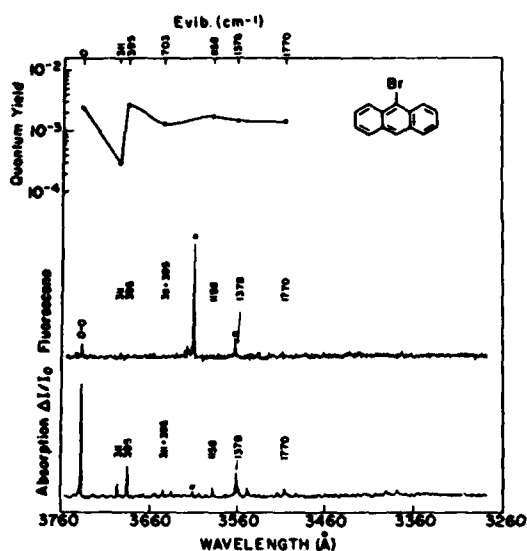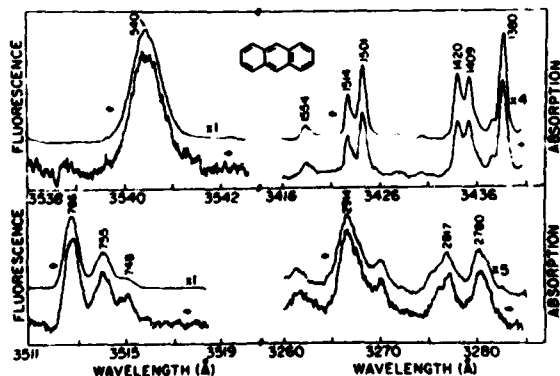
FIG. 18. Absorption spectrum, fluorescence excitation spectrum, and absolute fluorescence quantum yields of 9-bromoanthracene over the spectral region 3760-3260 Å. $P = 100$ Torr, $T = 145$ °C, and $X = 6$ mm. Notation as in Fig. 11. The spectral features in the LMIF spectrum marked by a star (*) correspond to an impurity of anthracene.

$S_0(0) \rightarrow S_1$ absorption (or fluorescence excitation) and the fluorescence from $S_1(0)$ spectra exhibit a mirror image for $E_v \approx 0$–800 cm^{-1}, while for $E_v > 800$ cm^{-1} this mirror symmetry is broken. As is evident from Fig. 12, the 1410 cm^{-1} vibrational excitation in S_0 is replaced by the Fermi resonance mates 1380, 1409, and 1420 cm^{-1} in S_1 of anthracene. Interesting effects of the breakdown of mirror symmetry are exhibited for 9,10DCA (Fig. 20), where the S_1 manifold reveals the prominent 1390 cm^{-1} vibration, which is replaced by the pair 1406 and 1273 cm^{-1} in S_0. The appearance of the 1273 cm^{-1} feature in S_0 may originate from intensity sharing due to Fermi resonance effects, between the 1406 and 1273 cm^{-1} excitations, while the counterpart of the latter excitation is absent in S_1. Alternatively, the 1273 cm^{-1} in S_0 of 9,10DCA may originate from a vibration which suffers a large frequency change between the two elec-

FIG. 19. Some details of the absorption and fluorescence excitation spectra of anthracene. Experimental conditions and notation as in Fig. 11.

tronic states. Another manifestation of the breakdown of the mirror symmetry pertains to the intensity alternation between the absorption and the emission spectra. As is evident from Fig. 12, the relative peak intensity of the 1410 cm^{-1} vibrational excitation in S_0 is considerably higher than the sum of the relative intensities, which are corrected for the quantum yield, of the 1380, 1409 cm^{-1} manifold in S_1. Similarly, in the spectrum of 9,10DCA (Fig. 20), the 1390 cm^{-1} vibration in S_1 is more intense than the corresponding 1406 cm^{-1} in S_0. A mirror symmetry breakdown between absorption and fluorescence can be attributed to the following effects: (1) interference between vibronically induced and allowed transition moments,[68,69] (ii) normal coordinate rotation in S_1,[70,71] and (iii) Fermi resonance anharmonic mixing. Effect (i) is expected to be significant only for symmetric levels of a moderately weak electronic transition, being of minor importance for the strongly allowed $S_0 \rightarrow S_1$ transition of anthracene and its derivatives. Nothing is presently known regarding the Duschinsky rotation[70] [effect (ii)] in the S_1 manifold, which may modify the vibronic intensities of the $S_1(0) \rightarrow S_1$ transition but not the $S_1(0) \rightarrow S_0$ emission spectrum.[71] The splitting of the higher levels in S_1, e.g., the appearance of the 1380, 1409, and 1420 cm^{-1} manifold in the S_1 state of anthracene (Fig. 12) points towards the significant role of Fermi resonance effects in the mirror symmetry breakdown.

Of some interest are the low frequency S_1 vibrations of substituted anthracene, which involve the motion of the substituents. The very low frequencies (31 and 54 cm^{-1}) exhibited for 9MeA correspond to the hindered rotation of the CH_3 group.[62] The 306 cm^{-1} vibration of 9,10DCA involves the motion of the Cl atoms in view of the marked Cl isotope effect on this frequency,[63] while the 202 cm^{-1} vibration of 9,10DBA may correspond to the analogous vibration involving the Br atoms. Another mode in this category involves the 311 cm^{-1} vibration of 9BA, which corresponds to the motion of the Br atom in this compound.

G. Nonradiative decay rates of anthracene and excess vibrational energy dependence of pure radiative lifetimes

The dependence of the fluorescence quantum yields from photoselected vibrational excitations in the S_1 manifold of anthracene is portrayed in Fig. 11. Our quantum yield data were combined with the lifetime τ data of Zewail et al.[19] to provide the dependence of the nonradiative decay rates $k_{nr} = (1 - Y)/\tau$ and the pure radiative lifetimes $\tau_{rad} = \tau/Y$ over the excess vibrational energy range $E_v = 0$–3300 cm^{-1} above the $S_1(0)$ origin (Fig. 21). The pure radiative lifetime of the $S_1(a_g)$ states in the low-energy domain ($E_v = 0$–800 cm^{-1}) are practically independent of E_v, falling in the range $\tau_{rad} = 33$–38 ns as expected for a symmetry-allowed transition. Notable exceptions from this rule involve the weak 232 ($\tau_{rad} = 47$ ns),the 540 ($\tau_{rad} = 57$ ns), and the 748 cm^{-1} ($\tau_{rad} = 50$ ns) vibrational features, whose pure radiative lifetimes exceed by about 50% the τ_{rad} values for the electronic origin and the low-lying $S_1(a_g)$ states (Fig. 22). These weak "abnormal" spectral features were tentatively
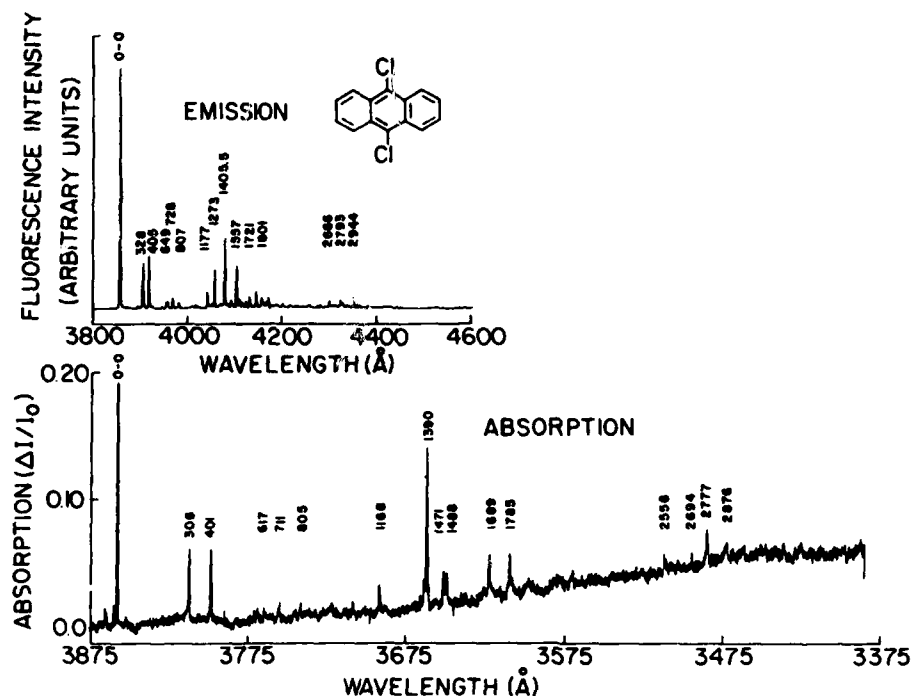
FIG. 20. Absorption spectrum at spectral resolution of 4 cm^{-1} (lower trace) and energy resolved emission from $S_1(0)$ at spectral resolution of 7 cm^{-1} (upper trace) of 9,10-dichloroanthracene. The baseline shift of the absorption spectrum is not genuine and is corrected electronically (see Sec. II) in Fig. 16.

attributed to vibronically induced transitions. Nonresonant vibronic coupling effects originating from Duschinsky rotation of the excited-state normal coordinates may result in the reduction of the transition moment for emission from a nontotally symmetric vibronic state,[70,71] resulting in the lengthening of τ_{rad}. In the higher energy domain ($E_v = 1100–2800$ cm^{-1}) the τ_{rad} values are slightly higher than the radiative lifetimes for the $S_1(a_g)$ states in the low energy region, spanning the range 38–45 ns. Vibronic coupling effects may be operative for the "background" S_t states in the high energy domain, which becomes populated by IVR[54–56] and which becomes active in $S_1 \to S_0$ emisison, resulting in the increase

of τ_{rad} and are of interest. However, the overall nearly constant values of τ_{rad} over a broad E_v range (Fig. 22) imply that the k_{nr}, τ_{rad} data inferred from our experimental Y values can be used to extract estimates of the vibrational energy dependence of k_{nr}, which are reliable within 15%, or so. The quantum yield data for the variety of anthracene derivatives (Figs. 16–21) provide a wealth of semiquantitative information on intramolecular dynamics.

H. General trends of the excess vibrational energy dependence of k_{nr}

The excess vibrational energy dependence of the nonradiative rates from the S_1 manifold of anthracene (Fig. 21) exhibit three energy domains:

(A) The low energy region $E_v < 800$ cm^{-1} where irregular variation of k_{nr} values is revealed, exhibiting mode specificity of the electronic relaxation rates.

(B) The intermediate energy region $800 < E < 1800$ cm^{-1}, where k_{nr} increases practically monotonically with increasing E_v.

(C) The high energy domain $E_v > 1800$ cm^{-1} where k_{nr} exhibits a weak dependence on the excess vibrational energy.

An examination of the E_v dependence of the quantum yields for anthracene (Figs. 11 and 21) perdeuteroanthracene (Fig. 13), 9MeA (Fig. 14), and 9CNA (Fig. 15) reveals similar characteristics. In particular, it should be noted that regions (B) and (C) seem to be exhibited in all these molecules. These universal characteristics of the interstate electronic relaxation in regions (B) and (C) of large mole-
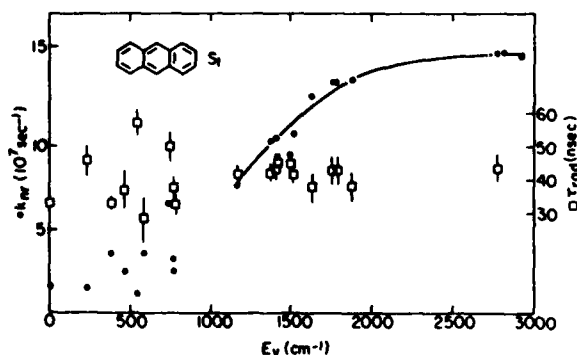

FIG. 21. The dependence of the nonradiative decay rates k_{nr} and of the pure radiative lifetimes τ_{rad} of anthracene on the excess vibrational energy above the $S_1(0)$ electronic origin.

TABLE V. Vibrational level structure of anthracene and some of its derivatives.[a]

Anthracene-H_{10}	Anthracene-D_{10}[c]	9MeA	9CNA	9,10DCA	9,10DBA	9BA
232(S_0)		31,54,68[d]	217[e]	198 306[f]	59 157 202[g]	 311
387(S_1), 393(S_0) [369 (a_g)]	369 [361 (a_g)]	386	377	401	399 405 [2×202]	395
473(S_1), 463(S_0) 541(S_1), 527(S_0) [517 (b_{3g})] 583(S_1), 633(S_0)					598 [202 + 399] 633	
748(S_1), 755(S_1), 766(S_1) 757(S_0), 783(S_0) [735(A_g)] + 2×387 + FRS[b]	743 [2×369]	711 [2×386]	753 [2×377]	710 [2×306][a]	792 [2×395]	703 [33 + 395]
1168(S_1), 1169(S_0) [1169(a_g)]	827 846(a_g)	1157	1160	1168	1166	1158
1266(S_0) [1240(a_g)]			1246			
1380(S_1), 1410(S_0) [1398(a_g)] + FRS	1380 [1347(a_g)]	1402	1396	1390	1379	1378
1409(S_1), 1420(S_1)	1450			1474	1477	
1514(S_1), 1567(S_0) [1557(a_g)]	1481	1508		1488		
1554(S_1)			1577		1579	

[a] All energies are given relative to the electronic origin of the molecule (in cm^{-1}).

[b] For anthracene-H_{10} we present the energies of the S_1 manifold [marked (S_1)] and of the S_0 manifold [marked (S_0)]. For all other compounds the energies of the S_1 manifold is presented.

[c] Calculated a_g (allowed) and b_{3g} (vibronically induced) vibrational frequencies for the S_0 manifold, which were taken from the work of Califano et al. [Ref. 61(a)] and of Ohno [Ref. 61(b)], are marked [(a_g)] and [(b_{3g})]. FRS denotes Fermi resonances.

[d] The low frequencies for the hindered rotation of the Me group.

[e] Low frequency motion of the CN group.

[f] Motion of Cl groups.

[g] Motion of Br group(s).

[h] For vibrational energies exceeding 700 cm^{-1}, Fermi resonance effects make vibrational assignment uncertain.

cules is related to the effects of intrastate intramolecular vibrational energy redistribution (IVR).

The manifestations of intrastate IVR can be inferred from the appearance of Fermi resonances in the $S_0 \to S_1$ absorption (or LIF) spectra,[9,18] the splitting and broadening of the energy-resolved $S_1 \to S_0$ emission[18] and the exhibition of quantum beats in the simultaneous time-resolved and energy-resolved decay.[66-68] The study of Felker and Zewail on IVR in the S_1 manifold of anthracene[66-68] indicates that region (B) corresponds to the intermediate level structure for intrastate mixing, while region (C) corresponds to the statistical limit for IVR. Regarding the manifestations of IVR on electronic relaxation it has already been proposed[8,64] that the features of range (C) originate from efficient IVR in the S_1 manifold, i.e., the statistical limit for IVR which affects the dynamics of the mediated $S_1 \to T$ crossing. We assert that range (B) corresponds to the intermediate level structure of IVR within the S_1 manifold, which results from anharmonic or/and Coriolis interactions. It has been suggested[66-69] that the anharmonic interactions provide a dominating contribution to the intrastate coupling. Recent studies on rotational state dependence of the time-resolved decay and of fluores-

cence quantum yield from vibronic states in range (B) of 9CNA demonstrate the significant role of Coriolis interactions.[55,56,64] From these considerations the following picture emerges of intramolecular dynamics in the S_1 manifold of these substituted anthracenes. Range (A) corresponds to the sparse level structure in S_1, where intrastate coupling does not prevail and each individual S_1 level may undergo (direct or mediated) ISC to T_1. In range (B) intrastate interaction couple a S_1 doorway state, which carries oscillator strength from the ground state origin $S_0(0)$ with background S_1 states, which do not carry oscillator strength from $S_0(0)$. The scrambled S_1 manifold exhibits a mediated ISC to the statistical T manifold. The major cause for the decrease of Y with increasing E_v in range (B) is attributed to the difference in the nonradiative decay rates of the doorway state(s) and of the background states. On the basis of the experimental data, we assert that the nonradiative ISC rates of the background S_1 states exceed that of the S_1 doorway states. This is reasonable, as different symmetries of these levels will affect the Franck–Condon factors which determine ISC. Range (C) corresponds to the statistical limit of IVR, where the S_1 doorway states decay nonradiatively to
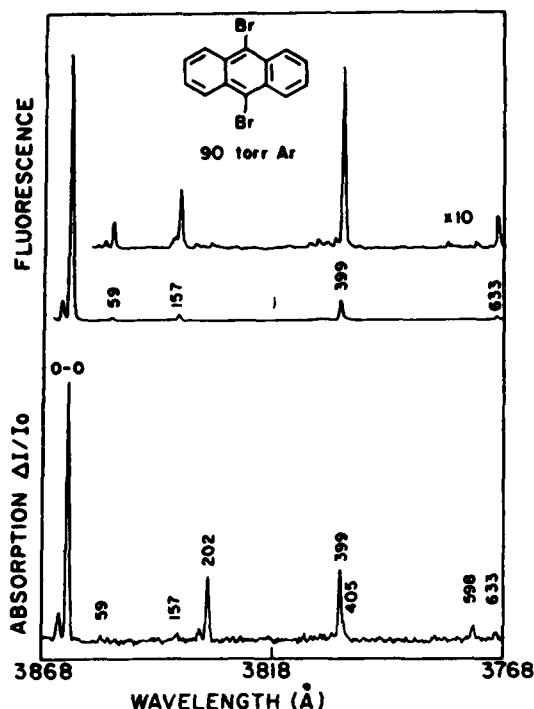
FIG. 22. Details of the absorption (lower trace) and fluorescence excitation (upper trace) spectra of 9,10-dibromoanthracene in the range 3868–3768 Å. Note the huge drop between the fluorescence quantum yield at 202 cm^{-1} relative to 0–0 and 157 cm^{-1}.

dense manifold of background S_1 states, which in turn decay to the T manifold. The interstate dynamics, which is manifested by the fluorescence quantum yield, is then governed by the decay rates of the S_1 background states.

The existence of domains (B) and (C) seems to be universal[64] and was observed in the S_1 manifold of many other large molecules, e.g., tetracene,[8] pentacene,[10] perylene,[31] fluorene,[31] and carbazole.[31] This universality inspires confidence in the admittedly qualitative picture, which rests on the coupling between intrastate IVR and interstate electronic relaxation. Regarding the interstate coupling we have already noted that the dynamics of electronic origins cannot be described in terms of the simple-minded picture for direct $S_1 - (T_1)$ coupling, and mediated coupling has to be invoked. These mediating coupling effects are manifested in the E_v dependence of Y of 9,10DCA and 9,10DBA, which will now be considered.

I. Resonance effects in the E_v dependence of ISC dynamics

We have seen in Sec. III E that for the electronic origins of 9,10DCA the ISC is blocked while the electronic origin of 9,10DBA is practically immune with respect to ISC, exhibiting modest electronic relaxation due to direct ISC. As these molecules are characterized by medium (for 9,10DCA) and high (for 9,10DBA) intramolecular spin–orbit coupling, we expect that the onset of mediated ISC will be manifested by a large abrupt drop of Y with increasing E_v. This expectation is borne out by the E_v dependence of Y for 9,10DCA, where

the fluorescence quantum yield reveals a dip at 401 cm^{-1} and drops by a numerical factor of 9 in the energy domain between 617 and 805 cm^{-1} and retains a low value at higher E_v (Fig. 16). This pattern is attributed to the onset of mediated ISC at $E_v > 401$ cm^{-1} with the 401 cm^{-1} state being already coupled to the $\{|T_x^k\}$ manifold, while efficient coupling with the mediating $\{T_x^k\}$ manifold sets in at the energy domain 711–805 cm^{-1}. A more interesting and detailed manifestation of the onset of mediated coupling at finite E_v is exhibited in 9,10DBA. In Figs. 22 and 23 we present the low-energy LMIF and absorption spectra of 9,10DBA, which exhibit clearly the high value of Y at the origin and at the 157 and 399 cm^{-1} vibration with the huge decrease of Y at 202 (Fig. 22) and at 405 cm^{-1} (Fig. 23) vibrations. It is extremely interesting to note that a small shift of the S_1 vibrational energy by 6 cm^{-1} from 399 to 405 cm^{-1} results in a twentyfold decrease in Y, while a shift of 35 cm^{-1} from 598 to 633 cm^{-1} leads to a thirtyfold increase of Y. It is also interesting to note that the three vibrational excitations of 202, 405 (2×202), and 598 cm^{-1} ($202 + 399$), which exhibit low Y value for 9,10DBA, involve the Br atom vibrations, pointing towards mode specificity in the $S_1 - \{T_x^k\}$ coupling. The three marked minima in the oscillatory energy dependence of Y vs E_v can be accounted for in terms of near resonances between the following pairs of levels: (i) $T_x(0)$ with S_1 (202 cm^{-1}), (ii) $T_x(0) + 202$ cm^{-1} with S_1 (405 cm^{-1}), and (iii) $T_x(0) + 399$ cm^{-1} with S_1 (598 cm^{-1}). The near-resonant interaction between the portions of the S_1 and $\{T_x\}$ manifolds will considerably enhance the interstate coupling of these specific S_1 levels, while other states in the
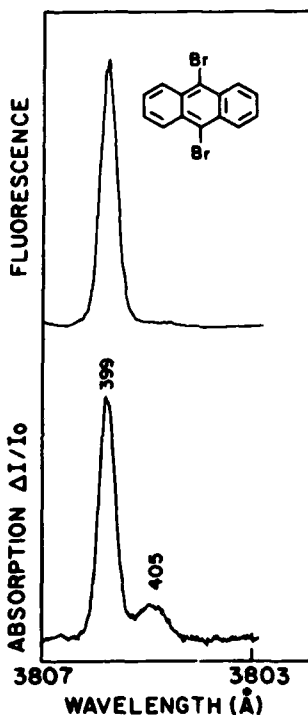

FIG. 23. Details of the absorption and fluorescence excitation spectra of 9,10-dibromoanthracene in the range 3807–3803 Å. Note the dramatic difference in the fluorescence quantum yield between 399 and 405 cm^{-1}.

S_1 manifold in this energy domain are not effectively coupled to the mediating states. The remarkable oscillatory energy dependence of Y together with the energetic sensitivity of the ISC rates (Fig. 17) is attributed to accidental near degeneracies between the S_1 doorway state(s) in the range 202–800 cm^{-1} and the mediating states in the $\{T_x^k\}$ manifold. According to our picture the details of the $S_1 - \{T_x\}$ energetics will determine the quantitative details of the ISC rates. The physical picture based on resonance effects is extremely attractive. Further experimental confirmation of the role of $S_1 - \{T_x\}$ resonance effects was obtained from the study of the implications of level shifts of the 202 cm^{-1} vibration induced by complexing and by isotopic analysis of 9,10DBA.

We have studied the fluorescence quantum yields of 9,10DBA Ar complexes at low vibrational excitations. In Fig. 24 we present the absorption and the LMIF spectra of 9,10DBA expanded in Ar at several stagnation pressures p of the diluent. Several hot bands of 9,10DBA are suppressed with increasing p, e.g., the 146 cm^{-1} features (Fig. 24). In addition to the bare molecules 157 and 202 cm^{-1} vibrations

a new feature appears at 151 cm^{-1}. The relative intensity of this 151 cm^{-1} new feature strongly increases with increasing stagnation pressure. Accordingly, the 151 cm^{-1} feature is attributed to a vibrational excitation of the 9,10DBA Ar$_1$ complex. The spectral shift of the electronic origin of 9,10DBA Ar$_1$ relative to $S_1(0)$ of 9,10DBA was found to be -50 ± 2 cm^{-1}. A similar shift is expected for intramolecular vibrational excitations of 9,10DBA Ar$_1$. Thus the 151 cm^{-1} excitation is assigned to the 202 cm^{-1} intramolecular vibrational excitation of the 9,10DBA Ar$_1$ complex. The red spectral shift is attributed to dispersive stabilization[72] of S_1 (202 cm^{-1}) relative to $S_0(0)$. On the other hand, the stabilization of the mediating (T_x^k) manifold by dispersive interactions is smaller than that of S_1. We thus expect that the energy defect(s) $|E(S_1(202) - E(T_x)|$ which determine the mediated ISC rate according to Eq. (2), will be grossly modified by Ar complexing. While in the bare molecule near-resonant interaction between S_1 (202 cm^{-1}) and some (T_x) levels prevails, the dispersive level shift of S_1 (202 cm^{-1}) will destroy the near accidental degeneracy resulting in a dramatic enhancement of Y from the S_1 (202 cm^{-1}) level of the Ar complex relative to that of the bare molecules. In Table VI we present the quantum yield data for the low vibrational levels of 9,10DBA Ar. The two orders of magnitude increase of Y for the 202 cm^{-1} vibration in the complex is attributed to the energetic "liberation" of this level from near-resonant coupling, which is induced by complexing. Alternative interpretations of the dramatic enhancement of Y for this vibrational excitation should be considered. One possibility involves vibrational predissociation of the 9,10DBA Ar complex. However, from extensive model calculations and experimental data[72] for the dissociation energies of large vdW complexes it is apparent that the dissociation energy of the 9,10DBA Ar complex should be 500–600 cm^{-1} (Ref. 72) so that the reactive vibrational predissociation channel is closed at 202 cm^{-1}. Another mechanism for the intramolecular dissipation of the intramolecular vibrational energy may involve nonreactive IVR between the intramolecular 202 cm^{-1} vibration and the low-frequency molecule-Ar vibration within the complex. This process, which cannot be excluded at present, will eliminate the near-resonant $|E(S_1(202) - E(T_x)|$ coupling due to dynamic effects.

Level shifts of the S_1 (202 cm^{-1}) vibrational excitation relative to the $\{T_x\}$ manifold in 9,10DBA can be induced by isotopic substitution of the Br atom. In Fig. 25 we portray an interesting energy dependence of the quantum yield within the contour of the 202 cm^{-1} excitation, which reveals a drop

FIG. 24. Absorption spectra (left-hand side curves) and fluorescence excitation spectra (right-hand side curves) of 9,10 dibromoanthracene at several stagnation pressures of Ar, which are marked on the spectra. All the spectra reveal the 157 cm^{-1} and the 202 cm^{-1} features, which correspond to S_1 vibrational excitation of the bare molecules. At low stagnation pressures $P = 56$ Torr and $P = 88$ Torr hot sequence bands of the bare molecules appear, the most prominent being the 146 cm^{-1} feature, which is marked $H.B.$ The $H.B.$ disappears at higher P. At $P = 132$ Torr and $P = 150$ Torr a new spectral feature appears at 151 cm^{-1} which is attributed to a 9,10DBA, Ar van der Waals complex.

TABLE VI. Fluorescence quantum yields from 9,10DBA and 9,10DBA Ar.

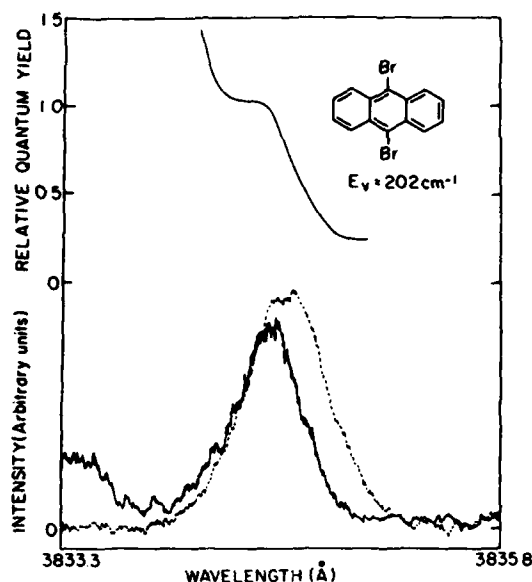| Energy[a] (cm^{-1})	9,10DBA	9,10DBA Ar
0	0.72	0.65
202	0.005	0.60

[a] Relative to electronic origin.

FIG. 25. Absorption spectrum (dashed lower curve), fluorescence excitation spectrum (solid lower curve), and relative fluorescence quantum yield (upper curve) across the (unresolved) contour of the 202 cm^{-1} S_1 excitation of 9,10-dibromoanthracene.

of Y at lower energies. The 202 cm^{-1} vibration of 9,10DBA, which involves the motion of the Br atoms, is expected to exhibit a marked Br isotope effect in an analogy to the 306 cm^{-1} vibration of 9,10DCA.[63] The 202 cm^{-1} contour of 9,10DBA consists of a superposition of the rotational contours of Br^{79}Br^{79}, Br^{79}Br^{81}, and Br^{81}Br^{81} compounds with the relative shifts of 0.7 and 1.3 cm^{-1}. In contrast to the S_1 (202 cm^{-1}) excitation, the $\{T_x\}$ manifold does not necessarily involve Br atom vibrational motion and is not markedly affected by isotopic substitution. Accordingly, the $|E(S_1(202)) - E(T_x)|$ energy defects are modified by the Br isotopic substitution, with small energy shifts resulting in a dramatic one order of magnitude change of the mediated ISC rate.

We have attributed the remarkable oscillatory dependence of Y vs E_v in 9,10DBA to near-resonant effects between some vibrational excitation of S_1 and the $\{T_x\}$ manifold. This mechanism is consistent with the manifestation of the energetic level shifts of S_1 induced by intermolecular complexing or by intramolecular isotopic substitution. A marked oscillatory dependence of Y vs E_v is also exhibited in the low E_v domain of 9BA (Fig. 18), where at $E_v = 311$ cm^{-1} Y drops by about one order of magnitude. The extremely low Y values for 9BA imply that the mediating mechanism is operative already for $S_1(0)$ and for all vibrational excitations of S_1. Accordingly, the drop of Y for S_1 (311 cm^{-1}) for 9DBA cannot be attributed to near-resonant effects with the $\{T_x\}$ manifold. The 311 cm^{-1} of 9BA involves the motion of the Br atom and the surprising reduction of Y for this state may originate from mode specificity in the $S_1 - \{T_x\}$ coupling. An attractive possibility exists that the resonances in Y observed both in 9,10DBA and 9BA are partially due to an enhanced coupling strength of those vi-

brational states involving bromine atoms motion with the mediating $\{T_x^k\}$ manifold. The nature of mode specificity in mediated ISC deserves a further study.

J. Coupling between IVR and mediated ISC

The intramolecular dynamics in the S_1 manifold of anthracene and its derivatives is dominated by the interplay between two classes of intramolecular interaction:

(i) Intrastate coupling involving anharmonic and/or Coriolis coupling which does not prevail for $S_1(0)$ but sets in with increasing E_v.

(ii) Interstate coupling involves two types: (a) very weak direct spin–orbit coupling which prevails only when the intramolecular spin–orbit interaction is appreciable, i.e., 9,10DBA; (b) mediated spin–orbit and vibronic coupling Eq. (1), which dominates the ISC. The dominant role of mediated coupling in this class of compounds emerging from our data is evident from the inverse deuterium isotope effect on ISC at the origin, the sensitivity of k_{nr} of $S_1(0)$ to isotopic substitution, the erosion of the inverse isotope effect by Ar complexing, the stepwise onset of ISC in 9,10DCA, the resonance effects on ISC in 9,10DBA and their modification by Ar complexing.

The intrastate coupling depends on the excess vibrational energy, while the nature of the mediated interstate coupling depends on the nature of the molecule. In Fig. 26 we present the relevant coupling schemes which are encountered in this class of compounds. The following cases were documented:

(1) The interstate $S_1 - \{T_1\}$ coupling to the statistical limit, while intrastate coupling does not prevail. This situation corresponds to the $S_1(0)$ origins of 9CNA, 9,10DCA, and 9,10DBA. ISC is very inefficient, being exhibited only for $S_1(0)$ of 9,10DBA.

(2) The interstate coupling $S_1 - \{T_x^k\} - \{T_1\}$ is mediated with the sparse $\{T_x\}$ manifold while $T_x^k \rightarrow \{T_1\}$ coupling is statistical. No intrastate coupling prevails. This situation corresponds to (i). The $S_1(0)$ origin and low vibrational excitation, i.e., range (A) of anthracene, its deuterated anthracenes, and 9MA. (ii) The electronic origin and low vibrational excitation 9BA, where the very low quantum yield is due to the high spin–orbit interaction. (iii) Some vibrational excitations of 9,10DCA and 9,10DBA which exhibit resonance effects on ISC.

(3) The interstate coupling $S_1 - \{T_x^k\} - \{T_1\}$ is mediated by the $\{T_1\}$ manifold, while intrastate coupling is effective in the S_1 manifold and corresponds to the intermediate level structure. This state of affairs corresponds to participation of both doorway and background S_1 states in the ISC process. This state of affairs corresponds to range (B) in anthracene, deuterated anthracenes 9CNA and 9BA.

(4) The interstate $S_1 - \{T_x^k\} - \{T_1\}$ coupling is mediated, with the $\{T_x^k\}$ manifold being statistical. Intrastate coupling between the doorway and background S_1 states prevails and IVR corresponds to the statistical limit. The ISC rates are determined by the ISC rates of the background S_1 states, which decay to the statistical $\{T_x^k\}$ manifold. These ISC rates exhibit a weak E_v dependence. This state of affairs
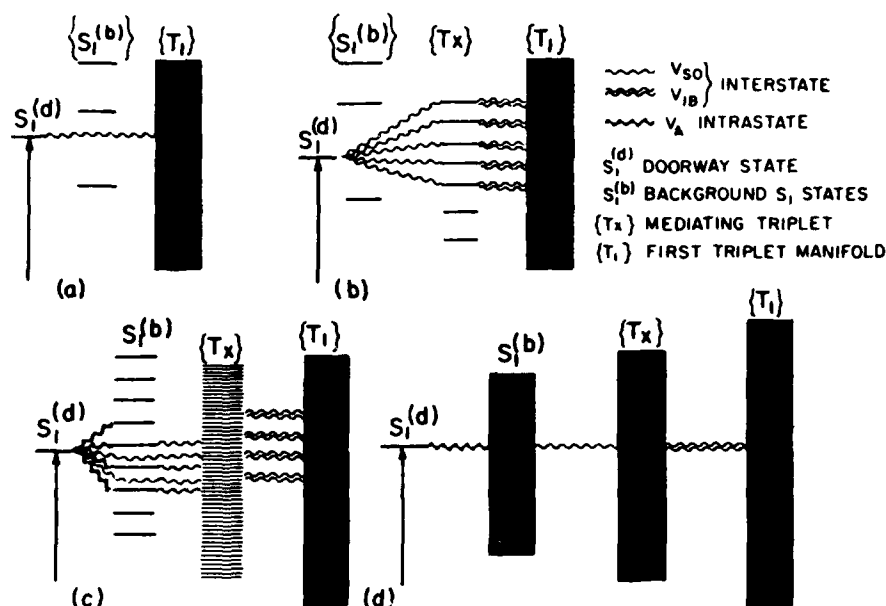
FIG. 26. Interstate and intrastate coupling schemes for intersystem crossing. (a) A doorway state of a very sparse S_1 manifold undergoing direct ISC to a (T_1) quasicontinuum. (b) A doorway state of a very sparse S_1 manifold undergoing mediated ISC through near-resonant coupling with a sparse (T_x) manifold. (c) The S_1 manifold becomes denser and intrastate coupling between the doorway state background S_1 states prevails. The mixed $S_1^{(d)} + S_1^{(b)}$ states decay via mediated ISC. (d) The $S_1^{(b)}$ and (T_x) manifolds are statistical relaxation and can be described in terms of sequential decay, i.e., $S_1^{(d)} \to (S_1^{(b)}) \to (T_x) \to (T_1)$, which corresponds to a sequence of IVR, ISC, and triplet–triplet internal conversion.

prevails at high values of E_v for all the anthracene derivatives in range (C). From the limiting high E_v quantum yields (Table VII) we infer that the ISC rates depend on the intramolecular spin–orbit coupling, as expected. In range (C) the ISC rates (Table VII) are weakly dependent on the position of the same classical substituents and on the isotopic substitution. The erosion of the inverse deuterium isotope effect in this range can be rationalized in terms of $\{S_1\} \to \{T_x^k\}$ ISC in the statistical limit which corresponds to a small electronic energy gap.[73]

The intramolecular dynamics in the S_1 manifold of anthracene and its derivatives exhibits mode specificity of ISC due to the interplay between two classes of effects. First, intrastate coupling, which corresponds to the intermediate level structure in S_1, and second, resonance effects due to interstate coupling of S_1 states with a relatively sparse $\{T_x^k\}$ manifold. These mode-specific effects will prevail only provided that either the $\{S_1\}$ manifold or the $\{T_x^k\}$ manifold is

sparse. Such effects are expected to be exhibited only in the low energy region (A) and in the intermediate energy region (B). In the high E_v domain all vibrational mode specificity for ISC disappears due to efficient IVR in the S_1 manifold, while all resonance effects are cancelled out in the statistical mediating $\{T_x\}$ manifold. Intramolecular ISC in this high-energy domain corresponds to "chemical"-type intramolecular dynamics in an isolated molecule where all mode-specificity effects are eroded.

ACKNOWLEDGMENTS

TABLE VII. High E_v ISC rates of anthracene derivatives.

Molecule	E_v (cm^{-1})	Y	$k_{nr} \tau_{rad}$
Anthracene	2919	0.132	6.6
Anthracene-D_{10}	2893	0.130	6.7
9CN Anthracene	2718	0.13	6.7
9,10-dichloroanthracene	8271	0.017 1	58
9-bromoanthracene	1770	0.001 24	806
9,10-dibromoanthracene	2860	0.001 8	550

[1]H. Von Weyssenhoff and E. W. Schlag, J. Chem. Phys. 51, 2508 (1968).
[2]C. S. Parmenter and M. W. Schuyler, Chem. Phys. Lett. 6, 339 (1970).
[3]K. G. Spears and S. A. Rice, J. Chem. Phys. 55, 5561 (1971).
[4]J. C. Hsieh, C. S. Huang, and E. C. Lim, J. Chem. Phys. 60, 4345 (1974).
[5]D. H. Levy, Annu. Rev. Phys. Chem. 31, 197 (1980).

[6]A. Amirav, U. Even, and J. Jortner, J. Chem. Phys. 71, 2319 (1979).

[7]F. M. Behlem, N. Mikami, and S. A. Rice, Chem. Phys. Lett. 60, 364 (1979).

[8]A. Amirav, U. Even, and J. Jortner, J. Chem. Phys. 75, 3770 (1981).

[9]U. Even and J. Jortner, J. Chem. Phys. 77, 4391 (1982).

[10]W. R. Lambert, P. M. Felker, and A. H. Zewail, J. Chem. Phys. 75, 5958 (1981).

[11]P. M. Felker, W. R. Lambert, and A. H. Zewail, Chem. Phys. Lett. 89, 309 (1982).

[12]P. M. Felker and A. H. Zewail, Chem. Phys. Lett. 102, 113 (1983).

[13]A. Syage, W. R. Lambert, P. M. Felker, A. H. Zewail, and R. M. Hochstrasser, Chem. Phys. Lett. 88, 266 (1982).

[14]P. M. Felker, W. R. Lambert, and A. H. Zewail, J. Chem. Phys. 77, 1603 (1982).

[15]P. M. Felker, J. A. Syage, W. R. Lambert, and A. H. Zewail, Chem. Phys. Lett. 99, 1 (1982).

[16]P. M. Felker and A. H. Zewail, Chem. Phys. Lett. 94, 448, 454 (1983); J. Chem. Phys. 78, 5266 (1983).

[17]W. R. Lambert, P. M. Felker, and A. H. Zewail, J. Chem. Phys. 81, 2217 (1984).

[18]W. R. Lambert, P. M. Felker, J. A. Syage, and A. H. Zewail, J. Chem. Phys. 81, 2195 (1984).

[19]J. A. Syage, P. M. Felker, and A. H. Zewail, J. Chem. Phys. 81, 2209 (1984).

[20]T. Majors, U. Even, and J. Jortner, J. Chem. Phys. 81, 2330 (1984).

[21]K. Rademann, U. Even, S. Rozen, and J. Jortner, Chem. Phys. Lett. 125, 5 (1986).

[22]S. Okajima, B. E. Forch, and E. C. Lim, J. Phys. Chem. 87, 4571 (1981).

[23]T. R. Hyes, W. Henke, H. Selze, and E. W. Schlag, Chem. Phys. Lett. 77, 19 (1981).

[24]A. Amirav, U. Even, and J. Jortner, Chem. Phys. Lett. 83, 1 (1981).

[25]T. Zwier, E. Carrasquillo, and D. H. Levy, Chem. Phys. 78, 5493 (1983).

[26]A. Amirav and J. Jortner, Chem. Phys. Lett. 94, 547 (1983); 95, 295 (1983).

[27]M. Sonnenschein, A. Amirav, and J. Jortner, J. Phys. Chem. 88, 4217 (1984).

[28]A. Amirav, M. Sonnenschein, and J. Jortner, Chem. Phys. Lett. 100, 488 (1983).

[29]A. Amirav and J. Jortner, J. Chem. Phys. 84, 1500 (1986).

[30]A. Amirav, M. Sonnenschein, and J. Jortner, Chem. Phys. 102, 305 (1986).

[31]We have measured the vibrational energy dependence of the absolute quantum yield in the S_1 manifold of tetracene, perylene, fluorene, carbozole, indole, transstilbene, and 4-Cl transstilbene. A Amirav and J. Jortner (unpublished).

[32]R. E. Kellog, J. Chem. Phys. 44, 411 (1966).

[33]R. G. Bennet and P. J. McCartin, J. Chem. Phys. 44, 1969 (1966).

[34]W. R. Ware and B. A. Baldwin, J. Chem. Phys. 43, 1194 (1965).

[35]E. C. Lim, J. D. LeDosa, and J. M. Yu. J. Mol. Spectrosc. 19, 412 (1966).

[36]M. Bixon and J. Jortner, J. Chem. Phys. 48, 715 (1968).

[37]J. P. Roberts and R. S. Dixon, J. Phys. Chem. 75, 845 (1971).

[38]Y. H. Meyer, R. Astier, and J. M. Leclerq, J. Chem. Phys. 56, 801 (1972).

[39]A. Kearbell and F. Wilkinson, J. Chim. Phys 20, 125 (1970).

[40]T. F. Hunter and R. F. Wyatt, Chem. Phys. Lett. 6, 221 (1970).

[41]R. P. Widman and J. R. Huker, J. Phys. Chem. 76, 1524 (1972).

[42]G. D. Gillespie and E. C. Lim, J. Chem. Phys. 65, 2202 (1976).

[43]G. D. Gillespie and E. C. Lim, Chem. Phys. Lett. 63, 355 (1979).

[44]K. C. Wu and W. R. Ware, J. Am. Chem. Soc. 101, 5906 (1979).

[45]K. Hamanouse, S. Hirayama, T. Nakayama, and H. Teranishi, J. Phys. Chem. 84, 2074 (1980).

[46]M. Tanaka, I. Tanaka, S. Tai, K. Hamanouse, M. Sultani, and K. Yoshihara, J. Phys. Chem. 87, 813 (1983).

[47](a) A. Amirav, U. Even, and J. Jortner, J. Chem. Phys. 75, 2489 (1981); (b) S. Leutwyler, Chem. Phys. Lett. 107, 284 (1984).

[48]A. Amirav and J. Jortner, Chem. Phys. Lett. 132, 335 (1986).

[49]G. Beck, Rev. Sci. Instrum. 45, 318 (1974).

[50]R. Parish, J. Chem. Phys. 24, 250 (1956); 25, 1112 (1956).

[51]A. J. McHugh and I. G. Ross, Spectroschim. Acta 24A, 441 (1970).

[52]F. W. Birss, S. D. Colson, and D. A. Ramsay, Can. J. Phys. 51, 1031 (1973).

[53]F. A. Novak and S. A. Rice, J. Chem. Phys. 71, 4680 (1979); 73, 858 (1980).

[54](a) E. Riedle and H. J. Neusser, J. Chem. Phys. 80, 4686 (1984); (b) E. Riedle, H. J. Neusser, and E. W. Schlag, J. Phys. Chem. 86, 4877 (1982).

[55](a) A. Amirav, J. Jortner, S. Okajima, and E. C. Lim, Chem. Phys. Lett. 126, 487 (1986); (b) A. Amirav, J. Jortner, M. Terazima, and E. C. Lim, ibid. 133, 179 (1987).

[56](a) B. E. Forch, K. T. Chen, H. Saigusa, and E. C. Lim, J. Phys. Chem. 87, 2280 (1983); (b) B. E. Forch and E. C. Lim, Chem. Phys. Lett. 110, 593 (1984); (c) A. Amirav, J. Chem. Phys. 86, 4607 (1987).

[57]A. Amirav, Chem. Phys. 108, 403 (1986).

[58]W. E. Henke, W. Yu, H. L. Selzle, E. W. Schlag, D. Wutz, and S. H. Lin, Chem. Phys. 92, 187 (1985).

[59]N. Liver, A. Nitzan, A. Amirav, and J. Jortner (to be published) J. Chem. Phys. (in press).

[60]Y. Hirata and E. C. Lim, J. Chem. Phys. 69, 3292 (1978).

[61](a) N. Neto, M. Scrocco, and S. Califano, Spectrochim. Acta 22, 1981 (1966); (b) K. Ohno, J. Mol. Spectrosc. 77, 329 (1979).

[62]J. Murakami, M. Ito, and K. Kaya, Chem. Phys. Lett. 80, 203 (1981).

[63]A. Amirav, U. Even, and J. Jortner, Anal. Chem. 54, 1666 (1982).

[64]A. Amirav, J. Jortner, S. Okajima, and E. C. Lim, Chem. Phys. Lett. 126, 487 (1986).

[65]P. M. Felker and A. H. Zewail, J. Chem. Phys. 82, 2961 (1985).

[66]P. M. Felker and A. H. Zewail, J. Chem. Phys. 82, 2975 (1985).

[67]P. M. Felker and A. H. Zewail, J. Chem. Phys. 82, 2994 (1985).

[68]D. P. Craig and G. J. Small, J. Chem. Phys. 50, 3827 (1969).

[69]J. A. Warren, J. M. Hayes, and G. J. Small, Chem. Phys. 102, 323 (1986).

[70]F. Duschinsky, Acta Phys. 7, 551 (1937).

[71]J. A. Warren, J. M. Hayes, and G. J. Small, Chem. Phys. 102, 313 (1986).

[72]U. Even, A. Amirav, S. Leutwyler, M. J. Ondrechen, Z. Berkovitch-Yellin, and J. Jortner, Faraday Discuss. Chem. Soc. 73, 153 (1982).

[73]R. Englman and J. Jortner, Mol. Phys. 18, 145 (1970).

Energetics and Dynamics of Clusters.

J. JORTNER, D. SCHARF and U. LANDMAN (*)

School of Chemistry, Tel Aviv University - 69978 Tel Aviv, Israel

[a]Reference 22.
[c]Reference 19.
[f]Reference 23.
[g]A. Amirav and J. Jortner (unpublished).
[h]Calculated from $\tau_{rad} = Y^{-1}\tau$.

1. - Prologue.

Structural, electronic, dynamic and chemical characteristics of materials depend primarily on the state (*i.e.* the phase) and on the degree (*i.e.* the size) of aggregation. The level structure of elementary excitations, *e.g.*, phonons, electrons, excitons in clusters, *i.e.* finite aggregates [1-3], cannot be characterized in terms of the conceptual framework, which rests solely on one of the two traditional disciplines of solid-state physics and of molecular physics (table I). The area of the structure, level structure and dynamics of clusters, which is the subject matter of these lectures, bridges the gap between solid-state and molecular physics. The properties of clusters in microscopically inhomogeneous solids, *e.g.*, granular metals, have been studied for a long time [4]. Impetus for the interrogation of the properties of clean and isolated clusters stemmed from the remarkable progress in the areas of supersonic jets and cluster beams [5, 6], which provided the basis for intensive and extensive experimental and theoretical effort. As an example we consider the equilibrium structure of a characteristic rare-gas cluster, $(Ar)_{13}$ (fig. 1), which was determined from classical molecular-dynamics calculations, and which exhibits the icosahedron structure (to be discussed in sect. 2).

There are some compelling reasons for the study of isolated clusters.

A) Exploration of new basic physical phenomena. These are finite systems with a congested spectrum of energy levels (for electronic states, phonons, etc. [7]). The level structure can be varied continuously by changing the cluster size. Accordingly, one can accomplish a « continuous transition » from molecular to solid-state systems.

B) Microscopic approach to macroscopic phenomena, such as nucleation, adsorption and desorption and catalysis [2].

(*) Permanent address: School of Physics, Georgia Institute of Technology, Atlanta, GA 30322.

438

TABLE I. — *Unified concepts for the description of solid-state and molecular systems.*

Properties	Discipline	
	Solid-state physics	Molecular physics
Symmetries	Ubiquity of ordered structures with (approximate) symmetry of a periodic space group. Note that positionally and compositionally ordered structures (broken symmetries) also exist	A finite set of bound atoms whose equilibrium structure can be specified in terms of permutation symmetry and (approximate) point group symmetry
Density of states for elementary excitations	Continuous; characterized by Van Hove topological singularities for ordered structures and by exponential Mott tails for disordered materials	Discrete for low-energy excitations
Characteristic lengths of elementary excitations	Phonon wavelength, electron mean free path and coherence lengths are considerably shorter than sample dimensions	Concept not directly applicable
Vibrational excitations	Continuous density of phonon states	Fundamental vibrational excitations are discrete, being characterized in terms of normal and local modes. In large molecules quasi-continuum of vibrational states exists at high energies
Electronic states	Continuous density of electronic states	Discrete electronic excitations below fast ionization potential

C) A variety of technological applications [1-3] rests on cluster physics and chemistry. These include photography, aerosols and smoke, sintering of small particles in vacuum, plasma injection, as well as magnetism and superconductivity of metallic clusters.

D) Astrophysical applications. The elucidation of the nature, the formation mechanism and the properties of cosmic dust rests on cluster science [8].

The first obvious question is, how does a cluster hold itself together? The energetic stability of a cluster is determined by the binding. A classification of the nature of the chemical bonds in clusters is presented in table II. Clusters
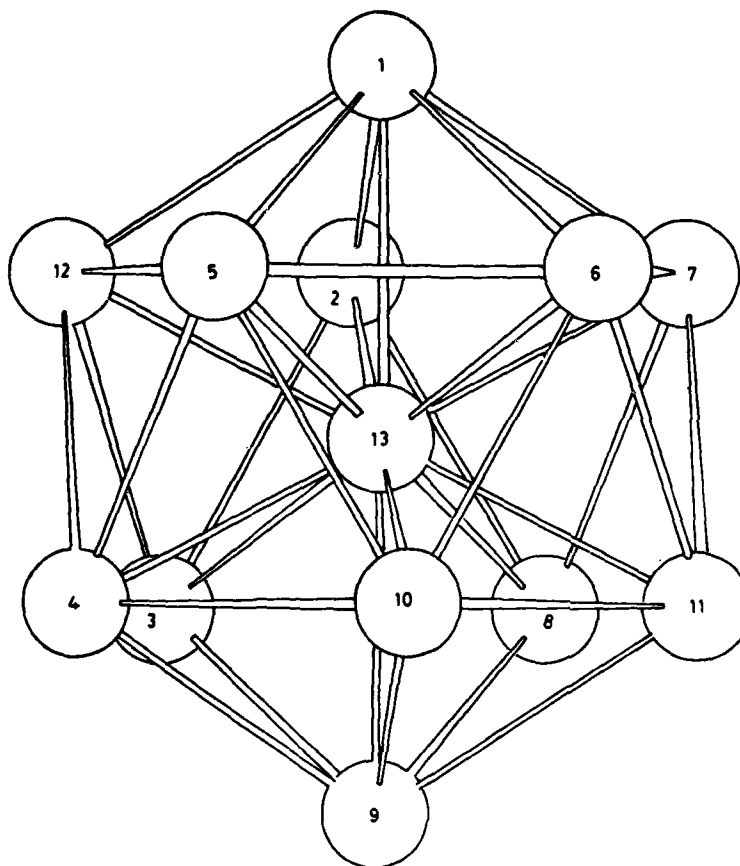
Fig. 1. – The equilibrium structure of the $(Ar)_{13}$ cluster obtained from molecular-dynamics calculations at 24 K.

fall into two general categories according to the strength of the chemical binding:

1) « Weak interaction » prevailing for Van der Waals (VdW) type, as well as for molecular and hydrogen-bonded clusters.

2) « Strong interactions », which encompass ionic and valence clusters, as well as many metallic clusters.

The atomic structure of the cluster (at 0 K) is a direct consequence of the binding. At finite temperatures the contribution of the vibrational excitations in the free energy of the cluster has to be incorporated. Figure 2 provides a typical example for the temperature dependence of the equilibrium configuration of alkali halide clusters, which were explored by MARTIN [9] and by us [10].

TABLE II. – *Classification of binding in clusters.*

Type	« Canonical » cases	Cause of binding	Average binding energies	Occurrence
Van der Waals clusters	rare gases R_n $(N_2)_n$, $(CO_2)_n$, $(SF_6)_n$	dispersive plus weak electrostatic	weak binding $D < 0.3$ eV	aggregates of rare gases and closed-shell molecules
molecular clusters	organics $(M)_n$ $(I_2)_n$	dispersive electrostatic (weak valence)	moderate binding $D \sim (0.3 \div 1)$ eV	aggregates of organic molecules and some closed-shell molecules
hydrogen-bonded clusters	$(HF)_n$, $(H_2O)_n$	H-bonding electrostatic charge transfer	moderate binding $D \sim (0.3 \div 0.5)$ eV	closed-shell molecules containing H and electronegative elements
ionic clusters	$(NaCl)_n$, $(CaF_2)_n$	ionic bonds charge-charge interactions shell effects $(IP + EA)$	strong binding $D \sim (2 \div 4)$ eV	metals from left-hand side of periodic table plus right-hand side electronegative elements
valence clusters	C_n, S_8, As_4	« conventional » chemical bonds	strong binding $D \sim (1 \div 4)$ eV	isomeric molecules and radicals
metallic clusters	Na_n, Al_n, Cu_n, W_n	« metallic » bond low KE of electrons	moderate to strong binding $D \sim (0.5 \div 3)$ eV	wide occurrence to the left of B, Si, Ge, Sb, Po in rows $2 \div 6$ of periodic table

The cubic structure constitutes the stable equilibrium configuration of the $(NaCl)_4$ cluster at 0 K. At finite temperatures the vibrational entropy contribution, S, to the free energy, G, has to be incorporated, *i.e.*

$$(1.1) \quad \begin{cases} G = E - TS, \\ E = E_0 + \sum_i \hbar\omega_i/2, \\ S = kT \ln\left[1 - \exp\left[-\hbar\omega_i/kT\right]\right], \end{cases}$$

where E is the potential energy E_0 corrected for zero-point energy, and $\hbar\omega_i$ are the characteristic frequencies. The entropy contribution favours the ring structure for $(NaCl)_4$ at high temperatures. At 400 K the relative concentration is 50%, the ring structure becoming dominant at temperatures exceeding 900 K. At a finite temperature $(NaCl)_4$ clusters will exhibit a small number of dominant structures underlying dynamic isomerization between these configurations. This simple example demonstrates the crucial role of nuclear excitations and the vibrational entropy in determining the stability and equilibrium configurations of clusters at finite temperatures.
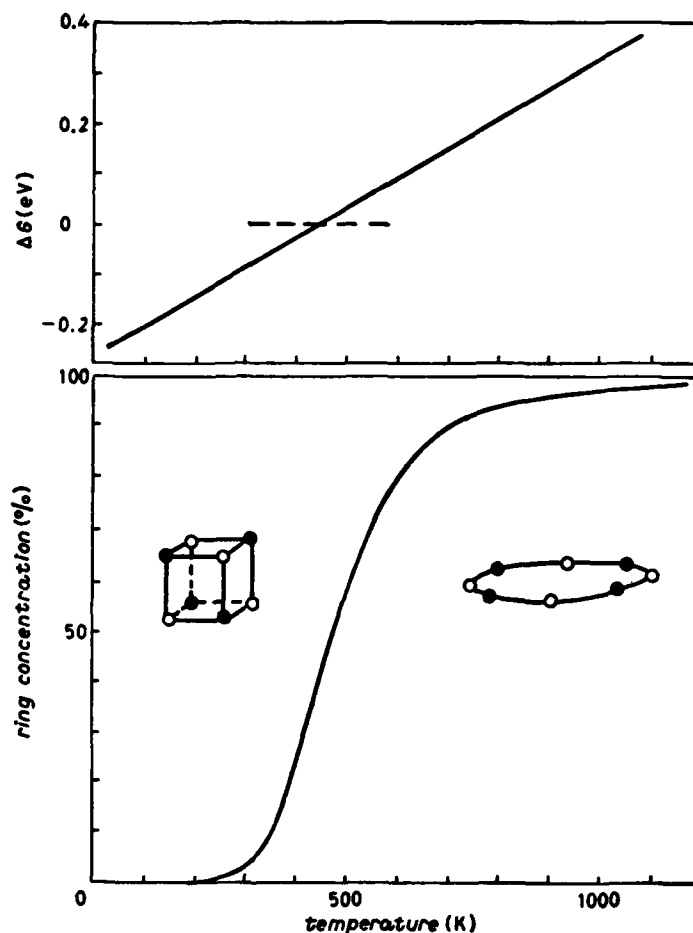
Fig. 2. – Free-energy difference between the cubic and the ring-shaped cluster of $(NaCl)_4$ (top). The temperature dependence of the relative concentration of the ring-shaped structure (bottom). Data from ref. [9, 10].

The characteristic examples alluded to in this section pertain to rare-gas and alkali halide clusters. In what follows, we shall limit ourselves to the diverse area of nonmetallic systems notwithstanding the rich and interesting area of metallic clusters.

2. – Classification of clusters.

It is useful to provide a classification of clusters according to size. The smallest constituent is the dimer ($n = 2$), which should rather be considered

separately as a «molecular» entity. The dimer acts as an essential and basic
ingredient in nucleation. Then, in order of increasing size, we have for non-
metallic systems:

2`1. *Microclusters* ($n = 2 \div 10$ or 13). – These involve VdW molecules for
weak interactions and ionic and covalent molecular structures for strong
interactions. The molecular structure is usually well characterized, although
for larger microclusters several nearly isoenergetic isomers may exist. A well-
known example involves the microclusters of rare gases [11-13] (fig. 3), which
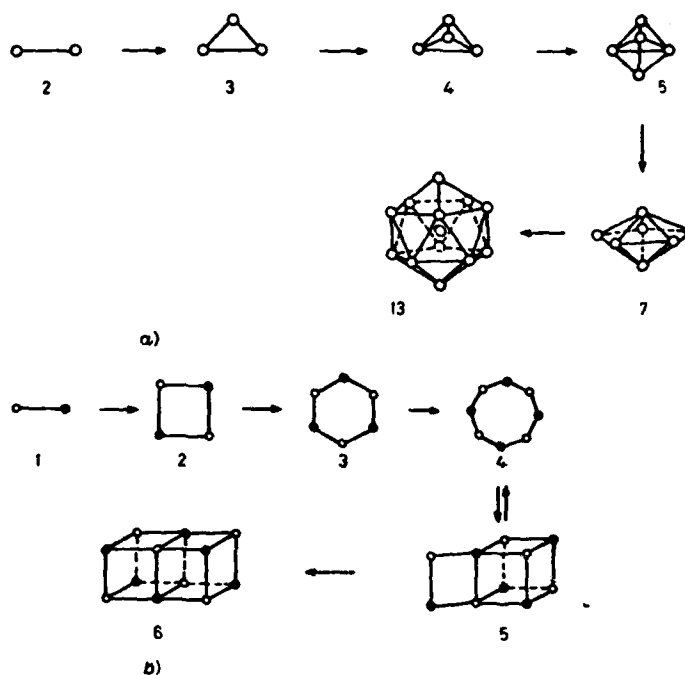
Fig. 3. – Structures of rare-gas (ref. [11-13]) and of ionic microclusters (ref. [9]).

are characterized by the most compact noncrystalline ordered structures,
e.g., equilateral triangle ($n = 3$), regular tetrahedron ($n = 4$), triangular bi-
pyramid ($n = 5$) and a pentagonal pyramid ($n = 7$). For $n = 13$ the cele-
brated icosahedron structure with the multiple pentagonal symmetry is more
stable than hexagonal closed-packed and face-centred cubic structures, con-
stituting a building block for larger $n = 33$, $n = 55$ and $n = 147$ structures,
and which may involve a basic structural unit for amorphous materials.
Molecular-dynamics calculations [13-17] indicate the existence of amorphous,
liquid-type, rare-gas structures at higher temperatures. For ionic micro-

clusters [9], the noncrystalline structures are stable for low n (fig. 3) and nearly isoenergetic isomers are abundant. The cubic, solid-state structure begins to exhibit energetic stability for relatively small neutral alkali halide structures with $n > 8$. Regarding elementary excitations in microclusters, we note that the molecular vibrations are discrete, being characterized by large-amplitude nuclear motion. The electronic states below ionization are discrete. These characteristics of the elementary excitations correspond, of course, to molecular systems.

2'2. *Small clusters* $(n \sim 10 \div 10^2)$. – The usefulness of molecular concepts breaks down as the molecular structures are characterized by a large number of isomers. Furthermore, amorphous structures also become common. The vibrational motion of such small clusters is complex.

2'3. *Large clusters* $(n > 10^2)$. – A gradual evolution of a solid-state structure is exhibited at $n > 10^3$. A quasi-continuum density of states for electronic states (*i.e.* « valence band » and « conduction band ») and for phonons appears with increasing n. Furthermore, macroscopic surface and volume emerge with increasing cluster size.

3. – Large clusters.

Let un now consider some unique characteristics of large clusters, which differ from the properties of bulk material.

A) Large surface/volume ratio. The fraction of the number of surface atoms n_s is $n_s/n = 4/n^{\frac{1}{3}}$, being $n_s/n \simeq 0.4$ for $n = 10^2$, $n_s/n \simeq 0.2$ for $n = 10^4$ and $n_s/n \simeq 0.04$ for $n = 10^6$. The structural, energetic and dynamic properties of the « microsurfaces » of clusters are of considerable interest.

B) Quantum size effects [7, 17]. The dependence of the specific properties, *e.g.*, electric and magnetic susceptibilities, of clusters on their geometrical dimensions originate from two interrelated causes. Firstly, the effective wavelength of excitations is comparable with the cluster size, resulting in boundary scattering effects. In this context, the effect of finite cluster size on large-radius Wannier exciton states [18] and large polarons [19] in solid rare gases and alkali halide clusters will be of considerable interest. Secondly, the sample size d is small, so that the energy gap, Δ, for excitations is comparable to the thermal energy $k_B T$, to the magnetic interaction μH, or to the spectral resolution. For example, for the case of phonons,

$$(3.1) \qquad\qquad \Delta \sim h v / d ,$$

where $v \sim 10^5$ cm s^{-1} is the velocity of sound. Thus quantum size effects will be severe when $\Delta \sim k_B T$ or $d \sim 100$ Å$/T(\text{K})$, so that at $T = 10$ K we estimate $d \sim 10$ Å and $n \sim 100$. On the other hand, for electronic states in the tight-binding scheme, one has

$$(3.2) \qquad\qquad \Delta \sim zJ/n \, ,$$

where J is the transfer integral, while z is a numerical constant which takes the value $z = \pi$ for 1 dimension and, in general, we can set z to be approximately equal to the average number of nearest neighbours. Taking $J = 1$ eV and $z = 6$, the electronic gap is comparable to the thermal energy when $n \sim 6 \cdot 10^4/T(\text{K})$, so that $n \sim 6000$ at $T = 10$ K. The different values of n emerging from the estimates of Δ for phonons and for electronic excitations clearly demonstrate that quantum size effects are not universal and depend on the specific physical property.

C) Thermodynamic size effects [7, 20, 21]. An important class of size effects involves the dependence of some intensive thermodynamic properties, e.g., surface tension, vapour pressure and the characteristics of phase transitions, on the sample size and shape.

An intriguing phenomenon within the category of thermodynamic size effects involves the melting of small clusters. It was predicted in 1909 that the melting temperature of droplets will decrease with decreasing size [22]. This prediction has been borne out by an experimental observation [23] of a dramatic dependence of T_m on the size of gold clusters supported on a substrate (fig. 4). Of some interest are the results of numerical simulations on Ar$_n$ clusters (fig. 5), which mimic the melting for very small microclusters as low as $n = 7$. We note that T_m seems to increase monotonically in the range $n = 7 \div 13$, with the $n = 13$ icosahedron structure exhibiting extra stability for melting. Three distinct, though related, approaches can be adopted for the description of the drastic lowering of T_m when decreasing the cluster size.

a) Thermodynamics of finite systems. A simple thermodynamic argument [21, 22] rests on the contribution of the surface tension, σ, to the chemical potential of droplets. As σ decreases by melting, the melting temperature will be size dependent. Two inherent difficulties arise in connection with the simple thermodynamic picture. Firstly, fluctuations are severe in a finite system, precluding the exact definitions of T_m. Secondly, in a finite system « phase transitions » are expected to be gradual rather than sharp.

b) Description of melting in terms of large nuclear displacements. Lindeman's hypothesis of melting [24, 25] rests on the notion of the onset of large vibrational displacements. Accordingly, the low melting temperature of small clusters implies the occurrence of large-amplitude nuclear motion.
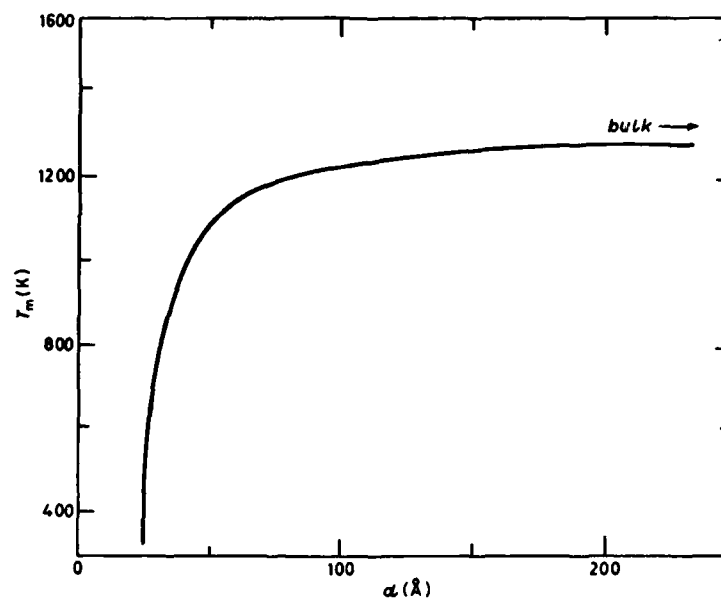
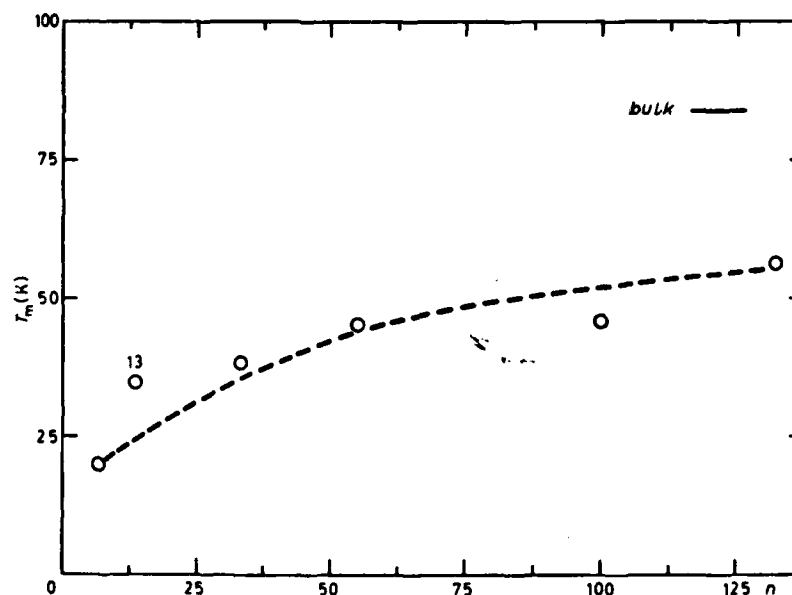Fig. 4. – Size dependence of melting temperature of gold clusters supported on a subtrate (ref. [23]).

Fig. 5. – Melting temperatures of Ar_n ($n = 7 \div 133$) microclusters and small clusters from molecular-dynamics computer simulations (ref. [14-16]).

c) *Dynamic description of melting.* Melting of clusters has been described by BERRY *et al.* [26] in terms of fast isomerization between several nuclear configurations. This model bears a close analogy to the Stillinger-Weber [27] description of a liquid in terms of a system passing from a region around one potential minimum to another.

From the descriptions of *b*) and *c*) of the melting of clusters at low temperature, several interesting qualitative conclusions emerge.

i) In view of their low melting temperature, large-amplitude nuclear motion is expected to be exhibited in microclusters at low temperatures.

ii) Structural and time-resolved studies of isomerization may provide direct information on phase transitions in clusters.

iii) Time-resolved studies of isomerization will open up a new research area of the dynamics of phase transitions in finite systems.

4. – Heteroclusters.

Up to this point we have alluded to some features of chemically neat clusters. The exploration of the properties of doped clusters is of considerable interest, as an added guest molecule may act as a microscopic probe for the molecular structure, the nuclear motion and the electronic excitation of the cluster. Studies of doped clusters provided insight into three classes of phenomena.

1) The configurational changes induced by doping.

2) The cluster-guest molecule interactions modify the energetics of vibrational and electronic excitations and the intramolecular dynamics (*i.e.* intramolecular vibrational-energy redistribution and interstate electronic relaxation) of the guest molecule.

3) Clustering around a guest molecule opens up new decay channels for the disposal of vibrational and electronic energy of the guest, *e.g.*, vibrational predissociation in microclusters and vibrational relaxation in large clusters [28, 29]. Some classes of interesting heteroclusters are assembled in table III. Heteroclusters can be classified according to their charge into neutral, positively charged and negatively charged aggregates. The neutral heteroclusters involve doped VdW clusters [28-31] held together by dispersive and weak electrostatic interactions, as well as doped molecular [32] and hydrogen-bonded clusters [33], which involve an organic or inorganic molecule solvated by nonpolar (*e.g.*, CCl_4) or by polar (*e.g.*, H_2O) ligands. These interactions are reminiscent of those prevailing in nonionic solutions. Positive heteroclusters span a broad spectrum of systems. The weakest electrostatic

TABLE III. – *Some heteroclusters.*

Type	Examples	Cause of binding	References
doped Van der Waals clusters	$(I_2)R_n$ $(n = 1 \div 6)$ $(SF_6)R_n$ $(n = 1 \div 50)$ tetracene$\cdot R_n$ $(n = 1 \div 200)$	dispersive and weak electrostatic	[28-31]
doped molecular and H-bonded clusters	$(HNO_3)_x$ $(H_2O)_y$ $(x = 1 \div 6, \ y = 2 \div 20)$ tetracene$\cdot(CCl_4)_n$ $(n = 1 \div 3)$	electrostatic and H-bonding dispersive and weak electrostatic	[33] [32]
doped positive Van der Waals clusters	$(C_6F_6^+)Ar_n$	dispersive plus polarization	[34]
positive ions in Van der Waals clusters	$(He_n)^+$ $(n \simeq 68\ ^4He; \ 85\ ^3He)$ $(Ar_n)^+$	dispersive and polarization hole trapping	[35] [36]
ionic complexes	$H^+(H_2O)_n$ $Na^+(H_2O)_n$ $Na^+(SO_2)_n$	charge dipole	[33, 37]
simple ionic clusters	$(H_n)^+$ $(n = 3 \div 15)$ $(n = 500 \div 1000)$	valence and polarization	[38] [39]
negative-ion clusters	$(CO_2)_n^-$	solvation of negative molecular ion	[40] [41]
solvated-electron clusters	$(H_2O)_n^-$ $(NH_3)_n^-$	electron localization in an extended state	[42-44]

interactions prevail in positive VdW heteroclusters [34], involving a positive large ion in a rare-gas cluster, which is held together by charge-induced dipole and dispersive interactions. Similar interactions prevail in He_n^+ clusters [35], where the charge-induced dipole interaction results in electrostriction. Ionic complexes [33, 37], *e.g.*, $H^+(H_2O)_n$ and $Na^+(SO_2)_n$, are bound by stronger electrostatic charge-dipole interactions, as those prevailing in ionic solutions. Chemical bonding is exhibited in positive-ion rare-gas clusters of R_n^+, where the positive R_2^+ molecular diatomic ion is formed within the cluster [45, 46]. Another extreme case of valence interaction in clusters involves ionic clusters, *e.g.*, the H_n^+ aggregates [38, 39], which presumably consist of an H_3^+ ion bound to an ensemble of H_2 molecules. Negative clusters fall into two broad categories. i) The negative-ion clusters involve localization of the excess electron within a single molecule [40, 41], resulting in the formation of a «conventional» negative ion, and ii) the excess electron cluster which involves electron localization within the cluster [42-44]. We shall now proceed to discuss some features of charged clusters, focusing attention on the formation mechanism of positively charged clusters and on the nature of extended excess electron states in negatively charged clusters.

5. – Ionization of clusters.

Selective ionization processes via one-photon or multiphoton ionization of VdW and molecular clusters provide direct information on the energetics of the formation of positively charged clusters. The energetics of ionization can be utilized to elucidate the nature of intramolecular and intermolecular nuclear configurational changes accompanying the formation of positively charged microclusters. In this context, the following mechanisms are relevant.

5‘1. *Small-polaron effects.* – Ionization of a molecule in a cluster may be accompanied by a change in the intramolecular nuclear equilibrium configuration [47]. When such a molecule is ionized within the cluster (fig. 6), the transfer

a)

b)
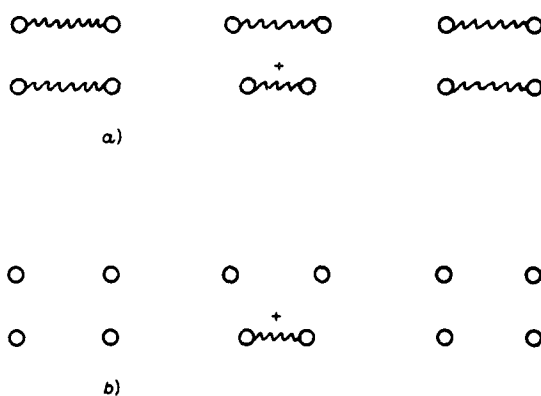
Fig. 6. – Ionization mechanisms: *a)* small-polaron effects, *b)* hole trapping.

integral J, which is responsible for the intermolecular hole transfer, corresponds to an electronic contribution, J_e, reduced by the nuclear Franck-Condon factor F, so that $J = J_e F$. An immediate energetic implication of these « dressed » intermolecular interactions, J, involves the lowering of the ionization potential $I(n)$ of the n-th cluster relative to the monomer ionization potential $I(1)$. For a one-dimensional system a simple molecular-orbital calculation results in the relation [48]

$$(5.1) \qquad I(n) = I(1) - 2|J| \cos \frac{\pi}{n+1} \, .$$

Invoking the approximate relation [49] $\cos\left(\pi/(n+1)\right) = 1 - 1/n$ for $n = 2 \div 10$ results in

$$(5.2) \qquad I(n) = \left[I(1) - 2|J|\right] + \frac{2|J|}{n} \, .$$

For a multidimensional system, we can replace the numerical factor of 2 in eq. (5.2) by the number of nearest neighbours, z, so that eq. (5.2) is generalized to read

$$(5.3) \qquad I(n) = [I(1) - z|J|] + \frac{z|J|}{n}.$$

Relation (5.3) results in the general linear dependence of $I(n)$ vs. n^{-1} (fig. 7) proposed by TROTT et al. [49]. This relation is well obeyed for $((CH_3)_2CO)_n$ ($n = 1\div4$) [49], $(NO)_n$ ($n = 1\div5$) [50] and $(CS_2)_n$ ($n = 1\div4$) [51] microclusters. From the linear plots of fig. 7, we deduce the reasonable value $z|J| \simeq 1$ eV for the hole transfer integral in these microclusters.
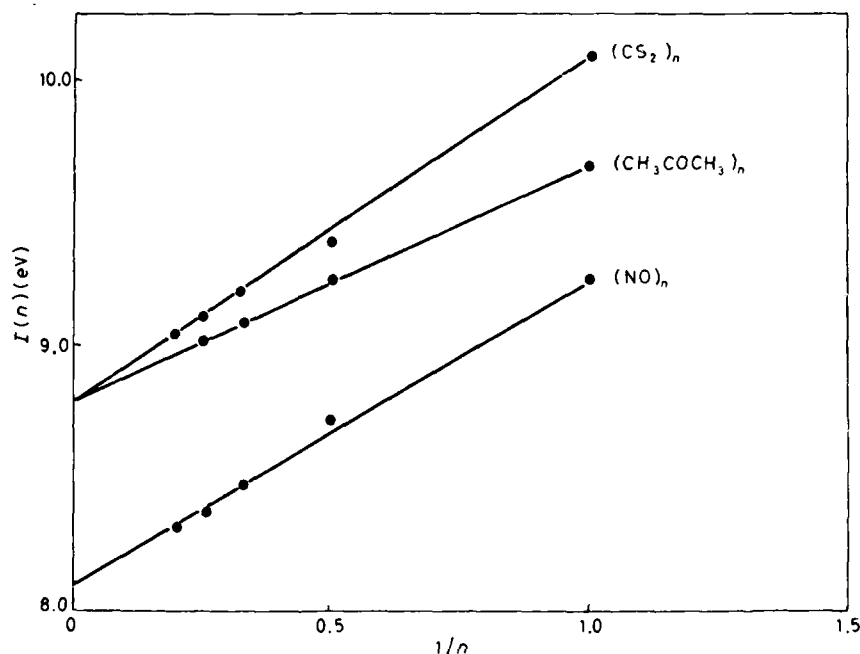
Fig. 7. – Small-polaron effects on the ionization potentials of microclusters of polyatomic molecules, exhibiting the linear $I(n)$ vs. n^{-1} dependence. Data for (acetone)$_n$ (ref. [49]), $(NO)_n$ (ref. [50]) and $(CS_2)_n$ (ref. [51]).

5˙2. Hole trapping. – The formation of the positive ion may result in large intermolecular nuclear configurational changes leading to the formation of a new chemical bond (fig. 6). Such a state of affairs prevails in solid rare gases [45] (table IV), where the vertical formation of a R^+ ion is followed by the production of a stable R_2^+ diatomic ionic molecule, whose binding energy is high (fig. 8). Accordingly, the adiabatic ionization potential of the VdW molecule R_2, whose binding energy is ~ 0.001 eV, is lowered by $\sim D_+$ relative

to the ionization potential of Ar. These local binding effects are reflected in the reduction of the ionization potentials of Ar $(n = 2, 3)$ VdW molecules [36] (fig. 9). For the larger Ar_n $(n = 4 \div 6)$ clusters [36], additional small polarization effects contribute to the cluster stabilization energy.

TABLE IV. – *Bond lengths and dissociation energies for the ground state of the R_2 molecule* (0) *and for the ionic R_2^+ molecule* (+) *(data from ref. [45]).*

	r_0 (Å)	D_0 (eV)	r_+ (Å)	D_+ (eV)
Ar	3.76	0.0012	2.43	0.99
Kr	4.01	0.0017	2.79	1.15
Xe	4.36	0.0024	3.04	0.99
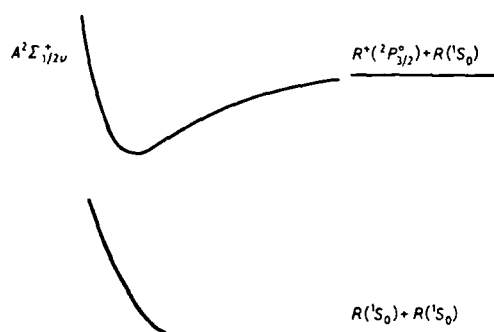
Fig. 8. – Potential curves for R_2 VdW molecules and for R_2^+ diatomic molecular ions.
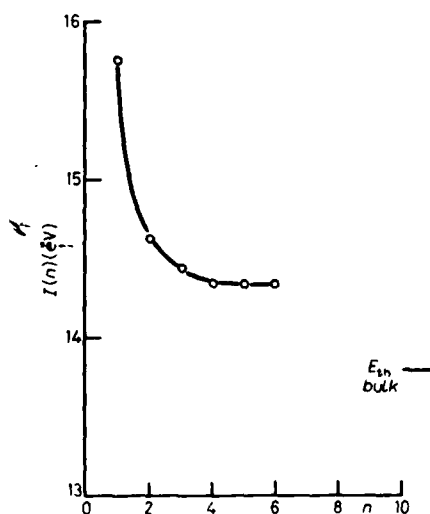
Fig. 9. – Adiabatic ionization potentials of Ar_n $(n = 1 \div 6)$ microclusters (ref. [36]).

5`3. *Destabilization of ionized ionic clusters.* – Removal of an electron from an ionic cluster [9] results in a substantial decrease in the electrostatic Madelung energy. The ionization potential accompanied by the removal of the charge Z_j from the anion located at r_j is [9]

$$(5.4) \qquad\qquad I = \mathrm{EA} + \sum_i \frac{Z_j Z_i}{|r_i - r_j|},$$

where EA is the electron affinity of the anion. Accordingly, the vertical ionization potential of ionic clusters, which is substantially larger than the electron affinity, increases with increasing n (fig. 10). MARTIN [9] has provided numerical
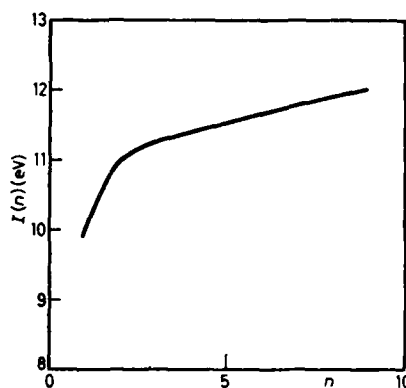
Fig. 10. – Vertical ionization potentials for $(NaCl)_n$ microclusters. (Theoretical data from ref. [9].)

calculations of vertical ionization energies. Furthermore, as pointed out by MARTIN [9], vertical ionization of ionic clusters results in large configurational changes with the cluster relaxing to a new equilibrium configuration.

5`4. *Polarization interactions in ionic Van der Waals* (VdW) *systems.* – The formation of a doped ionic VdW microcluster is accompanied by minor intramolecular and intermolecular configurational changes. The extra stabilization energy of such an ionic microcluster, relative to the corresponding neutral microcluster, originates from charge-induced-dipole polarization interaction. These weak interactions are reflected in the reduction of the ionization potential of the benzene-Ar complex by $\Delta I = -2.5 \cdot 10^{-2}$ eV relative to that of the bare molecule [52], which is in accord with the result $\Delta I = -5 \cdot 10^{-2}$ eV of simple model calculations [53] of these polarization interactions.

6. – Electron localization in clusters.

Electron attachment to clusters falls into two categories:

i) Nonreactive electron attachment, resulting in the formation of a negative cluster which is not accompanied by the breaking of either intermolecular or intramolecular bonds.

ii) Reactive electron attachment, which is accompanied by the breaking of intermolecular or intramolecular bonds.

Regarding the nonreactive electron attachment to clusters, the following issues are of interest:

1) The parentage problem. In many interesting cases the excess electron is attached to a cluster whose individual atomic or molecular constituents do not form a stable negative ion.

2) Localized and extended states of the excess electron. The spatial extent of the electron charge distribution, i.e. the localization length, relative to the cluster size, provides a distinction between localized and extended states in a finite system.

3) Bulk and surface states of the excess electron. The relative energetic stability of these two distinct types of states in different clusters is intriguing.

4) Cluster reorganization. The energetically stable state of the electron attached to the cluster may involve a nuclear configuration which drastically differs from the equilibrium structure of the neutral cluster. In this case electron attachment is accompanied by a large cluster reorganization energy.

5) Cluster isomerization. Electron attachment to a cluster may result in a configurational change resulting in a close-energy isomer.

6) Cluster melting induced by electron attachment. This phenomenon constitutes an extreme case of isomerization.

With regard to reactive electron attachment, the following problems are pertinent:

7) The formation of negative ions accompanying dissociative electron attachment.

8) Cluster dissociation and fission, resulting in the breakage of intermolecular and/or intramolecular bonds.

From the point of view of general methodology, the following issues pertaining to electron localization in clusters are of considerable interest:

9) Quantum phenomena are expected to be pronounced in systems where the electron wavelength is comparable to the cluster size.

10) The excess electron can serve as a probe for the nuclear motion of the cluster.

11) The dynamics of nonreactive and reactive electron attachment will result in novel information regarding the time evolution of electron localization.

Excess electron states in clusters, which are classified in table V, correspond to the following situations.

TABLE V. - *Electron attachment to clusters.*

Type of cluster	Nature of excess electron state	Canonical example	Cause of electron binding
rare gas $(He)_n$	surface state localized	$(He)_n^-$	repulsive + weak polarization
heavy rare gas	bulk state extended (?)	$(Xe)_n^-$	dominated by attractive interactions
Van der Waals	stable negative molecular ion	$(SF_6)_n^-$	large electron affinity of a single molecule
Van der Waals	solvated negative ion	$(CO_2)_n^-$	positive electron affinity of a single molecule stabilization of a negative ion by solvation
H-bonded	solvated electron cluster	$(H_2O)_n^-$ $(n > 6)$ $(NH_3)_n^-$	electron-polar molecule attraction in conjunction with large cluster reorganization
ionic	electron localization in anion vacancies on a surface	$Na_nCl_m^{m-n+1}$	electrostatic interactions

6'1. *Electron attachment to rare-gas clusters.* - It is well known that the electron-helium atom potential is strongly repulsive [54]. Indeed, this short-range repulsive pseudopotential is responsible for the electron bubble formation, both in liquid [55] and in solid [56] helium. In such an infinite system the (positive) energy of the localized excess electron state, which consists of electron kinetic energy together with the bubble surface energy, is lower than the energy of the quasi-free electron state. On the other hand, the repulsive interaction between an electron and a finite He cluster is not expected to result in an energetically stable state of the electron in the bulk of this cluster. Another possible mode of weak binding of the excess electron to a He cluster may involve a surface state. We assert that a surface state of an electron on a

$(\text{He})_n$ cluster is expected to be energetically stable in view of the interplay between the (weak) long-range attractive polarization and the (strong) short-range electron-helium potential. For the heavy rare gases, *i.e.* Ar, Kr and Xe, the long-range attractive polarization potential dominates the short-range repulsive interaction [57]. In clusters of the heavy rare gases, the bulk state of the excess electron, which is extended throughout the cluster, may be energetically stable. Nothing is currently known concerning surface and bulk states of an excess electron in rare-gas clusters.

6˙2. *A stable molecular negative ion.* – A single molecule within the cluster is characterized by a positive electron affinity. The excess electron is bound to a single molecule within the cluster, constituting a stable « solvated » anion. A good candidate for this class of negative clusters will involve $(\text{SF}_6)_n^-$. However, the large electron affinity of molecular SF_6 $(\text{EA} \simeq 5 \text{ eV} [58])$ will lead to appreciable vibrational excitation of the $(\text{SF}_6)_n^-$, following electron attachment, which may result in cluster dissociation.

6˙3. *Stabilization of a negative ion by solvation* $\left(e.g., (\text{CO}_2)_n^- \ (n = 2\div6)\right)$. – The adiabatic electron affinity of a single CO_2 molecule, $\text{EA} = (-0.6\pm0.2) \text{ eV}$ [59], is negative. The most stable nuclear configuration of CO_2^- involves a bent structure [60], which is unstable with respect to $\text{CO}_2 + e$. According to theoretical calculations [60] the electron affinity of the $(\text{CO}_2)_2$ dimer, consisting of a bent CO_2^- « solvated » by a linear CO_2, is positive. This expectation is borne out by the experimental observation of the stable negative $(\text{CO}_2)_2^-$ dimer [40, 41]. This mechanism of electron localization within a single molecule in a cluster involves a large intramolecular configurational change in conjunction with stabilization of the molecular negative ion.

6˙4. *A solvated electron in a cluster of polar molecules* $\left(e.g., (\text{H}_2\text{O})_n^-, (\text{NH}_3)_n^-\right)$. – The solvated electron [61-63] constitutes a bound excess electron state in a polar fluid, where a single molecule is characterized by a negative electron affinity. Extensive theoretical work has established the seminal role of long-range interactions beyond the first co-ordination layer in determining the energetic stability, the electron structure and spectra of the solvated electron in fluids [61-63]. The solvated electron in a cluster involves a spatially extended, large-radius excess electron state, where electron localization is « co-operative », being accompanied by large intermolecular configurational changes. There have been several experimental efforts [42-44, 64] to observe electron attachment to $(\text{H}_2\text{O})_n$ clusters in supersonic beams. Recently, HABERLAND *et al.* [42-44] have reported the observation of $(\text{H}_2\text{O})_n^-$ and $(\text{D}_2\text{O})_n^-$ $(n>11)$ solvated electron in water clusters and $(\text{NH}_3)_n^-$ $(n>32)$ for electron solvation in ammonia clusters.

Recent theoretical efforts were directed towards the elucidation of the energetic stability of the localized electron state in $(\text{H}_2\text{O})_n$ $(n = 4\div8)$ clusters.

KESTNER et al. [65, 66] have evaluated the energetic stability of $(H_2O)_n^-$ clusters by combining the results of self-consistent-field-configuration-interaction quantum-mechanical calculations of the binding energy of an electron in an optional nuclear configuration of $(H_2O)_n$ clusters together with the energy required to form various water clusters. The binding energy of the excess electron was calculated by RAO and KESTNER [65] using a SCF programme and the 4-31 G Gaussian basis set of Newton [63]. The nuclear configuration of the cluster was optimized to minimize the binding energy of the excess electron. The binding energies of various water clusters were obtained using the polarization model of Stillinger et al. [67]. The total energetic change accompanying the process

(6.1) $nH_2O + e \rightarrow (H_2O)_n^-$,
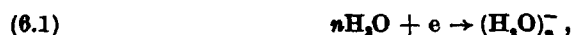
which corresponds to the net stability of the negative cluster relative to a free electron and separated water molecules [65, 66], is presented in fig. 11. From these results it is apparent that:
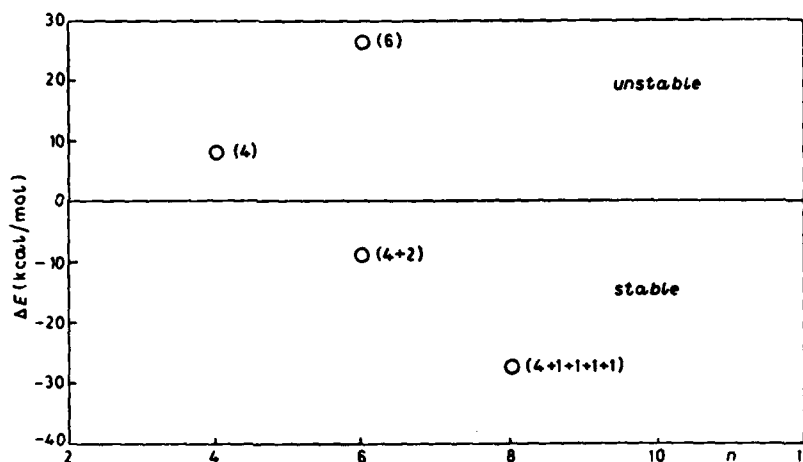
Fig. 11. – Energy change accompanying reaction (6.1). The clusters are labelled in terms of the first co-ordination layer plus the second layer (ref. [65, 66]).

a) The clusters $(H_2O)_n^-$ containing four and six water molecules in the first co-ordination layer, respectively, are unstable with respect to reaction (6.1).

b) $(H_2O)_n$ clusters with $n > 6$, which contain at least one water molecule in the second co-ordination layer, are stable with respect to the separate molecules and the free electron.

c) Interactions beyond the first co-ordination layer are essential for the localization of an excess electron in a cluster. These interactions are

analogous to the «long-range» electron-medium interaction in the dense fluid.

The optimal nuclear configurations of the $(H_2O)_n^-$ negative clusters are drastically different from the equilibrium nuclear configurations of the neutral $(H_2O)_n^{(eq)}$ clusters. The orientational effects induced by the presence of the excess electron are severe and result in considerable weakening of the hydrogen bonding. To demonstrate the consequences of the structural distortion of the normal neutral water cluster, KESTNER and JORTNER [66] have calculated the cluster reorganization energy, *i.e.* the energy required to transform the equilibrium water cluster into the optimal structure, which accommodates the excess electron. The energetic changes for the process

$$(6.2) \qquad\qquad (H_2O)_n^{(eq)} + e \rightarrow (H_2O)_n^-$$

are summarized in fig. 12. From these results it is apparent that:
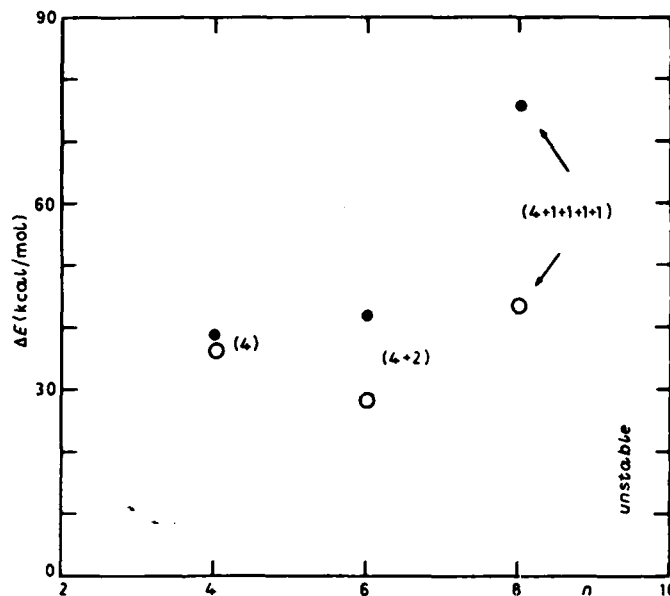
Fig. 12. – Energy change accompanying reaction (6.2) and cluster reorganization energies: o $(H_2O)_n^{(eq)} + e \rightarrow (H_2O)_n^-$, • $(H_2O)_n^{(eq)} \rightarrow (H_2O)_n$. Notation same as in fig. 11 (ref. [65, 66]).

d) The cluster reorganization energy is sizable, *i.e.* (1.5÷3.5) eV for $n = 4 \div 8$, exceeding the quantum binding energy of the excess electron to the cluster.

e) All the $(H_2O)_n^-$ clusters studied by KESTNER *et al.* [65, 66] are unstable with respect to reaction (6.2). One can assert that the equilibrium $(H_2O)_n^{(eq)}$ ($n = 4\div8$) clusters have a negative electron affinity.

f) An excess electron will not bind to a pre-existing, stable, equilibrium water cluster at 0 K.

g) Metastable $(H_2O)_n$ ($n>6$) neutral water clusters are required for the initial localization of an excess electron at low temperatures. Such negative small clusters once formed can subsequently attach additional water molecules.

What is the formation mechanism of $(H_2O)_n^-$ ($n>11$) clusters in super-sonic beams, which were observed by HABERLAND *et al.*? Two mechanisms come to mind. The first mechanism involves electron attachment to small ($n>6$) metastable water clusters followed by nucleation of additional water molecules on the initially formed negative cluster. The second possible mecha-nism rests on the notion that the water clusters formed in supersonic jets may be quite hot [68]. At high temperatures the cluster may undergo isomeriza-tion between several equilibrium nuclear configurations. The calculations of Kestner *et al.* [65, 66] provide information on the energies of the two minima of the potential hypersurface of the system, which correspond to $(H_2O)_n^{(eq)} + e$ and to $(H_2O)_n^-$, respectively. It is plausible to assume that these two minima are separeted by a barrier. An artist's view of the potential hyper-surface of the system is portrayed in fig. 13. Isomerization occurring at finite
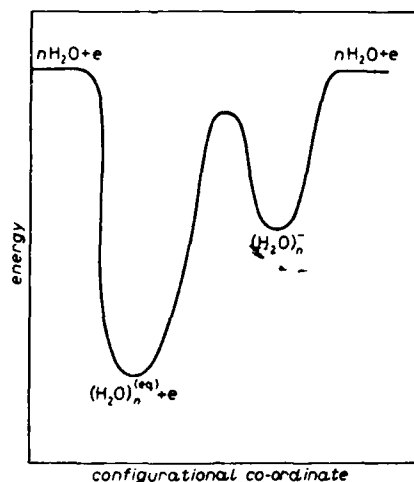
Fig. 13. – A schematic representation of the potential hypersurface for $nH_2O + e$. Only the energies of the two minima were calculated. The height of the barrier is un-known.

temperatures will result in the population of the energetically unfavourable $(H_2O)_n^-$ structure. This isomerization process at finite temperatures bears a close analogy to the dynamic description of the melting process of micro-clusters. The mechanism of attachment of an excess electron to a hot water microcluster may be promoted by structural modification due to the melting of the cluster.

6`5. *Electron localization in alkali halide clusters*. – The structure, energetics and dynamics of electron alkali halide clusters is of considerable interest with regard to the mechanisms and the localization modes of electron attachment. Recently, the theory of the compositional, structural and size dependence of various electron localization modes has been explored, providing novel information on bulk and surface states, nonreactive and reactive electron localization, configurational modifications and isomerization induced by electron localization in an alkali halide cluster (AHC) [69]. Apart from the intrinsic interest in these systems, the AHC was chosen because of three technical reasons. Firstly, the nature of interionic interactions in these clusters is well understood. Secondly, there exists an abundance of model calculations on both neutral and charged AHCs. Thirdly, quite extensive information is available on electron-alkali cation (M^+) and electron-halide anion (X^-) interactions. The structure, energetics and dynamics of e-AHC have been explored using the quantum path integral molecular-dynamics (QUPID) method. This approach, which rests on a discrete version of Feynman's path integral method [70-76], provides a powerful method for the study of these systems. In this scheme the quantum problem is isomorphic to an appropriate classical problem, with the excess electron being mapped onto a closed flexible polymer of P points. The isomorphism becomes exact as $P \to \infty$. The practical applicability of the computational method rests on the development of numerical algorithms, which achieve convergence with manageable values of P. From the point of view of general methodology, the QUPID method rests on the application of computers for the simulations of the properties of complex systems. The general philosophy underlying such an approach was initiated thirty years ago by FERMI, ULAM and PASTA [77] with the advent of the first generation of computers, when FERMI suggested to employ computers for the exploration of the dynamics of nonlinear systems. A recent seminal accomplishment of these techniques involves the applications of renormalization group theory to condensed-matter and particle physics [78].

The QUPID method was applied to a system of an electron interacting with an AHC, which is specified by the Hamiltonian

(6.3) $H = -(\hbar^2/2m)\nabla^2 + V_e(r)$,

with $V_e(r)$ being the e-AHC potential. The partition function for such a

system is

(6.4) $Z = \text{Tr} \left[\exp \left[-\beta H \right] \right]$,

where $\beta = 1/kT$ is the inverse temperature, while the energy of the system is

(6.5) $E = -\dfrac{\partial}{\partial \beta} \ln Z$.

The quantum-mechanical classical isomorphism is established by the factorization of the partition function

(6.6) $Z = \text{Tr} \left[\exp \left[-\beta H/P \right] \right]^P$.

By inserting P complete sets of states, one obtains the formally exact result

(6.7) $Z = \displaystyle\int d\boldsymbol{r}_1 \dots d\boldsymbol{r}_P \, \langle \boldsymbol{r}_1 | \exp \left[-\beta H/P \right] | \boldsymbol{r}_2 \rangle \dots \langle \boldsymbol{r}_P | \exp \left[-\beta H/P \right] | \boldsymbol{r}_1 \rangle$.

To proceed further, one can invoke the high-temperature, i.e. small β/P, expansion for the matrix elements

(6.8) $\langle \boldsymbol{r}_1 | \exp \left[-\beta H/P \right] | \boldsymbol{r}_2 \rangle \simeq (Pm/2\pi\hbar^2\beta)^{\frac{1}{2}} \cdot$

$\cdot \exp \left[-Pm(\boldsymbol{r}_1 - \boldsymbol{r}_2)^2/2\hbar^2\beta \right] \exp \left[-\beta[V_s(\boldsymbol{r}_1) + V_s(\boldsymbol{r}_2)]/2P \right]$,

which constitutes a product of a free-particle propagator at β/P and a potential-energy contribution. From eqs. (6.7) and (6.8) one obtains for Z the approximate expression

(6.9) $Z \simeq (Pm/2\pi\hbar^2\beta)^{3P/2} \displaystyle\int d\boldsymbol{r}_1 \dots d\boldsymbol{r}_P \, \exp \left[-\beta V_{\text{eff}}(\boldsymbol{r}_1 \dots \boldsymbol{r}_P) \right]$,

where the effective potential is

(6.10) $V_{\text{eff}} = \displaystyle\sum_{i=1}^{P} \left[\dfrac{Pm}{2\hbar^2\beta^2} (\boldsymbol{r}_i - \boldsymbol{r}_{i+1})^2 + \dfrac{1}{P} V_s(\boldsymbol{r}_i) \right]$,

consisting of a superposition of a harmonic potential and the cluster potential. We note in passing that, when the thermal wavelength

(6.11) $\lambda_T = (\beta\hbar^2/m)^{\frac{1}{2}}$

is considerably smaller than any relevant length scale, the Gaussian factors in eqs. (6.8) and (6.9) reduce to a delta-function, whereupon the classical description of the system is regained.

Equations (6.9) and (6.10) establish an approximate isomorphism between the quantum problem characterized by the Hamiltonian H, eq. (6.3), and the classical problem defined by the effective potential, eq. (6.10). In this isomorphism the quantum particle is mapped onto a closed polymer, which is also referred to as a necklace, of P pseudoparticles (beads). Each point of the necklace exerts two types of interactions (fig. 14), that is, i) nearest-
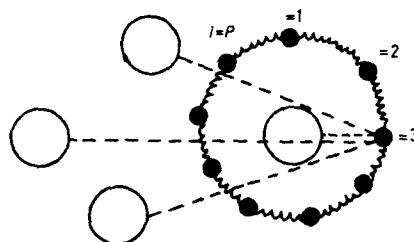

Fig. 14. – A schematic representation of the electron necklace: ⌇⌇ harmonic pseudo-interactions, – – – contributions to e-AHC potential, ○ classical ions, ● points of necklace.

neighbour interactions between the beads in the chain, which are chatacterized by a harmonic potential with a force constant $Pm/\hbar^2\beta^2$, and ii) interactions with the AHC through the scaled potential $V_e(r)/P$.

At this stage it will be convenient to provide an explicit description of the e-AHC system. The AHC, which is treated as a classical system, consists of N ions (N_1 cations and N_2 anions) with masses M_1 and M_2, respectively. The interionic potential within the AHC is

$$(6.12) \qquad V_{AHC} = \sum_I \sum_{I\neq J} \Phi_{IJ}(R_{IJ})$$

with the interionic potential $\Phi_{IJ}(R_{IJ})$ being given by the Born-Meyer potential [79]. The e-AHC potential is

$$(6.13) \qquad V_e(r) = \sum_I \varphi_{eI}(r - R_I) ,$$

consisting of a sum of electron-ion potentials, which are described by a purely repulsive pseudopotential

$$(6.14) \qquad \varphi_{eI}(r) = e^2/r$$

for electron-anion interaction and by the local pseudopotential [80]

$$(6.15) \qquad \begin{cases} \Phi_{eI}(r) = -e^2/R_e , & r < R_e , \\ \Phi_{eI}(r) = -e^2/r , & r > R_e , \end{cases}$$

for the electron-cation interactions. The average energy of the system is now given from eqs. (6.5) and (6.9) in the explicit form [73]

$$(6.16) \qquad E = 3N/2\beta + \langle V_{AHC} \rangle + KE + P^{-1} \left\langle \sum_{i=1}^{P} V_e(r_i) \right\rangle .$$

The first two terms in eq. (6.16) correspond to the kinetic and potential energies of the classical AHC system, respectively. The electron kinetic energy is [75]

$$(6.17) \qquad KE = 3/2\beta + \sum_{i=1}^{P} \langle \partial V_e(r_i)/\partial r_i \cdot (r_i - r_p) \rangle /2P ,$$

consisting of a free-particle term, $3/2\beta$, and the contribution, K_{int}, from the interaction with the ions [75]. The indicated statistical averages $\langle \rangle$ are over the Boltzmann distributions as defined in eq. (6.9). This formalism is converted into a numerical algorithm by noting [76] the equivalence of the sampling described above to that over phase-space trajectories generated via molecular dynamics by the classical Hamiltonian

$$(6.18) \quad H = \sum_{i=1}^{P} m^* \dot{r}_i^2/2 + \sum_{I=1}^{N} M_I \dot{R}_I^2/2 +$$
$$+ \sum_{i=1}^{P} [Pm(r_i - r_{i+1})^2/2\hbar^2\beta^2 + V_e(r_i)/P] + V_{AHC} ,$$

the mass m^* being arbitrary [76] and taken as $m^* = 1$ a.m.u.

Numerical simulations were performed for an electron interacting with sodium chloride clusters. Based upon the examination of the stability of the variance of the kinetic-energy contribution K_{int}, the number of «electron beads» was taken as $P = 399$. Employing an integration step of $\Delta t = 1.03 \cdot 10^{-16}$ s, long equilibration runs were performed $((1 \div 2) \cdot 10^4 \Delta t)$. The reported results were obtained via averaging over $8 \cdot 10^3 \Delta t$ following equilibration. The temperature of the system was $T = 300$ K. The electron-cation pseudopotential parameters were varied by changing the cut-off radius R_e in eq. (6.15). A typical value chosen for Na$^+$ was $R_e = 3.22\ a_0$ [69]. Weaker electron-cation interactions, which are appropriate for heavier cations, were mimicked by increasing the value of R_e.

Structural [9] and classical molecular-dynamics [10] calculations have established that, when the size of the ionic cluster increases ($N > 20$), the NaCl crystallographic arrangement is energetically preferred even if the number of positive and negative ions is not equal. We have chosen [69] to study first the interaction of an electron with the positive clusters [Na$_{14}$Cl$_{13}$]$^+$ and [Na$_{14}$Cl$_{12}$]$^{++}$, which exhibit the crystallographic structure without and with a vacancy, respectively (fig. 15), and which are characterized by a pronounced energetic stability. In fig. 16 and 17 we present our results for the equilibrium
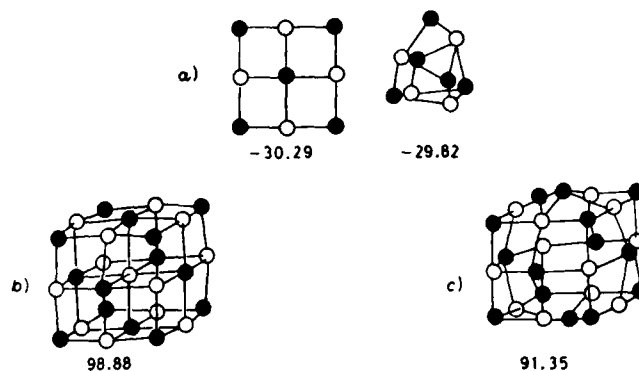
Fig. 15. – Configurations of some small and large NaCl clusters to which an excess electron was attached (ref. [9, 10]): a) $Na_8Cl_4^+$, b) $Na_{14}Cl_{13}^+$, c) $Na_{14}Cl_{12}^{++}$. The numbers refer to the ground-state energies in eV units.
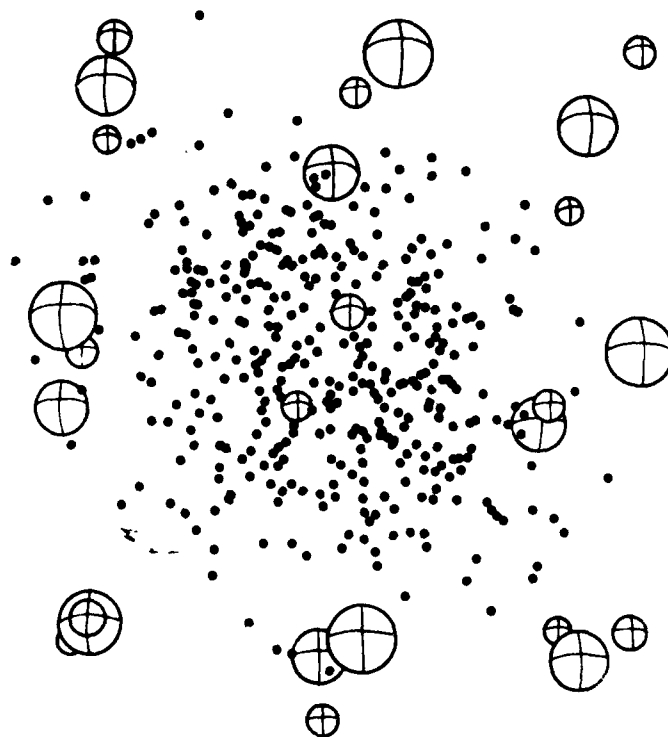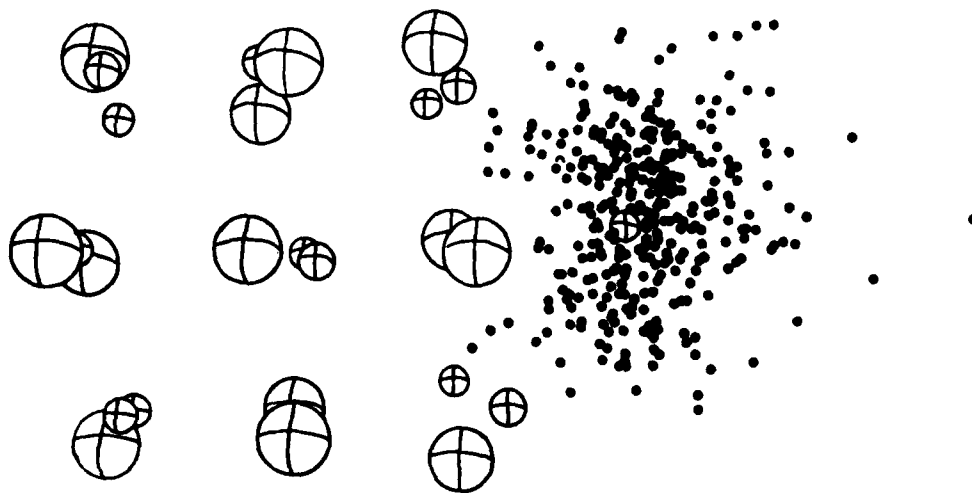

Fig. 16. – Ionic configurations and «electron necklace» distributions for an excess electron interacting with a $Na_{14}Cl_{12}^{++}$ cluster ($R_s = 3.22$ a.u.). Small and large spheres correspond to Na^+ and Cl^- ions, respectively. Dots represent 2-D projection of the «electron beads». Note electron localization in an anion vacancy (ref. [69]).

Fig. 17. – Ionic configuration and «electron necklace» distribution for an excess electron interacting with $Na_{14}Cl_{13}^+$ cluster ($R_s = 3.22$ a.u.). Note electron localization in a (compact) surface state (ref. [69]).

charge distribution obtained [69] from two-dimensional projections of the necklace edge points, and for the nuclear configuration of the clusters. The energetics of these systems are summarized in table VI, where the electron affinity, E_A, of the cluster

(6.19) $$E_A = E_B^o + E_o$$

is obtained by summing the electron binding energy

(6.20) $$E_B^o = 3/2\beta + K_{int} + P^{-1} \sum_{i=1}^{P} \langle V_e(r_i) \rangle$$

and the cluster reorganization energy

(6.21) $$E_o = \langle V_{AHC} \rangle - \langle V_{AHC} \rangle_o ,$$

where $\langle V_{AHC} \rangle_o$ is the potential energy of the «bare» AHC in the absence of the electron. As is apparent from fig. 16, the $[Na_{14} Cl_{13}]^{++}$ cluster stabilizes an internally localized excess electron state. The features of internal electron localization are:

1) It occurs in a moderately large cluster.

2) An anion vacancy is required.

TABLE VI. – *Average equilibrium temperature* ($\langle T \rangle$), *interionic cluster potential energy* ($\langle V_{AHO} \rangle$), *electron interaction kinetic energy* (K_{int}), *electron kinetic energy* KE $= 3/2\beta +$ $+ K_{int}$, *e-AHC interaction potential energy* ($\langle V_e \rangle$), *electron binding* (E_B^o), *cluster reorganization energy* (E_o), *electron affinity of cluster* (E_A) *and Cartesian components of the « electron necklace » gyration radii* (R_x^2, R_y^2, R_z^2). *Atomic units are used (energy in hartree, length in Bohr radii). Variances are given in parentheses.*

	$\langle T \rangle$ $(\cdot 10^3)$	$\langle V_{AHO} \rangle$	K_{int} $(\cdot 10^2)$	KE	$\langle V_e \rangle$
e-[Na$_{14}$Cl$_{12}$]$^+$ $R_e = 3.22$	0.983 (0.035)	-3.4856	6.4195 (0.633)	0.0657	-0.2251
e-[Na$_{14}$Cl$_{12}$]$^{++}$ $R_e = 3.22$	0.938 (0.028)	-3.2372	7.2203 (0.767)	0.0736	-0.3226
e-[Na$_6$Cl$_4$]$^+$ $R_e = 3.22$	0.950 (0.132)	-1.0059	2.6389 (0.582)	0.0278	-0.3012
e-[Na$_6$Cl$_4$]$^+$ $R_e = 4.36$	0.946 (0.038)	-1.0483	3.5453 (0.601)	0.0369	-0.1876

	E_B^o	E_o	E_A	R_x^2	R_y^2	R_z^2
e-[Na$_{14}$Cl$_{12}$]$^+$ $R_e = 3.22$	-0.1594	0.1055	-0.0539	5.4	7.0	9.8
e-[Na$_{14}$Cl$_{12}$]$^{++}$ $R_e = 3.22$	-0.2490	0.0799	-0.1691	4.6	6.8	6.3
e-[Na$_6$Cl$_4$]$^+$ $R_e = 3.22$	-0.2734	0.0940	-0.1794	2.2	2.0	2.5
e-[Na$_6$Cl$_4$]$^+$ $R_e = 4.36$	-0.1508	0.0516	-0.0992	5.7	7.2	5.5

3) The localized electron state is surrounded by Na$^+$ ions in an octahedral configuration and by twelve Cl$^-$ ions.

4) The ionic configuration is somewhat distorted.

5) The gain in E_B^o exceeds the loss in E_o, i.e. $E_B^o + E_o < 0$, which favours localization.

6) The total energy of e-[Na$_{14}$Cl$_{12}$]$^{++}$ is close to that of [Na$_{14}$Cl$_{12}$]$^+$, whereupon the electron (internal) binding energy in the cluster is similar to that of a negative ion.

7) These results establish the dominance of short-range attractive interactions for internal electron localization.

8) A measure of the spatial extent of the localized electron is given by

the gyration radius of the electron necklace

$$(6.22) \qquad R^2 = (1/2\,P^2)\left\langle \sum_i \sum_j (r_i - r_j)^2 \right\rangle$$

whose components (table VI) assume the values $(5 \div 10)\,a_0^2$. The thermal wavelength of a free electron at $T = 300$ K is $R_T = 56\,a_0$. Accordingly, for the internal excess electron state $R \ll R_T$, demonstrating enhanced localization.

A drastically different localization mode is obtained in the $[Na_{14}Cl_{13}]^+$ system (fig. 17), where a novel surface state is exhibited. We refer [69] to this state as a cluster surface localized state. Such surface states were considered for macroscopic alkali halide crystals by TAMM [81] about fifty years ago, but were never experimentally documented. The characteristics of external localization of an electron on a NaCl cluster are:

a) It is exhibited in a vacancy-free moderately large AHC.

b) In such an AHC internal localization is prohibited by a large value of E_s.

c) The excess electron in $[Na_{14}Cl_{13}]^+$ localizes around Na^+ surface ions leaving a neutral $Na_{13}Cl_{13}$ cluster interacting with a partially neutralized Na atom.

d) In this system a surface localized electron state is exhibited.

e) For clusters containing heavier M^+ ions, the surface state will become more extended.

f) The excess electron surface state is expected to be exhibited also in moderately large neutral AHCs.

In smaller clusters novel effects of dissociative electron attachment and cluster isomerization induced by electron localization were manifested [69]. We have studied the smallest single ionized cluster exhibiting high stability, i.e. $[Na_5Cl_4]^+$, for which the lowest-energy configuration is planar with four Na^+ ions at the corners and one at the centre of an approximate square (fig. 15). This cluster possesses an isomeric structure (less stable by 0.014 a.u.) in which the ions are arranged in a distorted pyramidal configuration [9, 10]. Adding an electron to the planar ground state, the configuration of $[Na_5Cl_4]^+$ (with the Na^+ pseudopotential being characterized by $R_c = 3.22\,a_0$) transforms the system into a neutral $[Na_4Cl_4]$ cluster with a planar ring structure and a dissociated neutral Na atom (table VI and fig. 18) corresponding to the initial- and final-state configurations, respectively. To demonstrate that this process is driven by the localization of e around a single Na^+ ion, we have decreased the cation-electron binding strength, taking $R_c = 4.36\,a_0$ [69]. In this case,

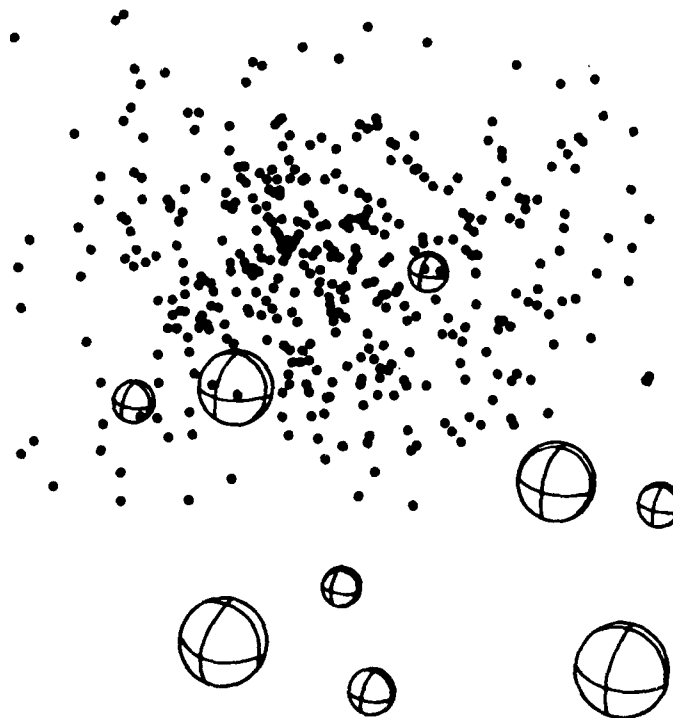Fig. 18. – Ionic configuration and «electron necklace» distribution for an excess electron interacting with $Na_4Cl_4^+$ cluster and resulting in dissociation detachment (ref. [69]).

extreme localization is not sufficiently counterbalanced by e-binding. Instead, the planar structure transforms to the isomeric pyramidal configuration with the electron localized as a diffuse cloud about the tip of the pyramid (fig. 19). Electron localization accompanied by structural isomerization will contitute a prevalent phenomenon for AHC with smaller e-cation binding energy, *i.e.* the heavier alkali metals. In view of the intimate interrelationship between structural isomerization and melting of clusters, it will be interesting to explore the melting of such finite systems induced by electron localization. To summarize, recent QUPID calculations [69] establish four modes of localization of an excess electron in AHC: i) An F-centre defect with the excess electron replacing an internal halide ion. ii) A new surface state, *i.e.* a «surface F-centre» of the excess electron. iii) Dissociative electron attachment to AHC resulting in the formation of an «isolated» alkali atom. iv) Structural isomerization induced by electron attachment. These calculations [69] established the compositional, structural and size dependence of these various localization mechanisms in these interesting systems.

Fig. 19. - Ionic configuration and «electron necklace» distribution for an excess electron interacting with a model $Na_nCl_n^+$ cluster with $R_e = 4.36$ a.u. Electron attachment results in cluster isomerization (ref. [69]).

7. - Dynamic processes in clusters.

From the foregoing study of the dissociation and isomerization of small alkali halide clusters (AHCs) induced by electron attachment, some interesting information has emerged regarding dynamic processes in microclusters. However, this energetic and structural information pertains to the behaviour of the system at $t \to \infty$. In other words, these time-independent data provide information on the decay channels of these systems. Of considerable interest is the temporal dynamics in clusters, which will provide the time scales for various processes of energy storage and disposal in these systems. In this context, an important issue involves the dynamic consequences of vibrational excitation of microclusters. Such relaxation processes fall into two categories: i) nonreactive relaxation, which does not result in dissociation, and ii) reactive dissociative relaxation. In what follows we shall consider some reactive relaxation processes in vibrationally excited Van der Waals and hydrogen-

bonded microclusters. The mechanism of vibrational-energy acquisition by the microcluster can involve collisional excitation, optical photoselective vibrational excitation or degradation of electronic energy into vibrational energy. The following processes are of interest.

7'1. Vibrational predissociation (VP)

(7.1) $$A_n \xrightarrow{\text{vt}} A_n^* \xrightarrow{\text{vt}} A_{n-1} + A .$$

Relevant information originates from molecular-dynamics computer simulations for Ar_n ($n = 4\div6$) clusters [82] and from experimental molecular-beam studies of hydrogen-bonded $(HF)_n$ ($n = 2\div6$) and (H_2O) ($n = 2\div6$) clusters [83]. The numerical results for classical trajectory calculations of Ar_n ($n = 4\div6$) microclusters can be accounted for in terms of the statistical theory of unimolecular reactions, which implies the occurrence of complete vibrational-energy redistribution [84]. The dependence of the VP rates, k, on the excess vibrational energy E_v can quantitatively be fitted by the classical RRK formula [85]

(7.2) $$k = A \left(\frac{E_v - E_t}{E_v}\right)^{s-1},$$

where E_t is the threshold energy, the pre-exponential factor $A = (10^{12}\div10^{13})$ s^{-1} corresponds to a vibrational frequency of an ordinary vibration, while the number of vibrational degrees of freedom is $s = 3n - 6$ [82]. This analysis of the VP dynamics of Ar_n ($n = 4\div6$) clusters in terms of a statistical theory is of considerable interest because of two reasons. Firstly, vibrational-energy randomization presumably occurs in small Ar_n clusters. Secondly, the quantitative fit of the VP dynamics in terms of the classical RRK theory with the exact value of s is unique. The experimental data for hydrogen-bonded microclusters [83] yield a lower limit for the VP rate $k > 10^6$ s^{-1} at $E_v \approx 3000$ cm^{-1} and do not as yet provide information on the interesting issue of intramolecular vibrational-energy redistribution and the applicability of statistical theories in these clusters.

7'2. Vibrational predissociation induced by exciton trapping.

 – Electronic excitation of a rare-gas cluster, E_n, results in an exciton state, which subsequently becomes trapped by self-localization. The details of the energetics and the spatial charge distribution of excitons in finite rare-gas clusters (RGC) have not yet been explored. Nevertheless, the two lowest «intermediate» exciton states in RGC can adequately be described in terms of tightly bound Frenkel-type excitation with a parentage in the $^1S_0 \to {}^3P_1$ and $^1S_0 \to {}^1P_1$ atomic excitations, which are modified by large nonorthogonality corrections [86]. The energetic separation between these two excitons corresponds

to the spin-orbit splitting [86]. This description of the electronic excitations
rests on a decidedly molecular description. An analogous molecular point
of view [86] is adopted for the description of exciton trapping in RGC. The
process of exciton trapping in the heavy RGC of Ar, Kr and Xe involves the
formation of the diatomic excimer molecule R_2^* at a highly vibrational state.
The energetics of R_2^* molecules is summarized in table VII. These diatomic

TABLE VII. – *Energetic parameters and band distances for the heavy rare-gas excimers*
(ref. [45]).

	r_e (Å)	D_e (eV)
Ar	2.42	0.68
Xe	3.04	0.79

molecules are characterized by substantial binding energies at short inter-
nuclear distances (fig. 20). Energy exchange between the R_2^* excimer and the
cluster in which it is embedded involves two processes.
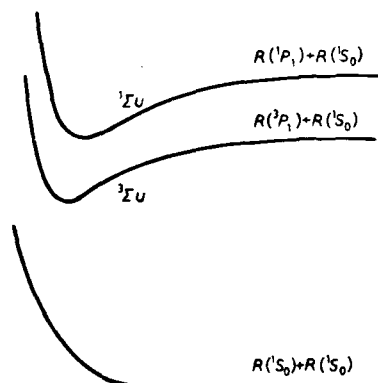
Fig. 20. – Potential curve for the formation of R_2^* electronically excited diatomic
rare-gas molecule.

1) Short-range repulsive interactions between the expanded, Rydberg-
type excited state of the excimer and the other cluster atoms result in a dila-
tion of the local structure around the excimer, leading to energy flow into
the cluster.

2) Vibrational relaxation of the excimer induces vibrational-energy flow
into the cluster.

The vibrational energy released into the cluster by processes 1) and 2)
may result in vibrational predissociation.

No experimental information is currently available concerning the dynamic implications of exciton trapping in RGC. We have conducted [87] classical molecular-dynamics calculations on electronically excited states of such clusters, which constitute an application of this technique for the dynamics of electronically excited states. As a model system we have chosen the Ar_{13} cluster (fig. 1), which in its ground state is characterized by Lennard-Jones pair potentials, specified by the energy ε and distance σ. To achieve an electronic excitation (at $t = 0$) within the framework of the classical description, the nuclear configuration is frozen as is appropriate for the ground electronic state (fig. 21). The electronic excitation is characterized by switching on at
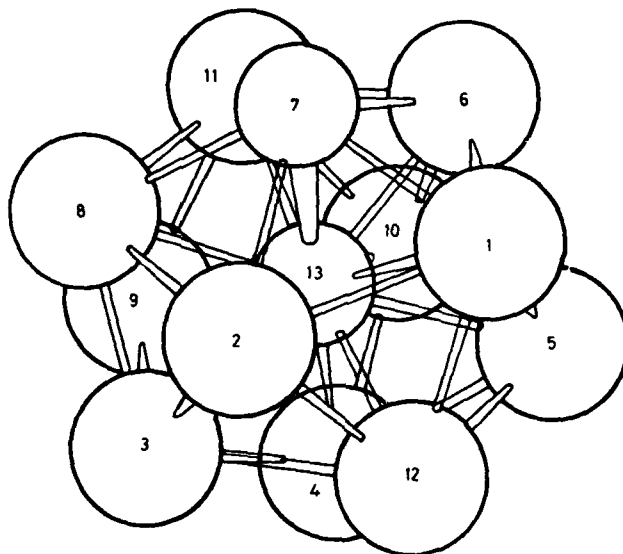
Fig. 21. – An artist's view of the electronic excitation of an excimer in the $(Ar)_{13}$ cluster.

$t = 0$ the molecular excimer potential, charaterized by the parameters of table VII, between a pair of atoms. We have adopted a local picture, disregarding the effects of electronic energy transfer within the cluster. Another important consequence of the electronic excitation involves the intermolecular potential between the excimer and the ground-state atoms. This excimer-cluster potential has been described in terms of atom-atom potentials. On the basis of the analysis of Xe^*-Ar interactions [88], the Ar^*-Ar potential for each of the constituents of the excimer has been described in terms of a Lennard-Jones potential with the parameters ε^* and σ^*. We have taken for the energy $\varepsilon^* = \varepsilon$, while the distance scale ratio $\bar{\sigma} = \sigma^*/\sigma$ has been chosen in the range $\bar{\sigma} = 1.0 \div 1.2$ [88], reflecting the enhancement of short-range

repulsive interactions in the electronically excited state. An overview of the
dynamics of nuclear motion, which is expressed in terms of the time dependence
of the interatomic distances, is shown in fig. 22 and 23. The excimer exhibits
a large-amplitude motion in a highly excited vibrational state, while all the
other interatomic distances increase, indicating the initiation of escape of
the ground-state cluster atoms. Insight into the energy flow from the dimer
into the cluster is exhibited in fig. 24 and 25, which show the time dependence
of the kinetic energy (KE), the potential energy (PE) and the total energy
of the excimer. The strong oscillations in the PE and KE clearly indicate
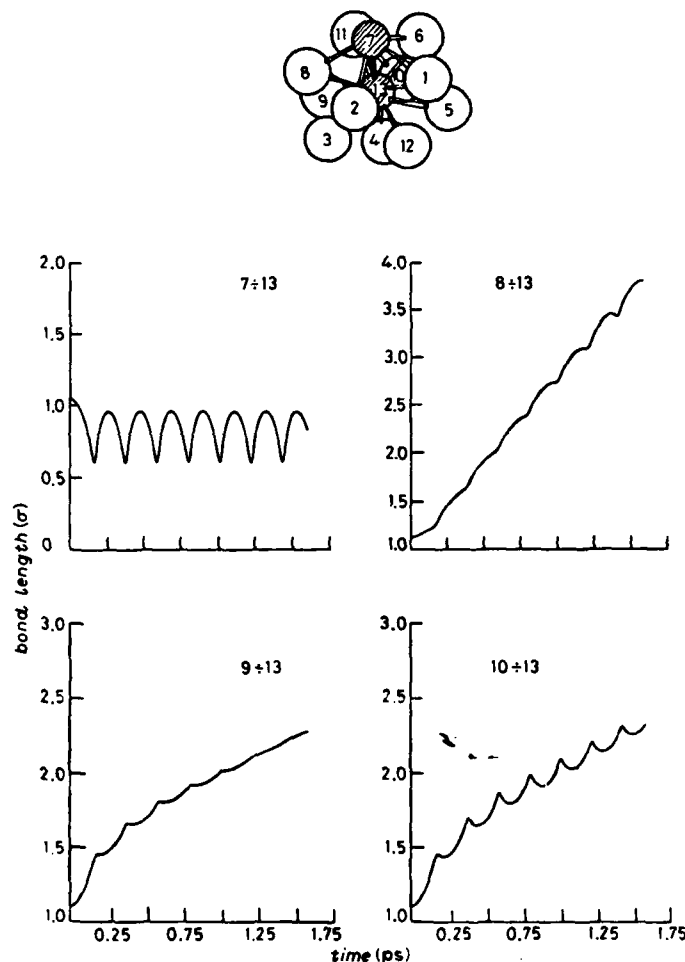
Fig. 22. – Time dependence of interatomic distances in the electronically excited
$(Ar)_{13}$ cluster ($\delta = 1.2$). Note the oscillating large-amplitude motion of the excimer
(ref .[87]).
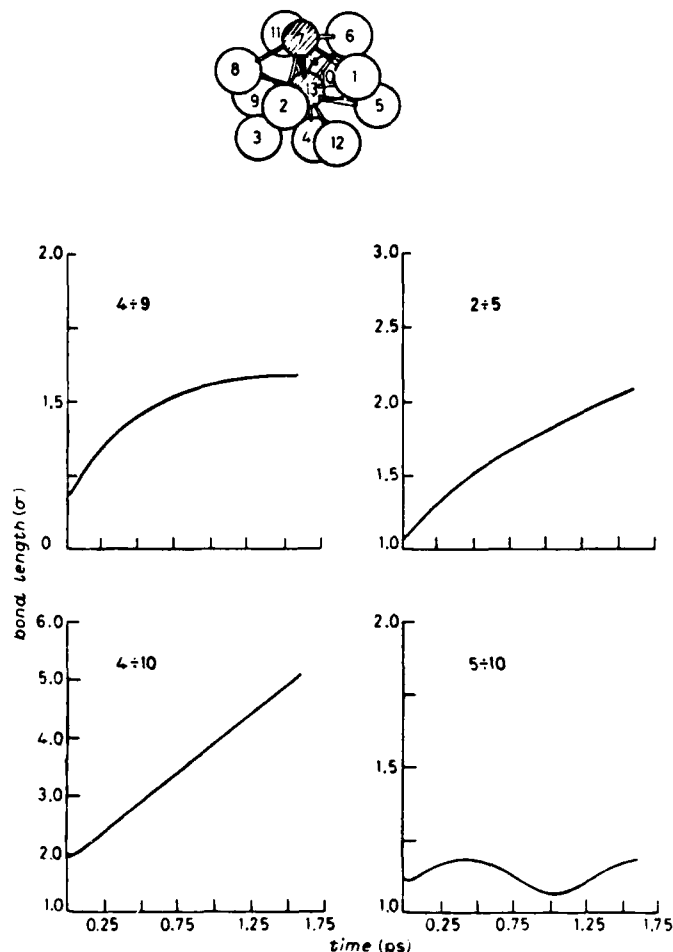
Fig. 23. – Time dependence of interatomic distances between ground-state atoms in the electronically excited $(Ar)_{13}$ cluster $(\delta = 1.2)$. Note the monotonic increase in the distances (ref. [87]).

the persistence of the vibrational excitation of the excimer over a long time scale. This situation corresponds to a « mode selective » excitation of the local motion of the excimer, with vibrational-energy redistribution being precluded by two effects. First, the difference in the characteristic frequencies of the (high-frequency) dimer motion and the (low-frequency) motion of the cluster. Second, the local dilation of the cluster structure around the excimer, which is induced by the short-range excimer-cluster repulsive interactions. The vibrational-energy flow from the dimer into the cluster (fig. 25) consists of two
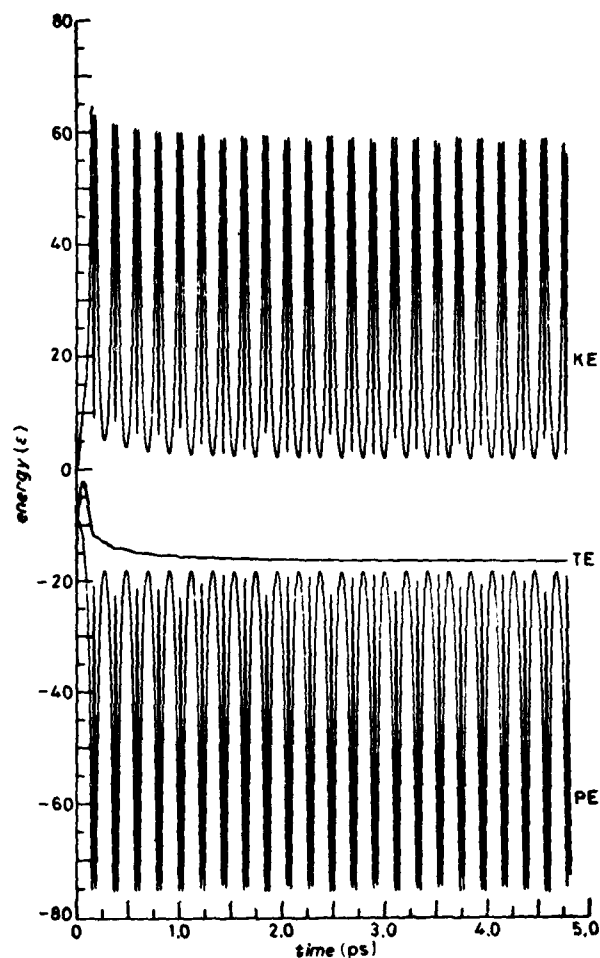
Fig. 24. – Time dependence of the potential energy (PE), the kinetic energy (KE) and the total energy (TE) of the excimer in $(Ar)_{13}$ ($\bar{\sigma} = 1.20$). Data from ref. [87]).

stages. i) Ultrafast energy transfer due to repulsion, which occurs on the time scale of 200 fs. This energy transfer process is dominated by the magnitude of the scale parameter $\bar{\sigma}$. ii) «Slow» energy transfer on the time scale of tens of picoseconds (for $\bar{\sigma} = 1.2$) and hundreds of picoseconds (for $\bar{\sigma} = 1.0$) due to vibrational relaxation of the excimer. The dynamics of the cluster induced by these energy transfer processes involves reactive vibrational predissociation. This state of affairs is, of course, drastically different from that encountered in infinite systems, where a nonreactive process prevails when the phonon modes of the system are excited. Figure 26 shows model calculations (with
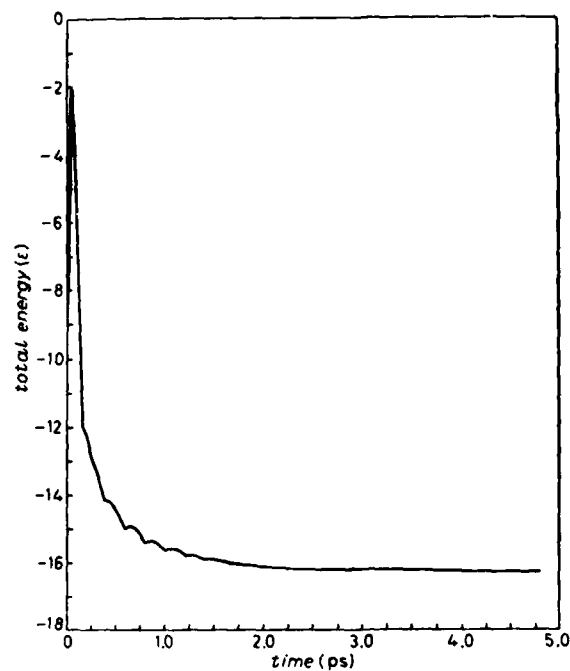
Fig. 25. – Time dependence of total energy of the excimer in $(Ar)_{13}$ ($\bar{\sigma} = 1.20$). Data from ref. [87].
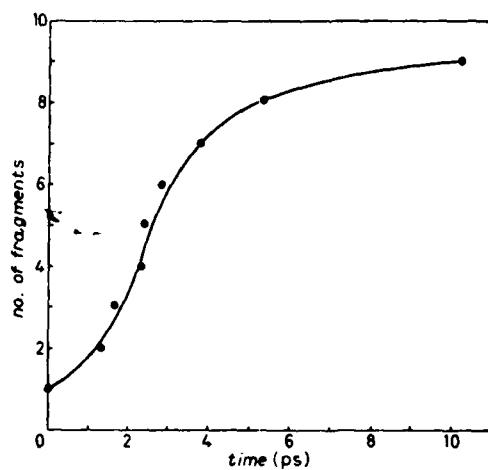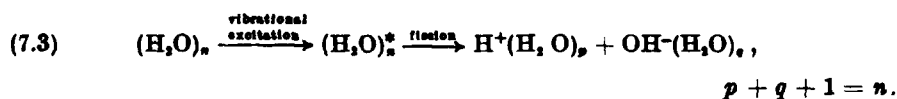

Fig. 26. – The time evolution of the fragmentation of the electronically excited $(Ar)_{13}$ cluster ($\bar{\sigma} = 1.20$). Note the sequential «evaporation» of single Ar atoms.

$\bar{\sigma} = 1.2$) for the dissociative dynamics of the Ar_{13} following excimer formation. Two reactive processes were observed: iii) A fast stepwise « evaporation » of Ar atoms is exhibited on the time scale of $(0.8 \div 4)$ ps. This process is induced by the energy transfer process i). Subsequently, an additional reactive process appears (fig. 25): iv) slower vibrational predissociation of Ar atoms on the time scale of > 10 ps. This dissociation is induced by both energy transfer processes i) and ii). It is imperative to note that the short-time « explosion » of the electronically excited cluster is induced by energy transfer due to short-range repulsive interactions. When these interactions are switched off by taking $\bar{\sigma} = 1.00$, only mechanism ii) is operative for vibrational-energy flow into the cluster and the cluster dissociation process, which again occurs by stepwise « evaporation », occurring on the time scale of $\sim (30 \div 1000)$ ps. The appropriate excited-state repulsive physical parameter characterizing excimer-cluster interactions in RGC is $\bar{\sigma} = 1.10 \div 1.20$, and we expect the occurrence of energy flow predissociation induced by excited-state repulsive interactions to occur on the time scale of $(1 \div 20)$ ps. We conclude this analysis of molecular dynamics in electronically excited states of RGC with several words of wisdom. Firstly, a new mechanism of vibrational-energy flow induced by short-range repulsions has been documented. This mechanism will be of considerable importance for energy exchange between any extravalence (Rydberg) excitation and a cluster. Secondly, in small ($n = 13$) clusters the consequences of vibrational-energy flow into the cluster involve a reactive dissociative process. It will be extremely interesting to increase the cluster size to establish the « transition » from reactive vibrational predissociation and « nonreactive » vibrational excitation of the cluster modes. Thirdly, the small $Ar_{11}Ar_2^*$ electronically excited cluster provides an example of a system where « statistical » vibrational-energy redistribution did not occur. The « mode selective » excitation of the excimer in the cluster constitutes a nice example for the violation of vibrational-energy equipartitioning in a large system.

7˙3. *Fission of microclusters.* – It was suggested by COMPTON [89] that dissociation of some hydrogen-bonded microclusters may result in ionic species. The process considered involved the fission of $(H_2O)_n$ microclusters:

$$(7.3) \qquad (H_2O)_n \xrightarrow{\text{vibrational excitation}} (H_2O)_n^* \xrightarrow{\text{fission}} H^+(H_2O)_p + OH^-(H_2O)_q ,$$

$$p + q + 1 = n.$$

Using thermochemical data, COMPTON [89] was able to estimate the minimum energy, E, required for symmetric fission, i.e. $p = q$. From the data summarized in fig. 27, it is apparent that this minimum energy is drastically reduced with increasing cluster size. Nevertheless, even for fairly large clusters, this energy is substantial $(E \sim 3.9 \text{ eV}$ for $(H_2O)_{13})$ and very high vibrational overtones
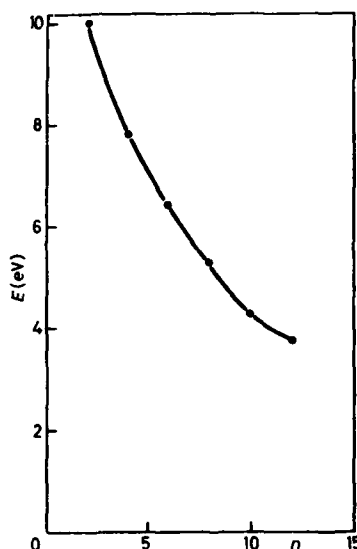
Fig. 27. – Estimates of the energy required for the symmetric fission of $(H_2O)_n$ clusters: $(H_2O)_n^* \rightarrow H^+(H_2O)_P + (OH^-)(H_2O)_P$; $2P + 1 = n$. Data from ref. [89].

have to be excited in order to make this cluster fission process amenable to experimental observation. The macroscopic analogue of this interesting cluster fission process involves the ionic photodissociation in liquid water, which has been recorded experimentally and which has an onset at $E \sim 1$ eV [90]. Dielectric screening of the Coulomb interactions, which prevail in the liquid, provides an additional contribution to the lowering of the threshold energy.

* * *

REFERENCES

[1]   *Proceedings of the International Meeting on Small Particles and Inorganic Clusters*, *J. Phys. (Paris)*, C2, 38 (1977).
[2]   *Proceedings of the II International Meeting on Small Particles and Inorganic Clusters*, *Lausanne, 1980*, *Surf. Sci.*, 106, 1 (1981).
[3]   *Proceedings of Bunsengesellschaft Discussion Meeting on Experiments on Clusters* *Koningstein, 1983*, *Ber. Bunsenges. Phys. Chem.*, 88 (1984).
[4]   M. H. COHEN, I. WEBMAN and J. JORTNER: *Phys. Rev. B*, 17, 4555 (1978).

[5] E. W. BECKER, K. BIER and W. HENKENS: Z. Phys., 146, 333 (1956).

[6] O. F. HAGENA and W. OBERT: J. Chem. Phys., 56, 1793 (1972).

[7] H. P. BALTES: J. Phys. (Paris), C2, 38, 152 (1977).

[8] B. DONN, J. HECHT, R. KHANNA, J. NUTH, S. STRANZ and A. B. ANDERSON: Surf. Sci., 106, 576 (1981).

[9] T. P. MARTIN: Phys. Rep., 95, 169 (1983).

[10] U. LANDMAN, D. SCHARF and J. JORTNER: Isomerization and Melting in Alkali Halide Clusters (to be published).

[11] J. BARKER: J. Phys. (Paris), C2, 38, 37 (1977).

[12] M. R. HOARE: Adv. Chem. Phys., 40, 49 (1979).

[13] J. FARGES, M. F. DE FERAUDY, B. RAOULT and G. TORCHET: J. Chem. Phys., 78, 5067 (1983).

[14] C. L. BRIANT and J. J. BURTON: J. Chem. Phys., 63, 2045 (1975).

[15] J. B. KAELBERER and R. D. ETTERS: J. Chem. Phys., 66, 3233 (1977).

[16] R. D. ETTERS and J. B. KAELBERER: J. Chem. Phys., 66, 5112 (1977).

[17] R. KUBO: J. Phys. (Paris), C2, 38, 270 (1977).

[18] J. M. ZIMAN: in Theory of Solids (Cambridge University Press, Cambridge, 1964).

[19] H. FROHLICH: Adv. Phys., 3, 325 (1954).

[20] J. P. BOREL: Surf. Sci., 106, 1 (1981).

[21] M. HASEGAWA, M. WATABE and K. HOSHINO: Surf. Sci., 106, 11 (1981).

[22] P. PAWLOW: Z. Phys. Chem., 66, 545 (1909).

[23] D. A. BUFFAT and J. P. BOREL: Phys. Rev. A, 13, 2289 (1976).

[24] P. R. COUCHAMAN and C. L. RYAN: Philos. Mag. A, 37, 369 (1978).

[25] K. HOSHINO and S. SHITAMURA: Philos. Mag. A, 40, 137 (1979).

[26] G. NATANSON, F. AMAR and R. S. BERRY: J. Chem. Phys., 78, 399 (1983).

[27] F. H. STILLINGER and T. A. WEBER: Phys. Rev. A, 25, 978 (1982).

[28] A. AMIRAV, U. EVEN and J. JORTNER: J. Chem. Phys., 75, 2489 (1981).

[29] A. AMIRAV, U. EVEN and J. JORTNER: J. Phys. Chem., 86, 3345 (1982).

[30] D. H. LEVY: Adv. Chem. Phys., 47, 323 (1982).

[31] S. S. KIM and G. D. STEIN: J. Appl. Phys., 51, 6419 (1980).

[32] U. EVEN and J. JORTNER: J. Chem. Phys., 78, 3445 (1983).

[33] A. W. CASTLEMAN, B. D. KAY, V. HERMANN, P. M. HOLLAND and T. D. MÄRK: Surf. Sci., 106, 179 (1981).

[34] M. HEAVEN, T. A. MILLER and V. E. BONDYBEY: J. Chem. Phys., 76, 3831 (1982).

[35] J. GSPANN and H. VOLLMAR: J. Low Temp. Phys., 45, 343 (1981).

[36] P. M. DEHMER and S. T. PRATT: J. Chem. Phys., 76, 843 (1982).

[37] J. Q. SEARAY and J. B. FENN: J. Chem. Phys., 61, 5282 (1974).

[38] Y. CHANUT, J. MARTIN and R. SALIN: Surf. Sci., 106, 563 (1981).

[39] P. R. W. HENKES and U. PFEIFFER: Ber. Bunsenges. Phys. Chem., 88, 258 (1984).

[40] C. E. KLOTZ and R. E. COMPTON: J. Chem. Phys., 67, 1779 (1977).

[41] C. E. KLOTZ and R. E. COMPTON: J. Chem. Phys., 69, 1636 (1978).

[42] M. ARMBUSTER, H. HABERLAND and H. G. SCHINDLER: Phys. Rev. Lett., 47, 323 (1981).

[43] H. HABERLAND, C. LUDEWIGT, H. G. SCHINDLER and D. R. WORSNOP: Surf. Sci., 156, 157 (1985).

[44] H. HABERLAND, H. LANGOSCH, H. G. SCHINDLER and D. R. WORSNOP: Ber. Bunsenges. Phys. Chem., 88, 270 (1984).

[45] N. SCHWENTNER, E.-E. KOCH and J. JORTNER: in Electronic Excitations in Condensed Rare Gases, Springer Tracts in Modern Physics, Vol. 107 (Springer-Verlag, Berlin, 1985), p. 1.

[46] H. HABERLAND: Surf. Sci., 156, 305 (1985).

[47] T. HOLSTEIN: *Ann. Phys. (N. Y.)*, **8**, 343 (1959).
[48] W. KANTZMANN: in *Quantum Chemistry* (Academic Press, New 1957).
[49] W. M. TROTT, N. BLAIS and E. A. WALTERS: *J. Chem. Phys.*, **69**
[50] S. H. LINN, Y. ONO and C. Y. NG: *J. Chem. Phys.*, **74**, 3342 (19:
[51] Y. ONO, S. H. LINN, H. F. PREST, M. E. GRESS and C. Y. NG: *J.* **73**, 2523 (1980).
[52] K. H. FUNG, W. E. HENKE, H. L. SELZLE and E. W. SCHLAG: *J.* **85**, 3560 (1981).
[53] U. EVEN, S. LEUTWYLER, Z. BERKOVITCH-YELLIN and J. JORTN *Phys.*, **78**, 309 (1983).
[54] N. R. KESTNER, J. JORTNER, M. H. COHEN and S. A. RICE: *Ph* **A 56** (1965).
[55] J. JORTNER, N. R. KESTNER, S. A. RICE and M. H. COHEN: *J.* **43**, 2614 (1965).
[56] M. H. COHEN and J. JORTNER: *Phys. Rev.*, **180**, 238 (1969).
[57] J. JORTNER and A. GAATHON: *Can. J. Chem.*, **55**, 1801 (1977).
[58] N. BARTLET: private communication.
[59] R. N. COMPTON, P. W. REINHARDT and C. D. COOPER: *J. Chem. F* (1975).
[60] A. R. ROSSI and K. D. JORDAN: *J. Chem. Phys.*, **70**, 4422 (1979).
[61] J. JORTNER: *J. Chem. Phys.*, **30**, 839 (1959).
[62] D. A. COPELAND, N. R. KESTNER and J. JORTNER: *J. Chem. P* (1970).
[63] M. NEWTON: *J. Chem. Phys.*, **58**, 5833 (1973).
[64] Recent attempts to observe $(H_2O)_n^-$ clusters include those by D. R. of Harvard University (private communication) and of R. N. Co Ridge National Laboratory (private communication).
[65] B. K. RAO and N. R. KESTNER: *J. Chem. Phys.*, **80**, 1587 (1984).
[66] N. R. KESTNER and J. JORTNER: *J. Phys. Chem.*, **88**, 3818 (1984)
[67] F. H. STILLINGER and C. W. DAVID: *J. Chem. Phys.*, **73**, 3384 (1!
[68] J. FARGES, M. F. DE FERAUDY, B. RAOULT and G. TORCHET: *8* **95** (1981).
[69] U. LANDMAN, D. SCHARF and J. JORTNER: *Phys. Rev. Lett.*, **54**, 1!
[70] R. P. FEYNMAN and A. R. HIBBS: in *Quantum Mechanics and* (McGraw-Hill, New York, N. Y., 1965).
[71] D. CHANDLER and P. G. WOLYNES: *J. Chem. Phys.*, **79**, 4078 (19!
[72] D. CHANDLER: *J. Chem. Phys.*, **88**, 3400 (1984).
[73] M. PARRINELLO and A. RAHMAN: *J. Chem. Phys.*, **80**, 860 (1984).
[74] L. S. SCHULMAN: in *Techniques and Applications of Path Integrals* York, N. Y., 1981).
[75] M. F. HERMAN, E. J. BRUSKIN and B. J. BERNE: *J. Chem. Phys.*, **76**
[76] D. CALLAWAY and A. RAHMAN: *Phys. Rev. Lett.*, **49**, 613 (1982).
[77] E. FERMI, J. PASTA and S. ULAM: in *Collected Papers by E.* (The University of Chicago Press; Accademia Nazionale dei Lincei, p. 978.
[78] K. G. WILSON: *Rev. Mod. Phys.*, **47**, 773 (1975).
[79] F. G. FUMI and M. P. TOSI: *J. Phys. Chem. Solids*, **25**, 31, 45 (1!
[80] R. W. SHAW: *Phys. Rev.*, **174**, 769 (1968).
[81] N. F. MOTT and R. W. GURNEY: in *Electronic Processes in Ionic Cr* University Press, Oxford, 1946).
[82] J. W. BRADY and J. D. DOLL: *J. Chem. Phys.*, **73**, 2767 (1980).

Best available Page

[47] T. HOLSTEIN: *Ann. Phys. (N. Y.)*, **8**, 343 (1959).

[48] W. KANTZMANN: in *Quantum Chemistry* (Academic Press, New 1957).

[49] W. M. TROTT, N. BLAIS and E. A. WALTERS: *J. Chem. Phys.*, **69**

[50] S. H. LINN, Y. ONO and C. Y. NG: *J. Chem. Phys.*, **74**, 3342 (19:

[51] Y. ONO, S. H. LINN, H. F. PREST, M. E. GRESS and C. Y. NG: *J.* **73**, 2523 (1980).

[52] K. H. FUNG, W. E. HENKE, H. L. SELZLE and E. W. SCHLAG: *J.* **85**, 3560 (1981).

[53] U. EVEN, S. LEUTWYLER, Z. BERKOVITCH-YELLIN and J. JORTN *Phys.*, **78**, 309 (1983).

[54] N. R. KESTNER, J. JORTNER, M. H. COHEN and S. A. RICE: *Ph* A **56** (1965).

[55] J. JORTNER, N. R. KESTNER, S. A. RICE and M. H. COHEN: *J.* **43**, 2614 (1965).

[56] M. H. COHEN and J. JORTNER: *Phys. Rev.*, **180**, 238 (1969).

[57] J. JORTNER and A. GAATHON: *Can. J. Chem.*, **55**, 1801 (1977).

[58] N. BARTLET: private communication.

[59] R. N. COMPTON, P. W. REINHARDT and C. D. COOPER: *J. Chem. P* (1975).

[60] A. R. ROSSI and K. D. JORDAN: *J. Chem. Phys.*, **70**, 4422 (1979).

[61] J. JORTNER: *J. Chem. Phys.*, **30**, 839 (1959).

[62] D. A. COPELAND, N. R. KESTNER and J. JORTNER: *J. Chem. Pl* (1970).

[63] M. NEWTON: *J. Chem. Phys.*, **58**, 5833 (1973).

[64] Recent attempts to observe $(H_2O)_n^-$ clusters include those by D. R. of Harvard University (private communication) and of R. N. Col Ridge National Laboratory (private communication).

[65] B. K. RAO and N. R. KESTNER: *J. Chem. Phys.*, **80**, 1587 (1984).

[66] N. R. KESTNER and J. JORTNER: *J. Phys. Chem.*, **88**, 3818 (1984;

[67] F. H. STILLINGER and C. W. DAVID: *J. Chem. Phys.*, **73**, 3384 (1!

[68] J. FARGES, M. F. DE FERAUDY, B. RAOULT and G. TORCHET: *8* 95 (1981).

[69] U. LANDMAN, D. SCHARF and J. JORTNER: *Phys. Rev. Lett.*, **54**, 1!

[70] R. P. FEYNMAN and A. R. HIBBS: in *Quantum Mechanics and J* (McGraw-Hill, New York, N. Y., 1965).

[71] D. CHANDLER and P. G. WOLYNES: *J. Chem. Phys.*, **79**, 4078 (19!

[72] D. CHANDLER: *J. Chem. Phys.*, **88**, 3400 (1984).

[73] M. PARRINELLO and A. RAHMAN: *J. Chem. Phys.*, **80**, 860 (1984).

[74] L. S. SCHULMAN: in *Techniques and Applications of Path Integrals* York, N. Y., 1981).

[75] M. F. HERMAN, E. J. BRUSKIN and B. J. BERNE: *J. Chem. Phys.*, **76**

[76] D. CALLAWAY and A. RAHMAN: *Phys. Rev. Lett.*, **49**, 613 (1982).

[77] E. FERMI, J. PASTA and S. ULAM: in *Collected Papers by E. .* (The University of Chicago Press; Accademia Nazionale dei Lincei, p. 978.

[78] K. G. WILSON: *Rev. Mod. Phys.*, **47**, 773 (1975).

[79] F. G. FUMI and M. P. TOSI: *J. Phys. Chem. Solids*, **25**, 31, 45 (1!

[80] R. W. SHAW: *Phys. Rev.*, **174**, 769 (1968).

[81] N. F. MOTT and R. W. GURNEY: in *Electronic Processes in Ionic Cr* University Press, Oxford, 1946).

[82] J. W. BRADY and J. D. DOLL: *J. Chem. Phys.*, **73**, 2767 (1980).

Best available Page

[83] M. F. VERNON, D. J. KRAYNOVICH, H. S. KWOK, J. M. LISY, Y. R. SHEA and Y. T. LEE: *J. Chem. Phys.*, **77**, 47 (1982).

[84] S. A. RICE: *Adv. Chem. Phys.*, **47**, 117 (1982).

[85] J. JORTNER and R. D. LEVINE: *Adv. Chem. Phys.*, **47**, 1 (1982).

[86] J. JORTNER, E. E. KOCH and N. SCHWENTNER: in *Photophysics and Photochemistry in the Vacuum Ultraviolet*, edited by S. P. MCGLYN, G. L. FINDLEY and R. H. HUBNER (Reidel Publ. Co., Dordrecht, 1985), p. 515.

[87] D. SCHARF, U. LANDMAN and J. JORTNER: *Chem. Phys. Lett.*, **126**, 495 (1986).

[88] I. MESSING and J. JORTNER: *J. Chem. Phys.*, **66**, 2239, 4577 (1977).

[89] R. N. COMPTON: in *Photophysics and Photochemistry in the Vacuum Ultraviolet*, edited by S. P. MCGLYN, G. L. FINDLEY and R. H. HUBNER (Reidel Publ. Co., Dordrecht, 1985), p. 261.

[90] W. C. NATZLE, C. B. MOORE, D. M. GOODAL, W. FRISCH and J. F. HOLZWORTH: *J. Phys. Chem.*, **85**, 2082 (1981).